UNIVERSITY OF MINNESOTA
ST. ANTHONY FALLS HYDRAULIC LABORATORY

Project Report No. 272

COOLING-INDUCED CONVECTIVE LITTORAL CURRENTS IN LAKES: SIMULATION AND ANALYSIS

by

Georgios M. Horsch

and

Heinz G. Stefan

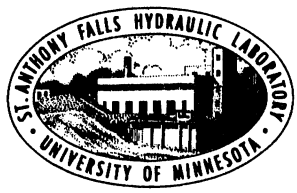

Prepared for

Legislative Commission on Minnesota Resources
Minneapolis, Minnesota

November 1988
Minneapolis, Minnesota

University of Minnesota
St. Anthony Falls Hydraulic Laboratory

Project Report No. 272

COOLING-INDUCED CONVECTIVE LITTORAL CURRENTS IN LAKES: SIMULATION AND ANALYSIS

by

Georgios M. Horsch

and

Heinz G. Stefan

Prepared for

Legislative Commission on Minnesota Resources
Minneapolis, Minnesota

November 1988
Minneapolis, Minnesota

ABSTRACT

Cooling of lakes through the water surface at a constant per unit area rate causes, under calm conditions, the development of a horizontal temperature gradient along the littoral slope, since water columns of different depths have different rates of temperature change. The temperature gradient gives rise to a convective circulation that consists of a cool undercurrent and an unstable surface return flow. This thermally induced circulation initiates water exchange between the littoral and pelagic regions with potential for transport of dissolved constituents, thereby affecting the water quality of the lake.

The flow development is studied numerically by extracting solutions to the system consisting of the continuity equation and the two–dimensional unsteady Navier–Stokes equations coupled with the energy equation through the buoyancy term. The solutions are obtained in a wedge–like domain, fitted in polar coordinates, for various values of the independent parameter, which are the Rayleigh number (Ra), the Prandtl number (Pr) and the slope (S).

Laboratory experimentation verifies the numerically obtained flow features of littoral currents and extends the range of Ra values beyond the range where numerical simulations are affordable.

Field verification of the occurrence of littoral currents is provided by the outcome of a simplified cells–in–series analysis of temperature profiles developing in response to night–time cooling along a littoral slope.

CONTENTS

LIST OF FIGURES

List of Figures (Cont'd)

List of Figure (Cont'd)

List of Figures (Cont'd)

I. INTRODUCTION

The temperature structure of moderate size temperate lakes is predominantly one–dimensional in the vertical, even though several physical processes create transient horizontal inhomogeneities. This is because after the action of the physical forcing has ceased (e.g. after cessation of wind), gravitational motions arise which tend to smooth out any horizontal temperature gradients [Imberger, 1985]. As a result, one–dimensional models [Stefan and Ford, 1975; Harleman and Hurley, 1977] have been quite successful in predicting the temperature structure for long periods of time (up to years), provided that an adequate time step (commonly 1 day) is used, even though they do not account explicitly for horizontal convective motions is used.

The gravitational motions induced by local temperature gradients may, however, be important transport mechanisms even if they contribute little to the lake stratification. Imberger [1985] has identified as mechanisms responsible for horizontal mixing in the epilimnion of lakes differential deepening of the mixed layer and differential heating. Differential deepening can be created by the spatial variability of the wind field or the sheltering of the lake shores. Differential heating can be the result of absorption of radiation at different depths, e.g. due to differences in turbidity. If submerged aquatic vegetation is present, it can also be due to the enhanced absorption of radiation at the surfaces of leaves [Dale and Gillespie, 1977]. The study presented herein examines one horizontal transport mechanism, namely the convective currents that can develop in the littoral zone, under calm conditions, during cooling of lakes. These currents provide an exchange mechanism between littoral and pelagic water. Hydraulic exchange is especially important in studies of nutrient exchange between littoral and pelagic water. For example, it is important in evaluating the possibility that littoral vegetation contributes significantly to the phosphorus pools, so important in freshwater systems [Carpenter, 1983]. As emphasized recently by Carpenter and Lodge [1986], one of the most important questions concerning the role of littoral zones in the functioning of lake ecosystems is the extent to which beds of vegetation act as sources or sinks for dissolved constituents in general. Quantification of hydraulic exchange is necessary in attempting to answer these questions.

In more precise physical terms, during cooling of water on a littoral slope, as the surface water becomes unstable, cool plunging sheets (thermals) form and distribute over depth the negative buoyancy created at the surface (Fig. I–1). Because depth increases progressively along a slope, approximately the same amount of heat is being extracted from "columns" of different depth. In time, a horizontal temperature gradient forms and induces horizontal circulation in the littoral zone. The circulation consists of a stable cold undercurrent and an unstable convecting return flow. This stratification is weak, with significant interaction between the developing

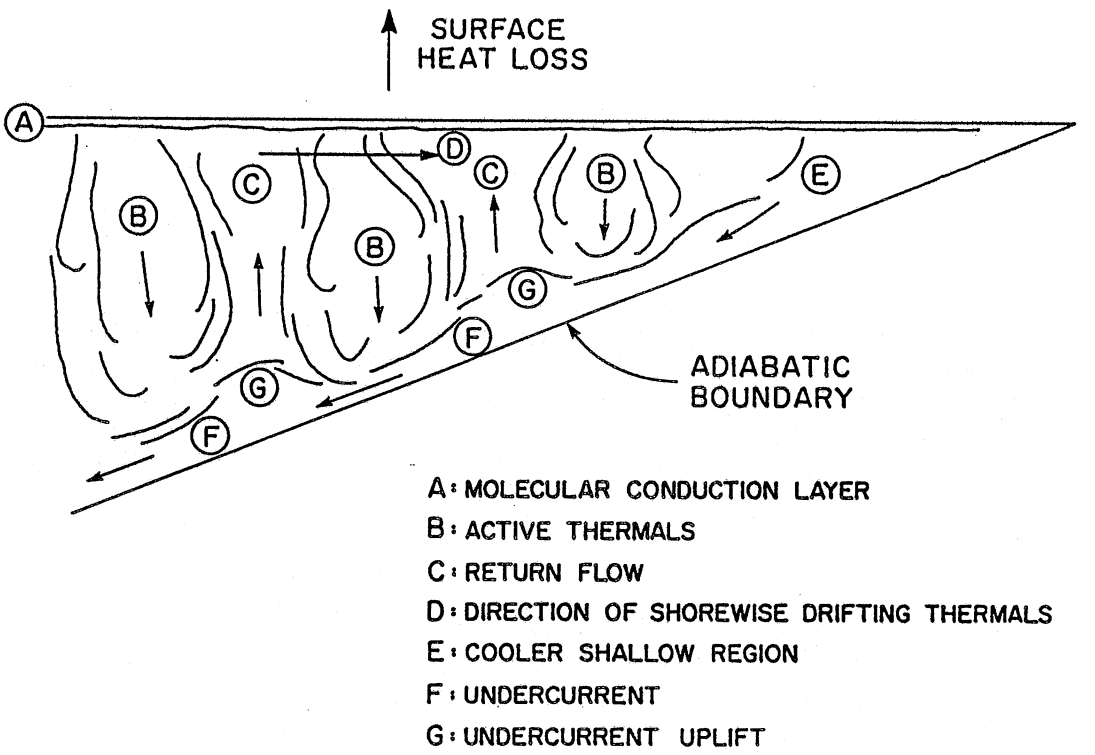

Fig. I–1. Quasi–steady phase in the evolution of a convective current on a slope due to surface cooling.

layers. This study analyzes some aspects of this phenomenon by extracting numerical solutions of the unsteady Navier–Stokes equations in a triangular enclosure. The numerical results are complemented with a visualization experiment. Finally, evidence of the development of littoral convective currents is extracted from field data. To place this work in the context of the available literature, studies of similar mechanisms are mentioned in the next chapter.

II. BACKGROUND

A. HORIZONTAL GRAVITATIONAL MOTIONS

1. Lake Sidearms

In coastal waters heat transfer through the water surface may, under favorable conditions, generate horizontal temperature gradients. An example is the spring thermocline which occurs when solar radiation heats up nearshore shallow waters faster than the open waters and creates an inclined density interface [Csanady, 1982]. A similar phenomenon can develop during the heating phase of the diurnal cycle; Patterson [1987] formulated an idealized model of the process and presented preliminary numerical solutions.

The circulation in the side arms of cooling lakes has been examined by Brocard et al. [1977]. Based on their experiments, they introduced the two–layer flow schematization and derived a closed form solution for the horizontal bottom. The mass and buoyancy flux across the interface were neglected; thus, the discharge flow rate does not depend on the x–coordinate. The justification for this approximation was the experimental observation that when the upper layer depth is less than about half the total depth at the open end (i.e. when the thermocline of the main lake is above half the depth at the junction) then a downflow is concentrated near the closed end. For deeper upper layers, the two–layer schematization is less useful since, in order to apply the model, a downflow distribution has to be assumed.

Sturm and Kennedy [1980] used a Kármán–Pohlhausen technique to analyze the side–arm problem. They presented their results in terms of correlations for a wide range of arm dimensions and meteorological conditions. Their model was verified by a laboratory experiment using setting different from that of Brocard et al. [1977].

Jain [1982] derived an analytical solution of the basic equations using the assumption of similarity of the velocity and temperature profiles.

Ookubo and Muramoto [1987] presented some field measurements in Lake Biwa, Japan, which consist of a deep and a shallow basin. Their data demonstrate the development of a convective current during cooling, but under strong wind conditions the circulation becomes wind–driven.

Harashima and Watanabe [1986] performed a laboratory experiment which simulated more directly than previous experiments the cooling–induced side arm (or estuary) circulation, in that both the circulation flow rate and the thickness of the two layer system were established internally rather than being imposed. They found the circulation flow rate to be proportional to the 0.22 power of the horizontal coordinate.

Phillips [1966] studied convective currents in the Red Sea. He assumed a flow driven by a constant surface buoyancy flux which results from the surface heat flux and the increase in salt concentration due to evaporation. His solution was based on the assumption of similarity profiles and involved unknown similarity functions. Phillips [1970] showed that if a stably stratified fluid is bounded by an inclined "adiabatic" wall, then a motion is produced by the local gradient in the region where the horizontal "isotherm" meets the inclined adiabatic boundary. He derived a simple analytical solution for the upslope flow rate thus generated.

Another class of relevant studies deals with natural convective flow in enclosures. Cormack et al. [1974a, part 1] studied steady natural convection in a shallow rectangular enclosure with differentially heated end walls, as a model for gravitational circulation in estuaries. They extracted asymptotic solutions in the limit as the aspect ratio of the enclosure tends to zero. Cormak et al. [1974b, part 2] produced numerical solutions to the same problem and found excellent agreement between the numerical and analytical solutions, provided the aspect ratio is less than 0.1.

The unsteady flow in rectangular enclosures with differentially heated end walls was studied by Patterson and Imberger [1980]. They presented a detailed scale analysis of the evolution of the flow starting from quiescent conditions, in terms of the non–dimensional parameters of the flow, i.e. the Rayleigh number (Ra), the Prandtl number (Pr) and the enclosure aspect ratio. Depending on the relative value of these parameters, the flow was classified as conductive, convective and transitional. Numerical solutions representative of each regime illustrated the development of the flow.

Poulikakos and Bejan [1983] investigated the unsteady development of the flow in a triangular enclosure with the lower horizontal side heated and the upper, sloping side cooled. Viewed as a variation of the classic Bénard configuration of convection between parallel, differentially heated plates, their study yields the interesting result that for Grashof number (Gr) up to 10^5 the flow consists of a single cell extending along the entire enclosure. This is to be contrasted to the results of the present study, where the flow developing in a similar geometry and range of independent parameters (Ra, Pr, Slope), but with different temperature boundary conditions, was found to exhibit the formation of transient convective cells.

2. Convective Cells and Thermals

As already mentioned, the motive force of littoral currents is a horizontal temperature gradient, which forms in response to surface cooling and vertical mixing induced by convective cells. For fluid between parallel plates and at low Rayleigh numbers these cells are steady two–dimensional and are referred to as Bénard cells. As the Rayleigh number increases, the cells undergo several transitions [Krishnamurti, 1970] from two– to three–dimensional flow, to time dependent three–dimensional flow and finally to turbulent flow. A flow regime chart for a wide range of the independent parameters (Ra, Pr) can be found in Krishnamurti and Howard [1981]. Their experiments revealed that at high enough Rayleigh number, the flow, which was no longer cellular, was dominated by transient plumes with a

horizontal scale comparable to the layer depth. There was, however, also horizontal flow with a scale comparable to the horizontal scale of the enclosure.

Katsaros [1981] reported observations of convection patterns that developed in a pond during cooling. Experiments of water cooled from the surface have been performed by Spangenberg and Rowland [1961], Foster [1969], and more recently by Katsaros et al. [1977] and Tamai and Asaeda [1984, 1987].

Katsaros et al. [1977] studied in detail the structure of the surface thermal boundary layer that forms when the water undergoes cooling. The relation of the boundary layer thickness to the surface heat loss was expressed as a relation between the Nusselt (Nu) and the Rayleigh numbers.

The characteristics of thermals were examined in great detail by Tamai and Asaeda [1984]. They introduced the distinction between a thermal and a plume, which consists of several successive thermals, and determined the dependence of the length scale and frequency of thermals on the Rayleigh number.

Some additional details concerning the experimental methods used in the aforementioned studies are summarized in Chapter VI.

B. SCOPE OF STUDY

To study the development of large-scale horizontal natural convective flow on a sloping boundary (littoral region of a lake), a problem of heat transfer in a triangular enclosure is posed. The formulation of the numerical model described in Chapter III is guided by the desire to capture what are believed to be the essential features of littoral convective currents (temperature boundary conditions) and by the need to compromise so as to get a problem tractable by available numerical methods (deep-end flow boundary conditions).

The results of the simulation are presented in Chapter IV. The range of the independent parameters (Rayleigh and Prandtl number, slope) over which simulations were performed was dictated by the available computer time. Often the littoral region of lakes is vegetated with aquatic plants. To assess the effects of the littoral plants on the convective circulation, an apparent viscosity, representing the energy dissipation introduced in the flow by the plants, is formulated in Chapter V. The results of a laboratory visualization experiment are included in Chapter VI. Finally, evidence of the development of littoral currents during cooling, extracted from a set of temperature field measurements in the littoral zone of a Wisconsin lake, appears in Chapter VII.

III. THE NUMERICAL MODEL

A. GOVERNING EQUATIONS

The numerical model is formulated in terms of the equations of continuity, momentum, and energy, all expressed in polar coordinates, in which the boundary of the domain can be fitted naturally.

The momentum equations

$$\frac{\partial u}{\partial t} + v\frac{\partial u}{\partial r} + \frac{u}{r}\frac{\partial u}{\partial \theta} + \frac{uv}{r} = -\frac{1}{\rho_o}\frac{1}{r}\frac{\partial p}{\partial \theta} + \nu\left[\frac{1}{r}\frac{\partial}{\partial r}\left[r\frac{\partial u}{\partial r}\right] + \frac{1}{r^2}\frac{\partial^2 u}{\partial \theta^2}\right]$$

$$+ \nu\left[-\frac{u}{r^2} + \frac{2}{r^2}\frac{\partial v}{\partial \theta}\right] + g\beta\,(T_o - T)\cos\theta \qquad \text{(III–1)}$$

$$\frac{\partial v}{\partial t} + v\frac{\partial v}{\partial r} + \frac{u}{r}\frac{\partial v}{\partial \theta} - \frac{u^2}{r} = -\frac{1}{\rho_o}\frac{\partial p}{\partial r} + \nu\left[\frac{1}{r}\frac{\partial}{\partial r}\left[r\frac{\partial v}{\partial r}\right] + \frac{1}{r^2}\frac{\partial^2 v}{\partial \theta^2}\right]$$

$$- \nu\left[\frac{v}{r^2} + \frac{2}{r^2}\frac{\partial u}{\partial \theta}\right] + g\beta\,(T_o - T)\sin\theta \qquad \text{(III–2)}$$

Continuity equation:

$$\frac{1}{r}\frac{\partial}{\partial r}(rv) + \frac{1}{r}\frac{\partial u}{\partial \theta} = 0 \qquad \text{(III–3)}$$

Energy equation:

$$\frac{\partial T}{\partial t} + v\frac{\partial T}{\partial r} + \frac{u}{r}\frac{\partial T}{\partial \theta} = \alpha\left[\frac{1}{r}\frac{\partial}{\partial r}\left[r\frac{\partial T}{\partial r}\right] + \frac{1}{r^2}\frac{\partial^2 T}{\partial \theta^2}\right] \qquad \text{(III–4)}$$

where $u = u(r,\theta)$ is the tangential, $v = v(r,\theta)$ is the radial velocity, p is pressure, T_o is the initial temperature, ν is the kinematic viscosity, β is the thermal expansivity, g is the acceleration of gravity, and α is the thermal diffusivity. In these equations, the Boussinesq approximation has been implemented, and in the body force the density has been expressed as a linear function of the temperature. This formulation of the density has implications for the occurrence of a quasi–steady state as discussed below.

The boundary conditions, shown in Figure III–1, are:

Shear–free surface with heat transfer

$$u = 0 \;;\; \frac{\partial v}{\partial \theta} = 0 \;;\; \frac{k}{r}\frac{\partial T}{\partial \theta} = H \text{ at } \theta = 0,\ 0 < r \leq R \qquad \text{(III–5)}$$

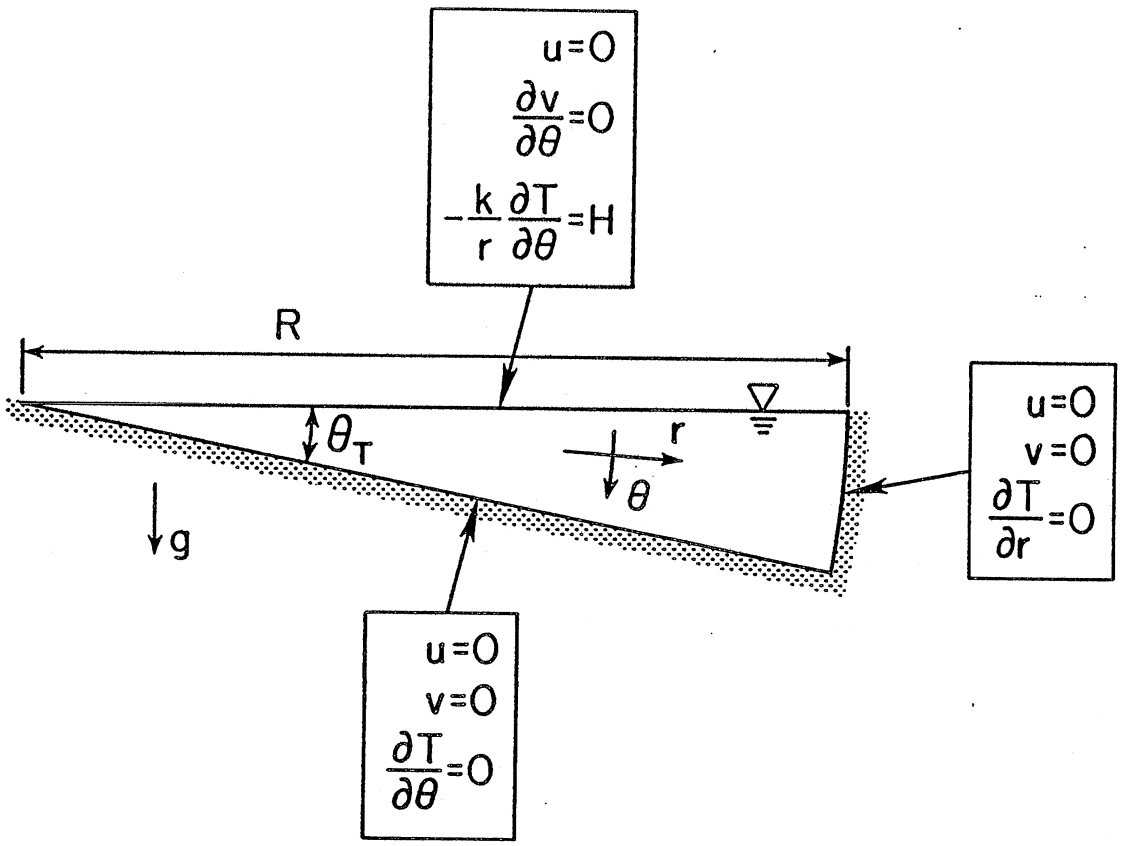

Fig. III–1 Computation domain and boundary conditions.

No slip, adiabatic boundaries at bottom and end of domain

$$u = 0 \;\; ; \;\; v = 0 \;\; ; \;\; \frac{\partial T}{\partial \theta} = 0 \text{ at } \theta = \theta_T, \; 0 < r \leq R \qquad \text{(III–6)}$$

$$u = 0 \;\; ; \;\; v = 0 \;\; ; \;\; \frac{\partial T}{\partial r} = 0 \text{ at } r = R, \; 0 \leq \theta \leq \theta_T \qquad \text{(III–7)}$$

where k is the conductivity, H is the imposed surface heat loss; R and θ_T specify the size of the domain shown in Fig. III–1.

To make the equations dimensionless, a choice of length, velocity, and temperature scales is required. The selection of the pertinent scales in natural convection is a particularly intriguing problem. Detailed scale analysis [Patterson and Imberger, 1980; Bejan, 1984] can produce valuable information about the hierarchy of scales, although it is not always easy to substantiate the results and there are examples of incorrect analyses (e.g. those referred to in Bejan, 1984, p. 119). Ultimately, however, if the scales are used solely to make the equations dimensionless for numerical solutions, the selection can be arbitrary at no damage (although unsubstantiated pronoucements of the opposite exist, e.g. Ostrach [1982b]).

A survey of nondimensionalization scales used in natural convection problems has been given by Ostrach [1982a]. In the present problem the difficulty in choosing the scales is aggravated since, in addition to the velocity, a choice of the temperature scale is also required.

The scales used to normalize the equations for the numerical calculations are:

Length scale

$$h_s = R \sin\theta_T \qquad \text{(III–8)}$$

Velocity scale

$$v_s = \frac{\nu}{h_s} Gr^{1/2} = \left[\frac{g\beta H}{k}\right]^{1/2} h_s \qquad \text{(III–9)}$$

Time scale

$$t_s = \frac{h_s^2}{\nu} Gr^{-1/2} = \left[\frac{k}{\beta g H}\right]^{1/2} \qquad \text{(III–10)}$$

Temperature scale

$$\Delta T_s = \frac{H h_s}{k} \qquad \text{(III–11)}$$

where Gr is the Grashof number. The nondimensional independent parameters of the problem are:

$$\text{Grashof number} = \frac{g\beta H h_s^4}{\nu^2 k} \tag{III–12}$$

$$\text{Prandtl number} = \frac{\nu}{\alpha} \tag{III–13}$$

$$\text{Slope of the enclosure, } S = \tan\theta_T \tag{III–14}$$

The Raleigh number, Ra = Gr Pr, can be used instead of Gr. The scales III–9 and III–10 have been used before, e.g. by Moore and Weiss [1973], in a numerical study of the confined Bénard problem. They did not prove particularly useful here, since, use of α/h and h^2/α as velocity and time scales, respectively, would have made explicit the insensitivity of the flow to Pr as discussed in Chapter 4. (The numerical results would have been, of course, identical.)

B. QUASI–STEADY CONVECTION PROBLEM

Because the domain is cooled from the surface while the bottom and the side are insulated, the water temperatures will keep dropping and no steady state in terms of temperatures can be reached. Because the fluid properties (ν, α, k) are represented as constants and the density is expressed as a linear function of temperature, a state can be reached where the velocities and the temperature gradients (instead of the temperature) become steady. This state is referred to as a quasi–steady state. An example of a one–dimensional conduction problem which exhibits similar quasi–steady behavior can be found in Carslaw and Jaeger [1959, p. 112]. In the quasi–steady state the temperature at each point drops at the same rate:

$$\frac{dT_q}{dt} = -\frac{2H}{\rho c\ R\ \theta_T} \tag{III–15}$$

c = specific heat, or in dimensionless form with $\phi = (T_o - T)/\Delta T_s$

$$\frac{d\phi_q}{dt} = 2Ra^{-1/2}Pr^{-1/2}\ \frac{\sin\theta_T}{\theta_T} \tag{III–16}$$

Thus, we have split the temperature into two components: a spatially averaged temperature which decreases linearly in time (the solution of Eq. III–15) and a component which, after the initial transient, settles into a steady–state spatial distribution.

Substituting $T(r,\theta,t) = -(2Ht/\rho c\ R\ \theta_T) + \tau(r,\theta,t)$ into Eq. III–4:

$$\frac{\partial \tau}{\partial t} + v\frac{\partial \tau}{\partial r} + \frac{u}{r}\frac{\partial \tau}{\partial \theta} = \alpha\left[\frac{1}{r}\frac{\partial}{\partial r}\left[r\frac{\partial \tau}{\partial r}\right] + \frac{1}{r^2}\frac{\partial^2 \tau}{\partial \theta^2}\right] + \frac{2H}{\rho c\ R\ \theta_T} \quad \text{(III–17)}$$

Since all boundary conditions for T involve gradients only and are independent of time, the same boundary conditions apply for τ as for T. The model consisting of Eqs. III–1,2,3, and III–17 and boundary conditions. Eqs. III–5,6,7, is equivalent to the original model and can be interpreted as the model of an enclosure with a uniformly distributed heat source equal to $2H/\rho c\ R\ \theta_T$; the enclosure is being cooled from the surface. Since τ can reach a steady state, no distinction is necessary between the quasi–steady state for temperature T and the steady state for τ. Computationally, however, it is more efficient to solve the problem consisting of Eqs. III–1,2,3,and III–17, especially for high Ra where the flow becomes time–dependent. In the following, T will be substituted for τ while referring to Eq. III–17.

C. THE DEPTH–INTEGRATED ENERGY EQUATION

Among the quantities to be extracted from the numerical solutions are the strength of the circulation Q and the total radial heat transfer $\bar{H}$, which are defined as follows:

$$Q(r) = \frac{1}{2}\int_{\theta=0}^{\theta_T} |v(r,\theta)|\, r\, d\theta \quad \text{(III–18)}$$

$$\bar{H}(r) = \int_{\theta=0}^{\theta_T} \left[\rho c T v - k\frac{\partial T}{\partial r}\right] r\, d\theta \quad \text{(III–19)}$$

These are made dimensionless as:

$$Q' = \frac{Q}{v_s h} \quad ; \quad \bar{H}' = \frac{\bar{H}}{Hh} \quad \text{(III–20)}$$

The steady–state of $\bar{H}$ can be found by integrating Eq. III–17 over the angular direction (this will be subsequently referred to as "depth integration"). The result is:

$$\bar{H}(r,t) = H\, r\left[\frac{r}{R} - 1\right] - \int_{r=0}^{r}\int_{\theta=0}^{\theta_T} \rho c\frac{\partial T}{\partial t}\, r\, d\theta\, dr \quad \text{(III–21)}$$

At steady state:

$$\bar{H}_{st}(r) = Hr\left[\frac{r}{R} - 1\right] \qquad \text{(III–22)}$$

and in dimensionless form:

$$\bar{H}_{st}(r') = r'(r' \sin\theta_T - 1) \qquad \text{(III–23)}$$

D. STEADY TWO–DIMENSIONAL CONDUCTION PROBLEM

Equation III–22 shows that the steady horizontal heat transfer is determined solely by the geometry of the domain and the temperature boundary conditions and not by the medium in which the transfer takes place. It is, therefore, instructive to examine the solution of the temperature field which develops in a solid domain (conduction problem) subjected to the same temperature boundary conditions. The solution is most readily obtained in Cartesian coordinates.

For a pure conduction problem, the energy equation that corresponds to Eq. III–17 is:

$$k\left[\frac{\partial^2 T}{\partial x^2} + \frac{\partial^2 T}{\partial y^2}\right] + \frac{2H}{h} = 0 \qquad \text{(III–24)}$$

with boundary conditions:

$$k\left.\frac{\partial T}{\partial y}\right|_{y=0} = H \quad , \quad \left.\frac{\partial T}{\partial y}\right|_{y=Sx} = S\left.\frac{\partial T}{\partial x}\right|_{y=Sx} \quad , \quad \left.\frac{\partial T}{\partial x}\right|_{x=\ell} = 0 \qquad \text{(III–25)}$$

where $S = h/\ell$ and h, ℓ are indicated in Fig. III–2.

The solution is:

$$T(x,y) = \frac{Hh}{k} S^{-2}\left[\frac{x}{\ell} - \frac{1}{2}\left[\frac{x}{\ell}\right]^2 + S^2\left(\frac{y}{h} - \frac{1}{2}\left[\frac{y}{h}\right]^2\right)\right] \qquad \text{(III–26)}$$

The isotherms corresponding to this solution can be seen in Fig. III–3.

Taking $\Delta T_x = T(\ell,0) - T(0,0)$ as a measure of the horizontal temperature difference we find:

$$\Delta T_x = \frac{1}{2}\frac{Hh}{k} S^{-2} \qquad \text{(III–27)}$$

Since, as already mentioned, the steady horizontal heat transfer is imposed by the geometry and boundary conditions, the ratio of ΔT_x, which develops in a fluid flow, divided by the value for conduction (Eq. III–27), can be taken as an indication of the relative importance of convective versus conductive transfer. Eq. III–27 shows that the pertinent horizontal temperature scale for the conduction problem is:

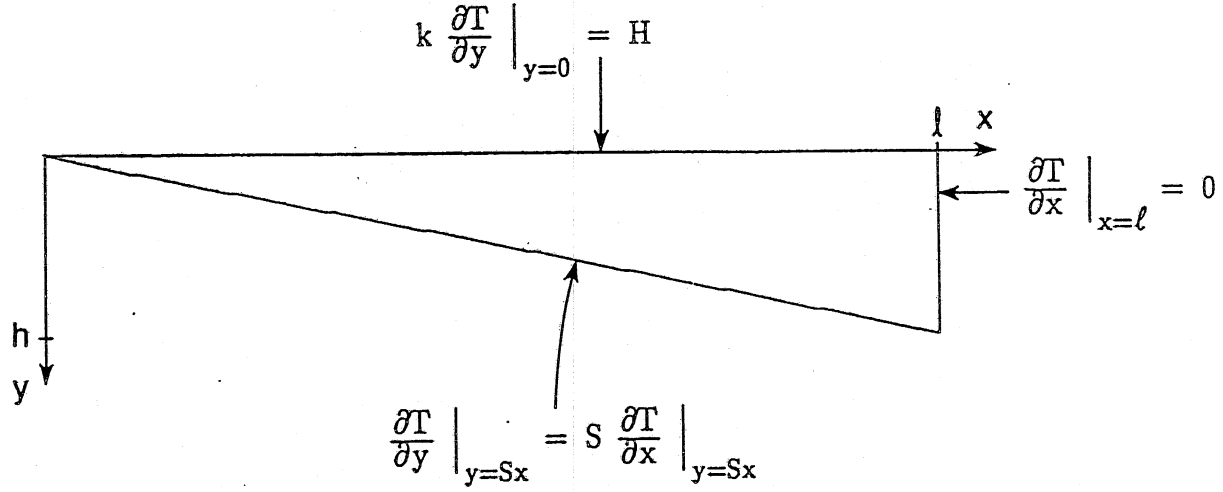

Fig. III–2 Domain and boundary conditions for the conduction problem in Cartesian coordinates.

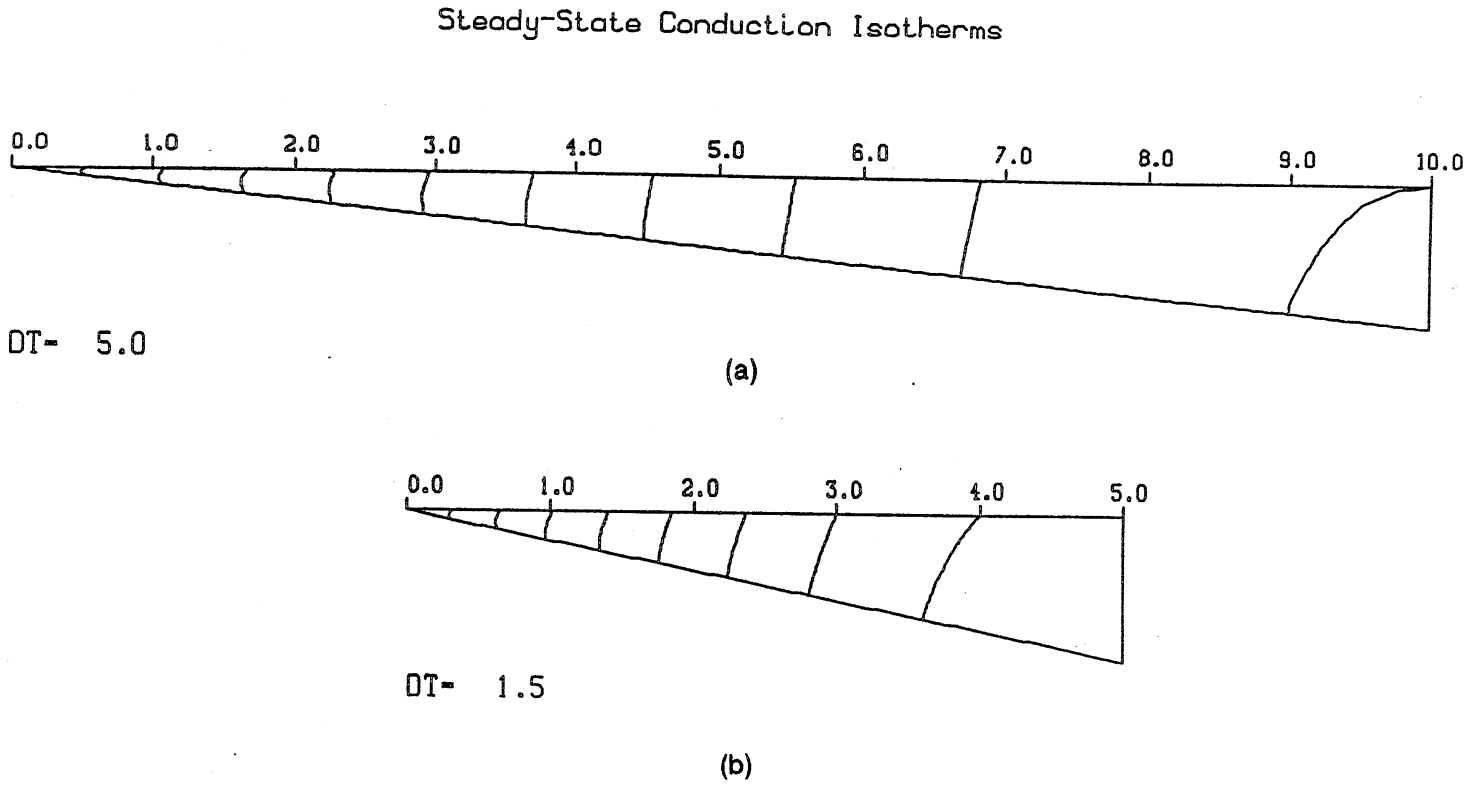

Fig. III–3 Steady–state isotherms for pure conduction (Eq. III–26) for: (a) S=0.1, (b) S=0.2.

$$\Delta T_x \sim \frac{Hh}{k} S^{-2} \qquad \text{(III–28)}$$

It is of interest to examine whether this is a general result, true for any shape of the slope, or whether there are more general slopes for which the scale Hh/k becomes relevant.

To answer this question the behavior of the solution is examined in the limit $S \to 0$. For a general slope of $y = f(t)$, $0 \le x \le \ell$, the equation corresponding to III–24 is:

$$k \left(\frac{\partial^2 T}{\partial x^2} + \frac{\partial^2 T}{\partial y^2} \right) + \frac{H\ell}{\int_0^\ell f \, dx} = 0 \qquad \text{(III–29)}$$

and the boundary conditions, generalizing III–25 are:

$$k \frac{\partial T}{\partial y}\Big|_{y=0} = H \; ; \quad \frac{\partial T}{\partial y}\Big|_{y=f(x)} = f' \frac{\partial T}{\partial x}\Big|_{y=f(x)} \; ; \quad \frac{\partial T}{\partial x}\Big|_{x=\ell} = 0 \qquad \text{(III–30)}$$

These equations are made dimensionless using the scales:

$$x = \hat{x}\ell \; ; \; y = \hat{y}h \; ; \; (f = \hat{f}h) \; ; \; T = \hat{T} \frac{Hh}{k} S^{-2} \qquad \text{(III–31)}$$

The scaled problem and boundary conditions become:

$$S^2 \frac{\partial^2 \hat{T}}{\partial \hat{x}^2} + \frac{\partial^2 \hat{T}}{\partial \hat{y}^2} + \frac{S^2}{\int_0^1 \hat{f}(\hat{x}) d\hat{x}} = 0 \qquad \text{(III–32)}$$

$$\frac{\partial \hat{T}}{\partial \hat{y}}\Big|_{\hat{y}=0} = S^2 \text{(a)} \; ; \quad \frac{\partial \hat{T}}{\partial \hat{y}}\Big|_{\hat{y}=\hat{f}(\hat{x})} = \hat{f}'(\hat{x}) \, S^2 \frac{\partial \hat{T}}{\partial \hat{x}}\Big|_{\hat{y}=\hat{f}(\hat{x})} \text{(b)} \qquad \text{(III–33)}$$

It can be noted that the problem III–32, III–33 does not present a singularity at x=0 so long as $\hat{f}'(0) \neq 0$ and $\hat{f}'(0) \neq \infty$ (assuming $\hat{f}(0)=0$). Otherwise III=33(a) and III=33(b) will be in conflict. The same remark holds for the flow problem III–5, III–6; the condition for non–singularity is met by the linear slope. Problems III–32 and III–33 can be solved by expanding $\hat{T}$ into a series of S:

$$\hat{T} = \hat{T}_0 + \hat{T}_2 S^2 + \hat{T}_4 S^4 + \ldots \qquad \text{(III–34)}$$

for any slope f(x). For the linear slope, it actually yields the exact solution III–26, because $\hat{f}(\hat{x})=\hat{x}$ satisfies the condition for separable exact solution, i.e. that:

$$\frac{\hat{f}'(1-\hat{x}) - \int_0^1 \hat{f}\, d\hat{x}}{\hat{f} - \hat{f}'(1-\hat{x})}$$

be independent of $\hat{x}$. (Another example is the parabolic slope $\hat{f}(\hat{x}) = 2\hat{x}-\hat{x}^2$).

The zero order solution (dropping the $\hat{}$) is:

$$T_o(x_1) = \int_0^{x_1} \frac{1}{f}\left(x - \frac{\int_0^x f\, dx_i}{\int_0^1 f\, dx_i}\right)dx \qquad \text{(III–35)}$$

Since solutions for general slopes are not needed here, the problem is not pursued further. Returning to the relevance of scale Hh/k, if instead of scaling problems III–29 and III–30 with scales III–31, it is scaled with:

$$x = \hat{x}\ell \ ; \ y = \hat{y}; \ (f = \hat{f}h) \ ; \ T = \hat{T}\,\frac{Hh}{k} \qquad \text{(III–36)}$$

the resulting scaled problem is:

$$S^2\,\frac{\partial^2\hat{T}}{\partial\hat{x}^2} + \frac{\partial^2\hat{T}}{\partial\hat{y}^2} + \frac{1}{\int_0^1 \hat{f}\, d\hat{x}} = 0 \qquad \text{(III–37)}$$

with boundary conditions:

$$\frac{\partial\hat{T}}{\partial\hat{y}}\Big|_{y=0} = 1 \ ; \ \frac{\partial\hat{T}}{\partial\hat{y}}\Big|_{\hat{y}=\hat{f}(\hat{x})} = \hat{f}'(x)\ S^2\,\frac{\partial\hat{T}}{\partial\hat{x}}\Big|_{\hat{y}=\hat{f}(\hat{x})} \qquad \text{(III–38)}$$

Expanding in series III–34, the $O(S^o)$ problem is (dropping $\hat{}$):

$$\frac{\partial^2 T_o}{\partial\hat{y}^2} + \frac{1}{\int_0^1 f dx} = 0 \qquad \text{(a)}$$

$$\frac{\partial T_o}{\partial y}\Big|_{y=0} = 1 \qquad \text{(b)} \qquad \text{(III–39)}$$

$$\frac{\partial T_o}{\partial y}\Big|_{y=f(x)} = 0 \qquad \text{(c)}$$

From III–39(a), (b):

$$\frac{\partial T_o}{\partial y} = - \frac{1}{\int_0^1 f dx} y + 1 \qquad \text{(III–40)}$$

so that

$$\frac{\partial T_o}{\partial y} \Big|_{y=f} = - \frac{f}{\int_0^1 f dx} + 1 \qquad \text{(III–41)}$$

Eq. III–41 is in conflict with III–39(c) so long as f is a function of x. Thus the scale Hh/k is relevant only for a "strictly horizontal bottom," when the problem effectively degenerates to the steady–state of the problem in p. 112 of Carslaw and Jaeger [1952].

E. NUMERICAL METHOD

The equations for the flow problem were solved numerically using the SIMPLE algorithm of Patankar and Spalding [1972]. The details of the method described in Patankar [1980, 1981] have been implemented in the code of Patankar [1982]. The main features of the method and some modifications of the original code are summarized below.

The method arrives at a solution of the coupled, nonlinear system of the equations of momentum, continuity and energy through successive iterations. During each iteration, a linearized form of each component of the momentum equation (u,v) is solved, followed by a pressure correction equation (p'), which has been derived from the continuity equation, and the energy equation (T). The matrix that results during the solution of each of these problems (u,v,p',T) is solved by a line–by–line method, utilizing the tridiagonal matrix algorithm.

The discretization of the differential equations is based on a finite volume formulation, which preserves the conservation properties of the equations exactly in the control volume that surrounds each grid point, for coarse and fine grids alike. The convection–diffusion terms are interpolated using the power–law scheme [Patankar, 1980] which is a computationally efficient, close approximation of the exponential scheme. The properties of these schemes were useful in this study where, at least for small Ra, the grid Peclet (Pe) number was found to range from small to large values in different parts of the computation domain. The remaining terms, e.g. the additional terms due to polar coordinates, were discretized separately. The grid is staggered, i.e. the two components of the velocity and the pressure are calculated at different locations to avoid the development of spurious pressure waves. The time marching is fully–implicit even though because of the possibility of the development of physical (convective) instability, the time step was small enough to satisfy a Courant criterion (as verified a posteriori).

As already mentioned, the combined convection–diffusion fluxes were interpolated according to the power–law scheme. To gain further insight into the calculated solutions, it is useful to break down the total flux into its separate convective and diffusive components. For convenience, the appropriate formulas are recorded below for the exponential scheme.

Following the notation of Patankar [1980, p. 80], the one–dimensional convection–diffusion (C/D) equation is:

$$\frac{dJ}{dx} = 0 \qquad \text{(III–42)}$$

in $[x_p, x_E]$, where

$$J = \rho u \phi - \Gamma \frac{d\phi}{dx} \qquad \text{(III–43)}$$

and ϕ = the quantity on which C/D is applied (e.g. u or T) ρu = mass flux, Γ = diffusion coefficient. The total flux at a point $x_e \epsilon [x_p, x_E]$ is:

$$J_e = (\rho u)_e \left(\phi_p + \frac{\phi_P - \phi_E}{\exp(Pe) - 1} \right) \qquad \text{(III–44)}$$

where Pe is the grid Peclet number

$$Pe = \frac{\rho u \, L}{\Gamma} \qquad \text{(III–45)}$$

The diffusive flux at x_e is:

$$- \Gamma \frac{d\phi}{dx} \Big|_e = - (\rho u)_e (\phi_E - \phi_P) \frac{\exp(Pe \, x_e/L}{\exp(Pe) - 1} \qquad \text{(III–46)}$$

and the convective flux at x_e is:

$$(\rho u \, \phi)_e = \Gamma \frac{d\phi}{dx} \Big|_e + J_e \qquad \text{(III–47)}$$

Examples of the separate diffusion and convection fluxes for the radial heat transfer can be seen in Fig. IV–1.

Two modifications were implemented in the original code. The first aimed at making possible unsteady solutions with a finite time step. The second aimed at improving the efficiency of the code on a vector processor. Analysis of the CPU time expended by the various subroutine of code showed that the major amount was spent in the section calculating the coefficients of the matrices and in the matrix solver. After rewriting portions of the coefficient calculating routine so as to make as many parts of it vectorizable as possible, the code executed twice as fast as the original.

IV. RESULTS OF THE NUMERICAL SOLUTIONS

A. RANGE OF INDEPENDENT VARIABLES

To gain insight into the development and steady–state of the flow model consisting of Eqs. III–1 to III–4 and boundary conditions III–5 to III–7, numerical solutions were calculated for different values of the independent parameters Ra, Pr and S. Since the time which is required for the flow to develop is among the dependent variables of interest, the solutions were initiated from a quiescent and isothermal initial condition. The calculated parameters chosen to characterize the dependence of the solutions on the independent parameters of the problem at steady state are $u_{r_{max}}$, Q_{max}, and $\Delta T_{r_{max}}$ at $\theta=\theta_T$. Solutions were calculated for selected triplets of Ra=10^4, 10^6, 10^8, Pr = 7, 10^2, 10^3 and S = 0.2, 0.1. Because the stability characteristics of the flow depend on Ra, a different regime results for each of the Ra values. The main features of these requires remain unaffected by Pr and, to a lesser degree, by S changes, within the examined ranges. It is convenient, therefore, to describe the flow for each value of Ra, followed by observations about the Pr influence. The influence of the slope is discussed in a final section.

B. LOW RAYLEIGH–NUMBER REGIME: Ra = 10^4

1. Flow Development

The development of the flow, from its inception at the onset of the surface heat loss, to the steady–state, is depicted in Fig. IV–1 for Ra = 10^4, Pr=10^3, S = 0.2. For each time instant this figure includes, from top to bottom, instantaneous graphs of (i) streamlines, (ii) isotherms, (iii) radial velocity profiles, (iv) the horizontal circulation flow rate (Eq. III–18) and the (v) total horizontal heat transfer (Eq. III–19). All these quantities are normalized with the scales presented in Section III–1.

At time t=50 (Fig. IV–1), the T=0 isotherm is parallel to the surface along almost the entire enclosure; near the region where it meets the sloping boundary, however, it curves so as to meet this adiabatic boundary perpendicularly. Thus, a local temperature gradient is created which initiates a counterclockwise rotating cell at the shallow end. This cell, in turn, initiates through shear a clockwise rotating cell, which extends along the entire deep–end of the enclosure. The first important feature of the low–Ra regime is that, for S=0.2, this deep–end cell remains stable, i.e. it does not break into smaller cells at a later time, so that during the rest of the development of the flow, the shallow–end cell grows at the expense of the deep–end cell until the latter disappears. The second important feature of this regime is that a steady state is eventually reached (i.e. u, v, T, p become time–independent).

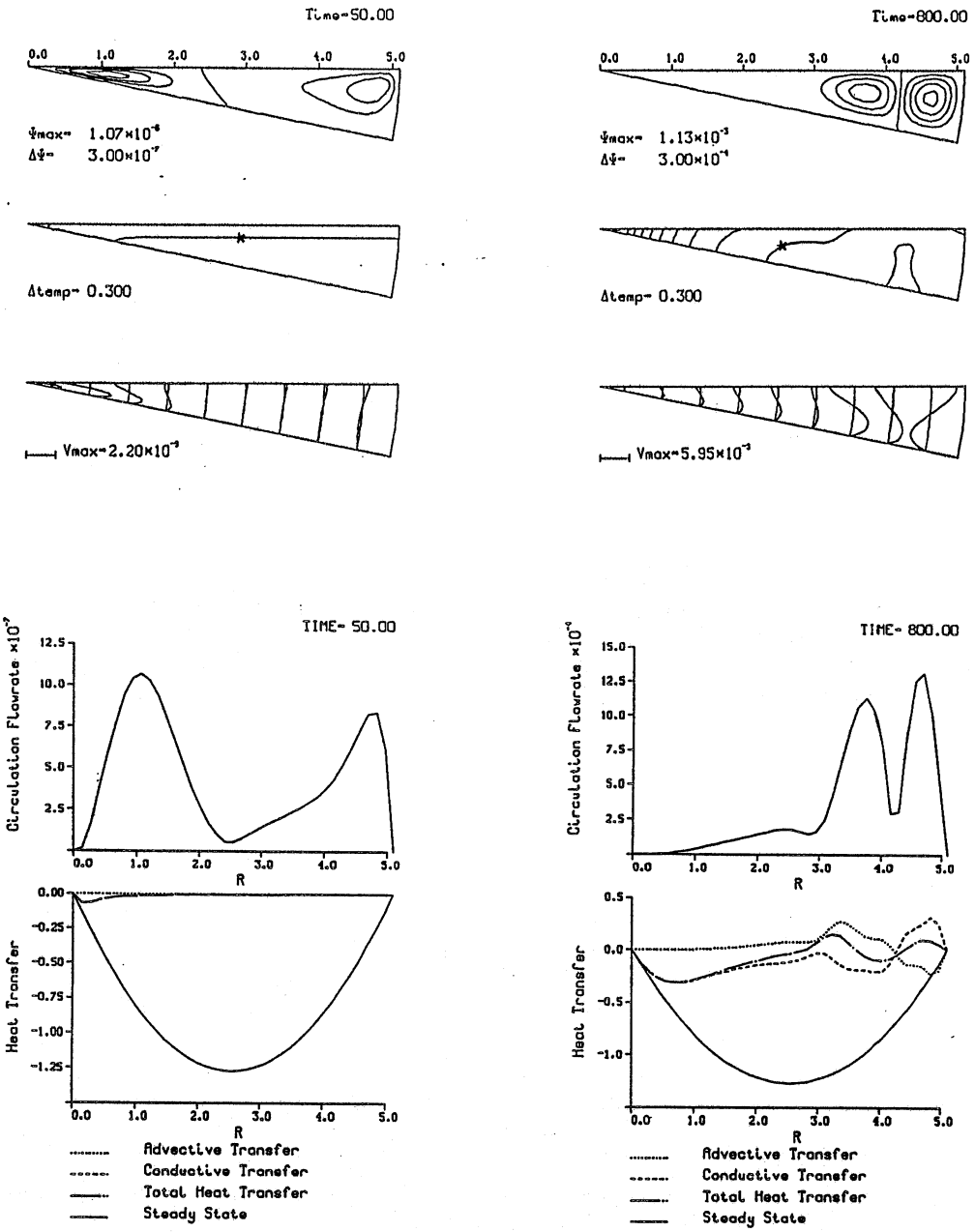

Fig. IV–1 Evolution of the flow for $Ra=10^4$, $Pr=10^3$, $S=0.2$. From top to bottom the instantaneous graphs represent: (i) streamlines, (ii) isotherms (* marks the T=0 isotherm), (iii) radial velocity profiles, (iv) horizontal circulation (Eq. III–18), (v) horizontal heat transfer (Eq. III–19).

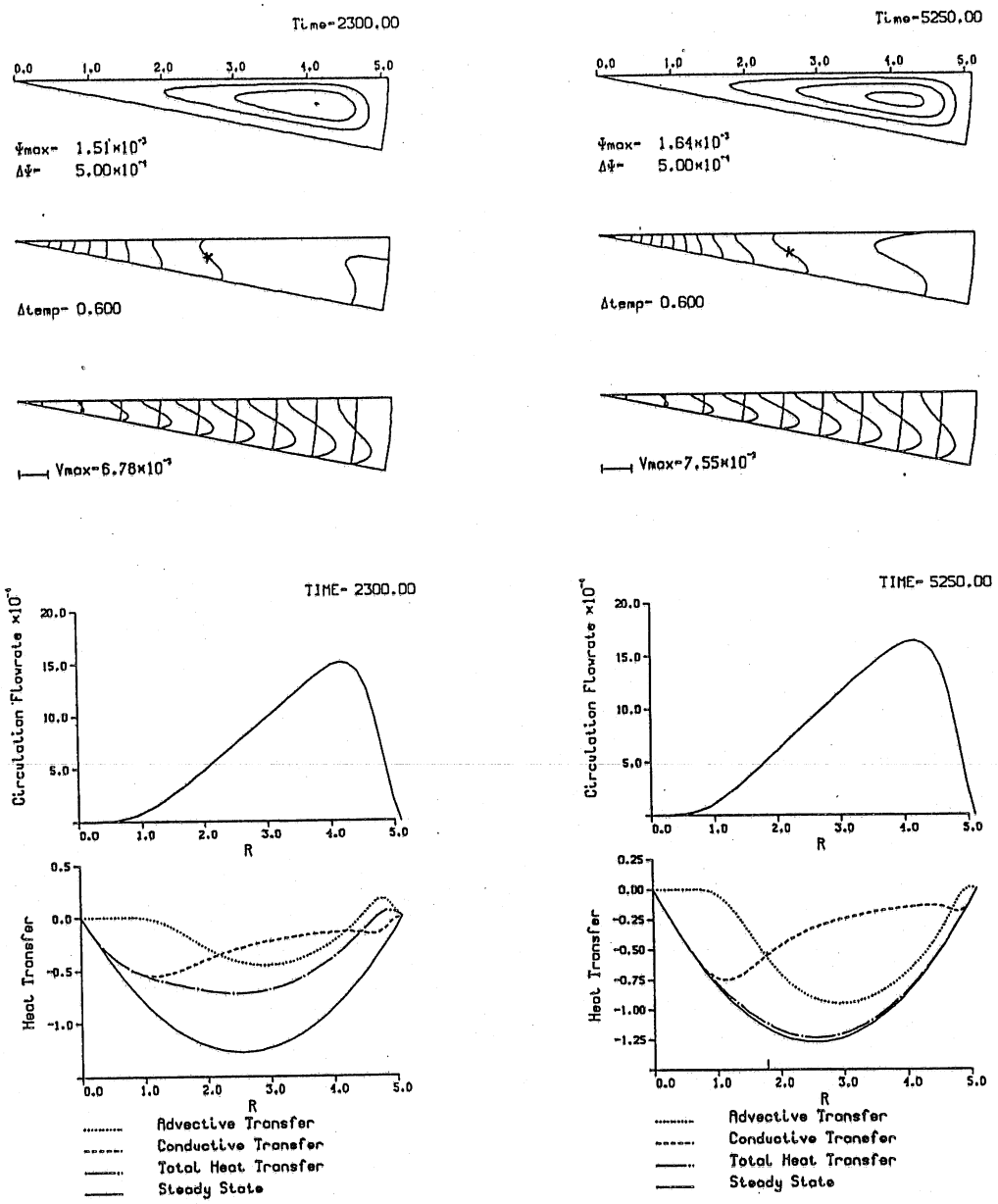

Fig. IV-1 (Continued)

Because the T=0 isotherm is parallel to the surface (Fig. IV–1), it can be inferred that at this time–instant the flow does not contribute to the heat transfer which is predominantly conductive. This is corroborated by the horizontal heat transfer graph, where the total heat transfer is separated into its conductive and advective components. (Caution, however, must be exercised in interpreting this graph because of possible cancellation effects of this two–layer flow.) At a later stage (t=800, Fig. IV–1) the isotherms and the heat transfer graph indicate the interaction of the flow with the heat transfer.

Figure IV–1b (t=2300) depicts the stage where the deep–end cell has been suppressed, and Fig. IV–1b (t=5250) shows the resulting steady–state. At steady–state the flow consists of one elongated cell which can be viewed as consisting of two layers. The heat transport in each layer is shown in Fig. IV–2; it can be seen that the corner where conduction dominates is shorter than might have been inferred from Fig. IV–1. Also, noteworthy is the cancellation effect of the advective transfer in the upper and lower layers. Finally, u_r time series at selected points appear in Fig. IV–3.

2. Dependence on Pr

A very interesting feature of the flow is its lack of dependence on the Pr number, for Pr values larger than 7 (which correspond e.g. to water at 20°C). The numerical calculations show that the velocities, which have been made dimensionless by the scale III–9, increase proportionally to $Pr^{-1/2}$. Because

$$\frac{u}{\frac{\nu}{h} Gr^{1/2}} = Ra^{-1/2}\ Pr^{-1/2}\ \frac{u}{\frac{\alpha}{h}} \qquad \text{(IV–1)}$$

it follows that, if the velocities are made dimensionless by α/h, they will be independent of Pr. This holds true for the entire period of development as well as for the steady state. Actually, it can be seen that, for the values reported in Tables IV–1 and IV–2, the velocity maximum (rescaled by α/h) for $Ra=10^4$, Pr=7 is within 0.5 percent of the maxima for $Pr = 10^2$ and $Pr = 10^3$ which are identical. Since the $u_i/a/h$ fields are identical for different Pr values, the same applies for the derivative quantity Q (Eq. III–18 and Table IV–2).

In summary, the following functional relations hold:

$$u_i(r,\theta,t) = \hat{u}_i(r,\theta,t,Ra,S)\ \frac{\alpha}{h}\ ,\ i=r,\theta \qquad \text{(IV–2)}$$

$$T(r,\theta,t) = \hat{T}(r,\theta,t,Ra,S)\ \frac{Hh}{k} \qquad \text{(IV–3)}$$

around a range of Ra values extending at least up to 10^6 (see below) and provided $Pr \geq 7$.

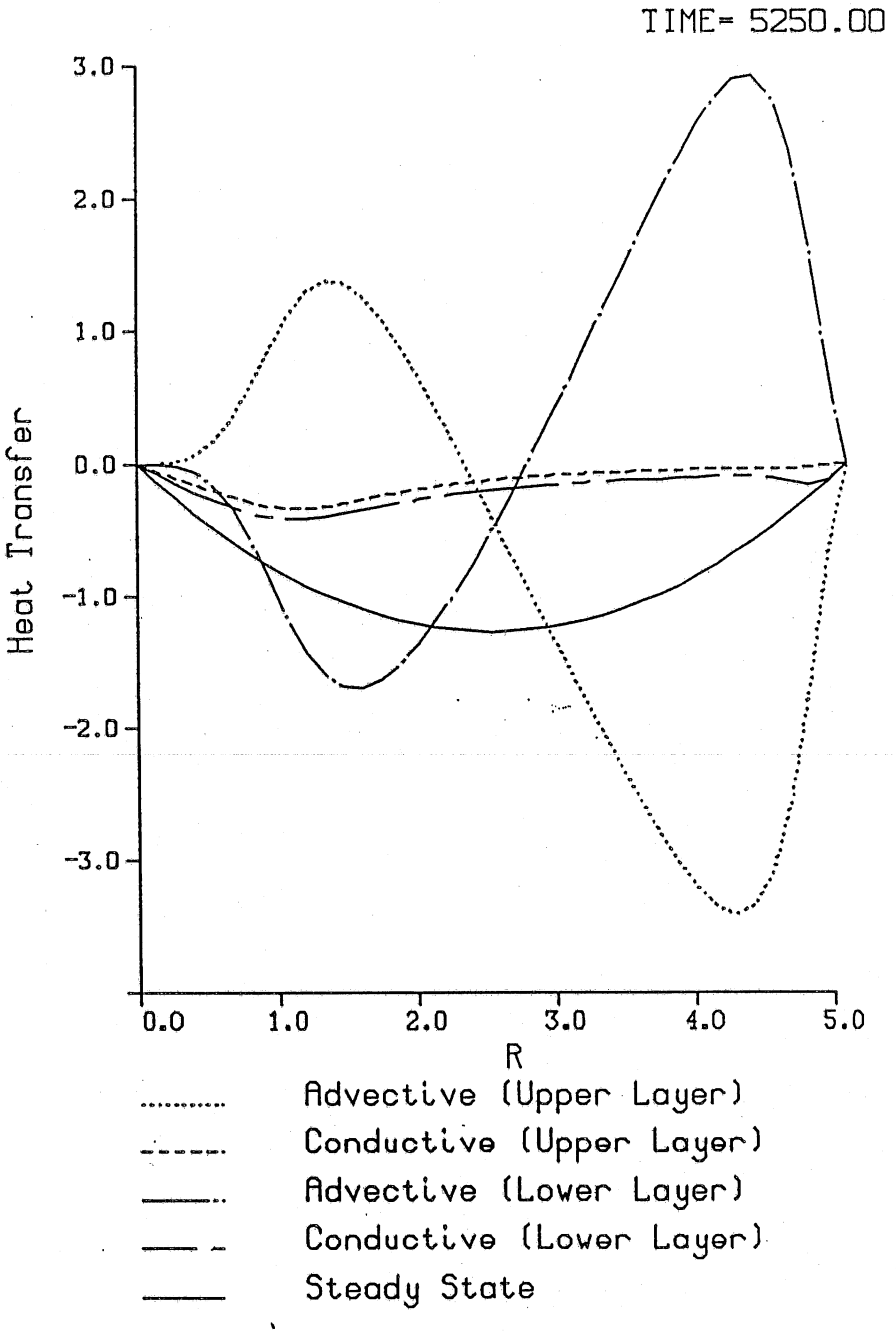

Fig. IV–2 **Total horizontal heat transfer in the lower and upper layers at steady state for Ra=10^4, Pr=10^3, S=0.2.**

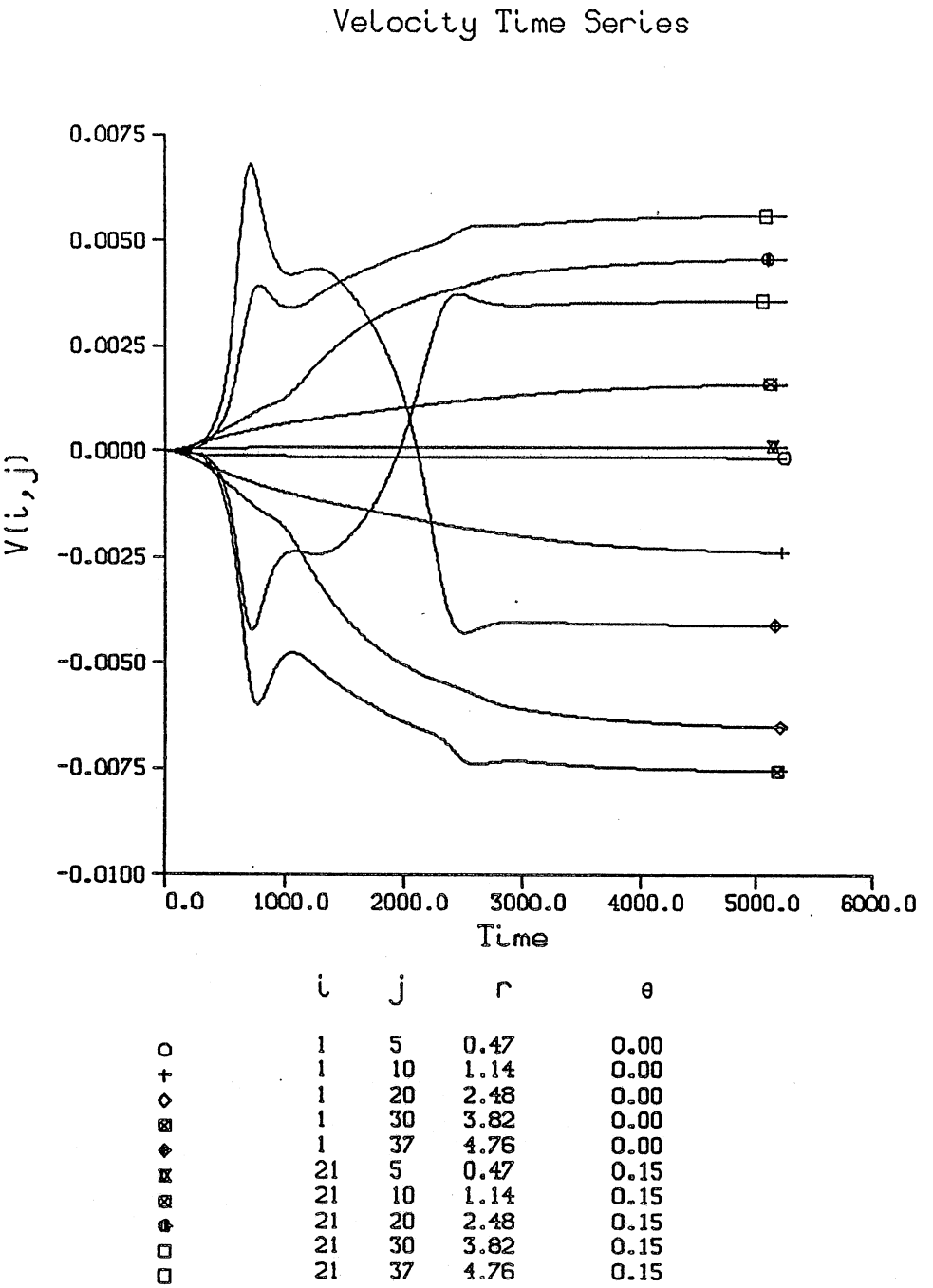

Fig. IV–3 Radial velocity (u_r) time series at selected points for $Ra=10^4$, $Pr=10^3$, $S=0.2$.

TABLE IV–1

Radial Velocity Maxima ($u_{r_{max}}$) at Steady State for Different Ra and Pr Values.
x is the exponent in $u_{r_{max}} = A\ Pr^x$

Pr	Ra=10^4	10^6	10^8
7	$9.01\ 10^{-2}$	$6.45\ 10^{-2}$	$4.10\ 10^{-2}$
10^2	$2.39\ 10^{-2}$	$1.78\ 10^{-2}$	$1.12\ 10^{-2}$
10^3	$7.55\ 10^{-3}$		
x	–0.50	–0.49	– 0.49

TABLE IV–2

Radial Flow Rate Maxima (Q_{max}) at Steady State for Different Ra and Pr Values.

Pr	Ra=10^4	10^6	10^{8*}
7	$1.96\ 10^{-2}$	$1.11\ 10^{-2}$	$6.85\ 10^{-3}$
10^2	$5.20\ 10^{-3}$	$3.00\ 10^{-3}$	$1.85\ 10^{-3}$
10^3	$1.64\ 10^{-3}$		

The important implication of this property of the flow is that the non–linear advective terms of the momentum equations are negligible. This is readily seen by examining a vorticity–type equation (in Cartesian coordinates for convenience) where u_i, T are rendered dimensionless as in Eqs. IV–2 and IV–3:

$$\frac{1}{Pr}\left[\frac{\partial}{\partial\hat{x}}\left[\frac{\partial\hat{v}}{\partial\hat{t}}+\hat{u}\frac{\partial\hat{v}}{\partial\hat{x}}+\hat{v}\frac{\partial\hat{v}}{\partial\hat{y}}\right]-\frac{\partial}{\partial\hat{y}}\left[\frac{\partial\hat{u}}{\partial\hat{t}}+\hat{u}\frac{\partial\hat{u}}{\partial\hat{x}}+\hat{v}\frac{\partial\hat{u}}{\partial\hat{y}}\right]\right]$$

$$=\frac{\partial}{\partial x}\nabla^2\hat{v}-\frac{\partial}{\partial y}\nabla^2 u+Ra\ \hat{T} \qquad \text{(IV–4)}$$

Since $\hat{u}$, $\hat{v}$, $\hat{T}$ are independent of Pr (Eqs. IV–2, IV–3) for large Pr, the advective terms have to be negligible. Effectively, the nonlinearities of this problem come from the advective terms of the energy equation, and the coupling, through buoyancy, of the momentum and energy equation. The Pr–independence of the appropriately scaled flow quantities is not a feature unique to the particular flow problem examined herein. In fact, as is well documented in the heat transfer literature, it seems to be common among natural convection flows in enclosures. For example, De Vahl Davis [1968] and Quon [1972] found that the steady, two–dimensional solutions of the flow in a square enclosure with differentially heated vertical walls is largely independent of Pr, for Ra values up to $\sim 10^6$. Mallinson and DeVahl Davis [1977] confirmed that this property of the flow also holds for three–dimensional solutions. These studies concluded that at Pr=7 the flow behaves as for infinite Pr, while the difference at Pr=1 is surprisingly small (of the order of a few percent).

Moore and Weiss [1973] studied the Rayleigh–Bénard problem by extracting two–dimensional numerical solutions. They found that for Pr values greater than unity, the Nusselt number is independent of Pr (termed the viscous regime). Also, the velocity scale they gave for this regime, i.e. $w \sim Ra^{2/3}\ \alpha/h$, is independent of Pr. The domain of validity of the viscous regime was found, however, to depend on the relative Ra and Pr values. Busse [1978] cites further evidence that for the Bénard problem Nu is independent of Pr, when Pr is larger than one; at this regime the stability properties of convection depend on the nonlinearities of the heat equation.

Thus, it can be seen that omission of the nonlinear terms in the analysis of the laminar convective littoral currents is a good approximation, just as it has been for other convective flows.

3. Accuracy of the Solutions

To appraise the accuracy of the calculations, solutions obtained at two different grids, one 30x15 (r–dir, θ–dir) and the other 40x25, for $Ra=10^4$, Pr=7, S=0.2, were compared. The grid was nonuniform in the θ–direction, progressively thinner towards the surface. The overall evolution of the flow was identical for the two different resolutions, with the boundary between the two cells (Fig. IV–4) being at the same position. As for any fixed grid calculation, however, of a flow that exhibits the transient formation and disappearance of cells, the calculation becomes less accurate when the extent of the disappearing cell becomes comparable to the spatial resolution. Thus, before t=35, the maximum radial velocity $u_{r_{max}}$ of the two solutions was within 5%, between t=35 and t=70, the difference was closed to 20%, with the maximum difference (25%) occurring at t=47.5 (see Fig. IV–4). Shortly before the disappearance of the deep–end cell, however, and up to the steady–state, the difference in $u_{r_{max}}$ between the two solutions is less than 0.2%.

The dimensionless time step used to calculate the solutions was 0.25, 0.5, 0.5 for Pr = 7, 10^2, 10^3, respectively. It can be verified a posteriori

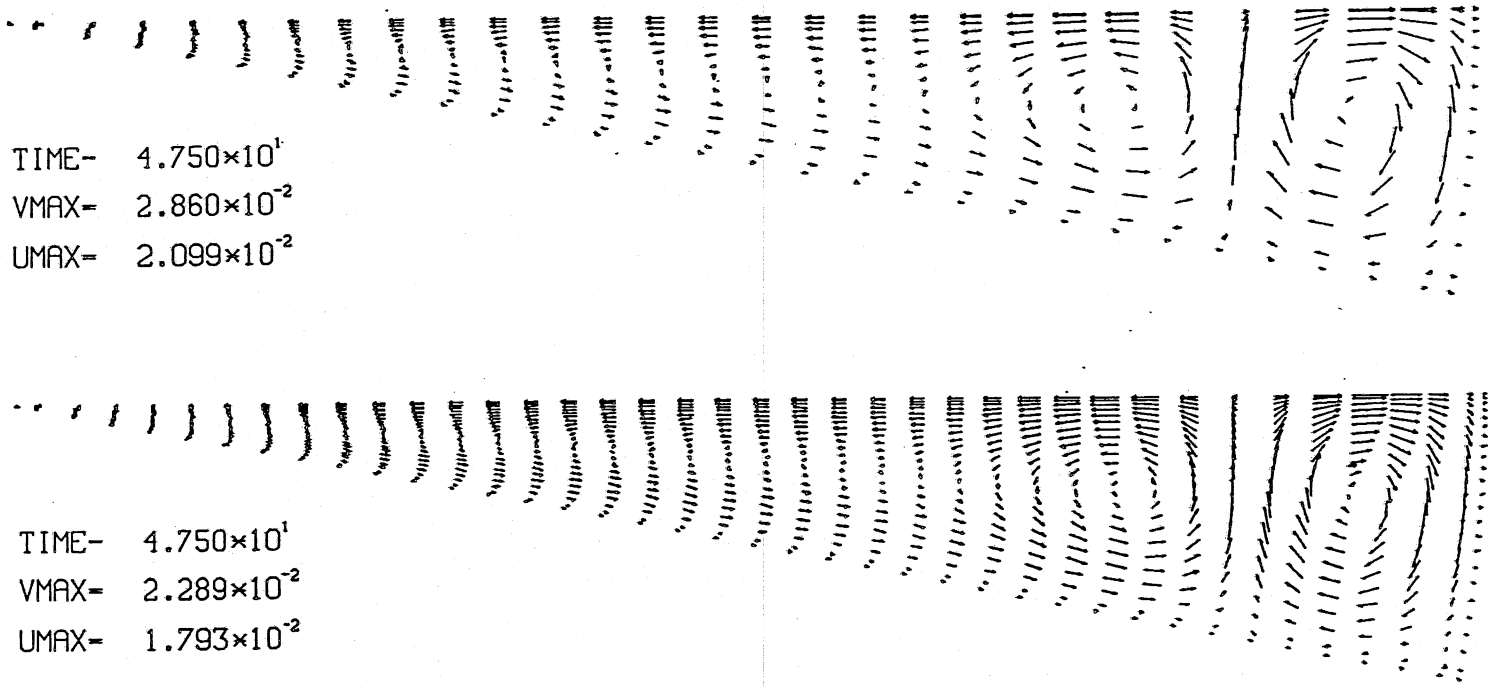

Fig. IV–4 Instantaneous velocity fields at t=47.5 for Ra=10^4, Pr=7, S=0.2 calculated on two different grids (a) 30x15 (upper) and (b) 25x40 (lower).

that with the grid and time step in use, a Courant number criterion is comformed to (although stability is not an issue since the method is fully implicit). An indirect verification that the time step was adequate comes from the higher Pr number solutions. The time step expressed in h^2/α time units (in which the solutions are virtually identical) is 9.45 10^{-4}, 5 10^{-4}, 1.58 10^{-4} for Pr = 7, 10^2, 10^3, respectively. Since decreasing the time step by a factor of six did not produce any differences, the original time step could be considered adequate.

C. INTERMEDIATE RAYLEIGH NUMBER REGIME: Ra = 10^6

1. Flow Evolution

A sequence of streamline, isotherm and radial velocity plots depicting the evolution of the flow at Ra = 10^6, Pr = 7, S = 0.1 appears in Fig. IV–5. The description of the main features of the flow is generic and applies also for Pr = 10^2 and for S = 0.2

The inception of the flow (Fig. IV–5, t=25) is quite similar to the inception at Ra = 10^4 described above. The first distinctive feature of this regime is shown in Fig. IV–5 (t=75), where it can be seen that the deep–end elongated cell breaks into smaller cells. Unlike the shallow–end cell, which is driven by the local, corner temperature gradient, the deep–end cells are the result of physical instability, i.e. they are the equivalent of Bénard cells. It can be recalled that at Ra=10^4 no such cells appeared. The second distinctive feature of the Ra=10^6 regime is that, just as for the Ra = 10^4 case, a steady state is eventually reached (Fig. IV–5, t=1250). This state consists of an elongated cell extending along the entire enclosure, with a secondary cell forming near the surface at the deep end. It is noteworthy that the single cell regime is reached relatively early in the evolution of the flow (around t=400, Fig. IV–5), whereas the steady state is reached at a much longer time (around t = 1100, Fig. IV–5). This can be also observed in Fig. IV–7 where time series of the radial velocity at selected points are plotted. After the initial development of the flow, steady state is reached through oscillations and minor adjustments of the flow. From the point of view of total radial heat transfer, it can be seen from Fig. IV–6 that these minor adjustments are important in reaching the steady, horizontal heat transfer.

The foregoing observation of the flow development raises a serious question. If several intermittent cells form, interact with each other, and finally merge into a single cell, it is possible, indeed probable, that the flow will be three– rather than two–dimensional. This situation is to be contrasted with the Ra=10^4 calculation, where the smooth progression from two to a single cell, makes it likely that the cells could be two–dimensional rolls. The more important question in the Ra=10^6 case is whether the single–main–cell at steady state results because of the procrustean restriction of the flow in two–dimensions.* The main justification, other than precedent, for carrying out two–dimensional rather than three–dimensional

*This raw practice, whereby an entity is reduced to a lesser dimension, would have likely appalled Procrustis himself.

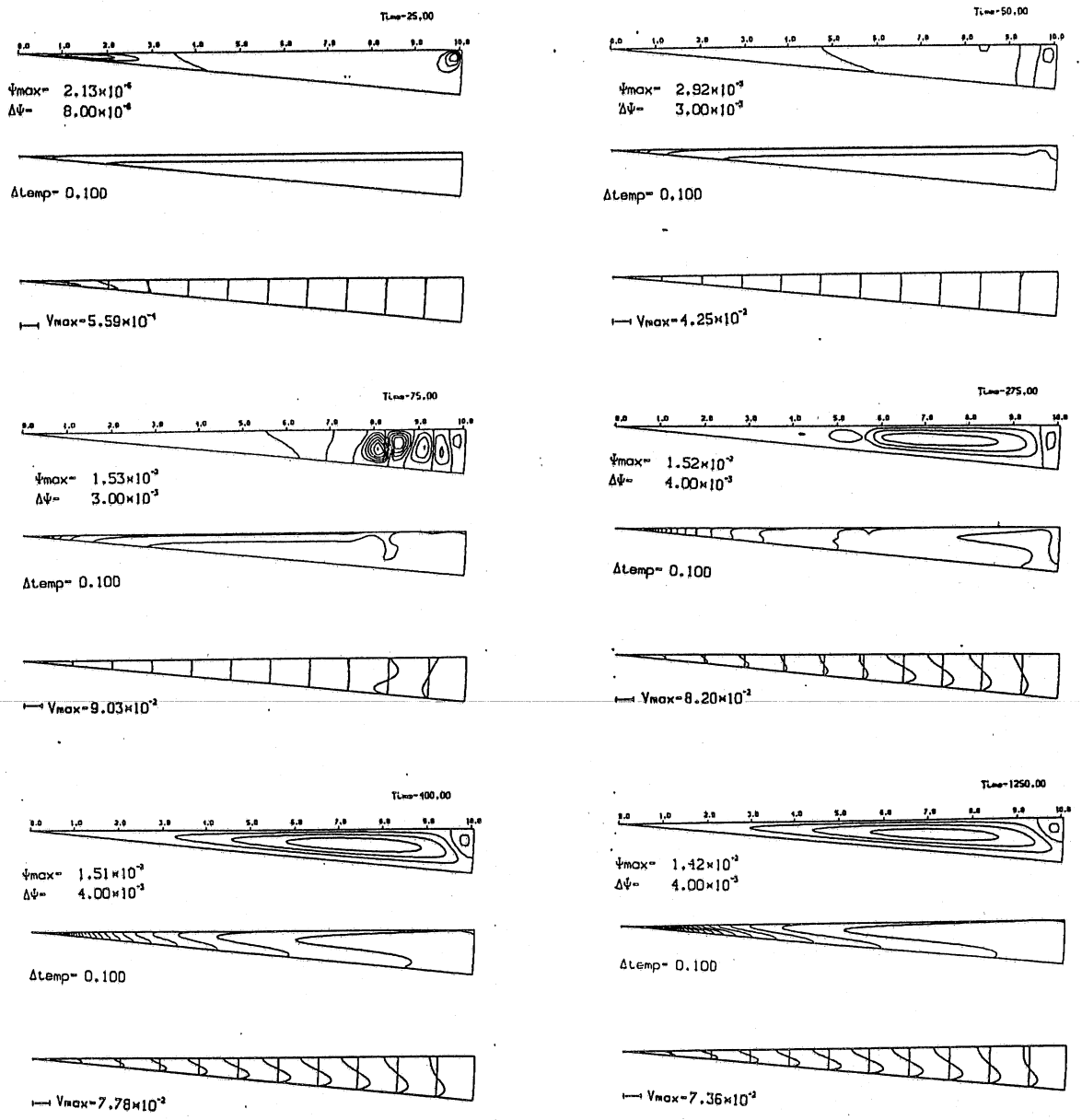

Fig. IV–5 Characteristic stages during the evolution of the Ra=10^6, Pr=7, S=0.1 flow on a 30x80 grid. At each time–instant plots of (from top to bottom) streamlines, isotherms and radial velocity profiles are included.

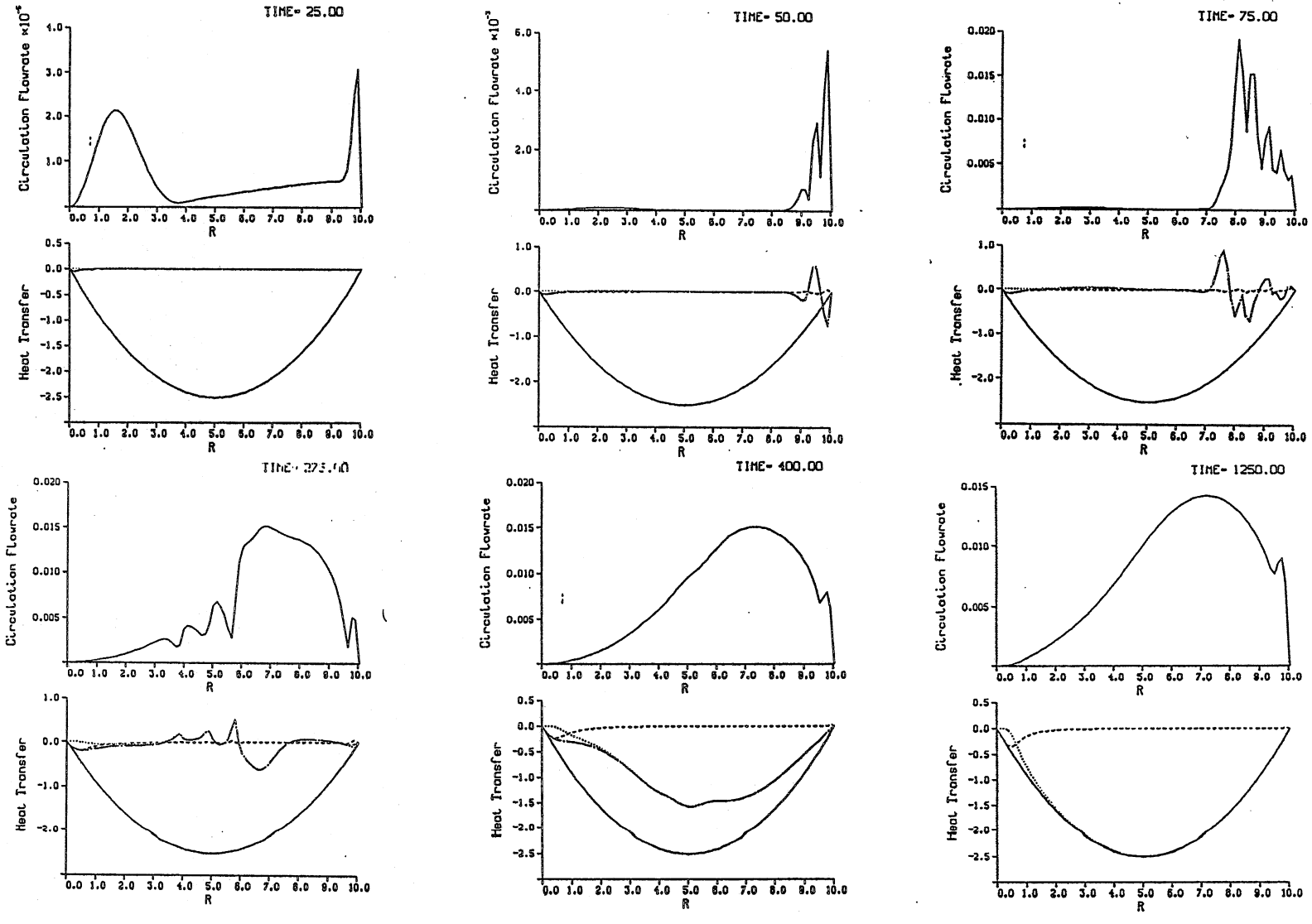

Fig. IV–6 Horizontal volumetric flowrate (Eq. III–18) and heat transfer rate (Eq. III–19) for each of the time instants depicted in Fig. IV–5.

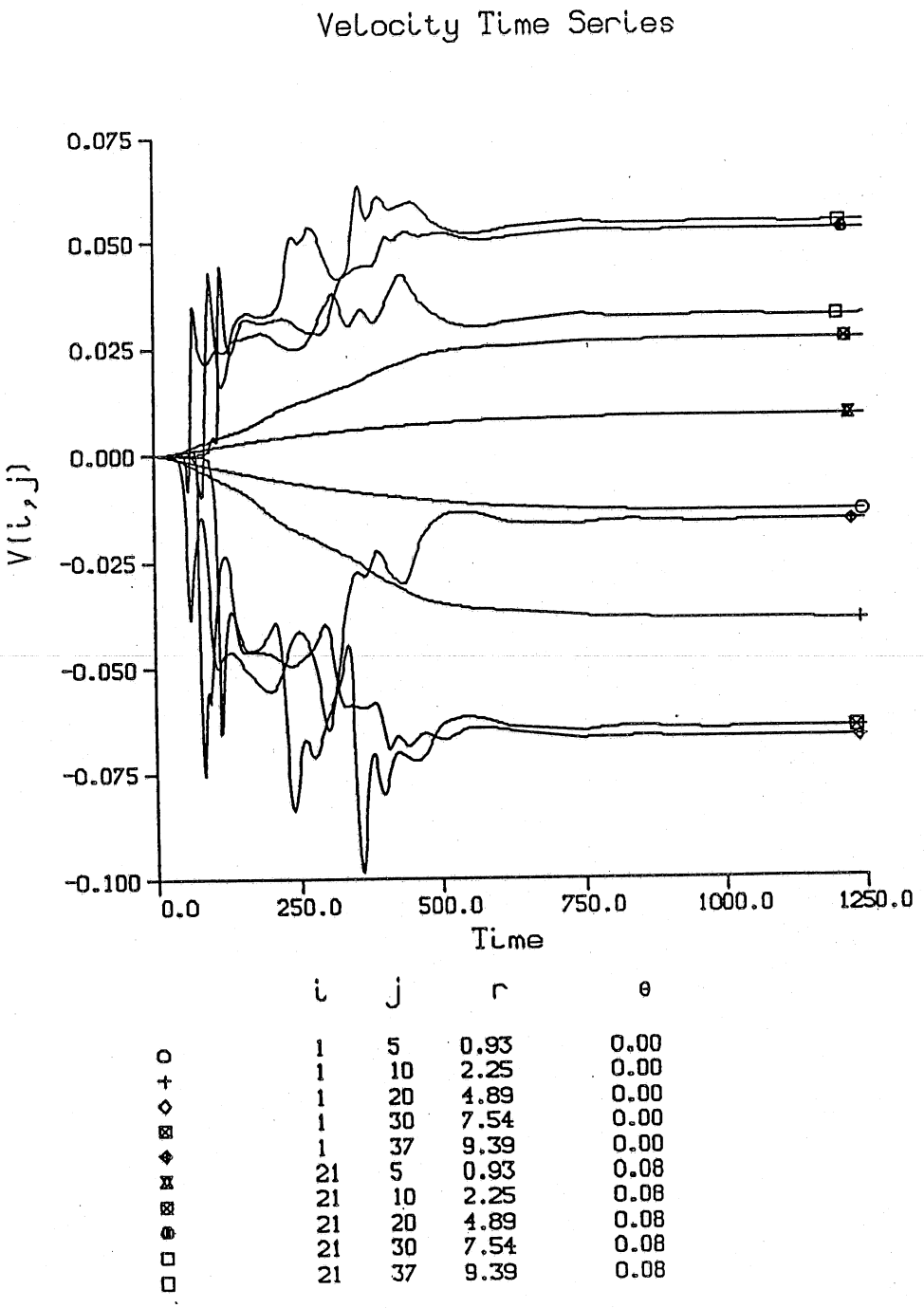

Fig. IV–7 Radial velocity (u_r) time series at selected points for Ra=10^6, Pr=7, S=0.1.

solutions is lack of a practical alternative because of the high cost of computation. (Not to mention the applicability of the results in "Flatland lakes".)

2. Dependence on Pr

The role of Pr for the solution at Ra = 10^6 is less clear than it is at Ra = 10^4, mainly because the unsteady part of the solution is less accurate. At steady state, it can be seen that, by rescaling the values given in Table IV–1 by α/h, the maximum of the velocity at Ra = 10^6 is 17.1, 17.8 for Pr = 7, 10^2, respectively. Unlike the Ra = 10^4 solution, however, the early stages of the evolution is different for each Pr value, with more vigorous cell velocities appearing at Pr = 10^2. Since it is rather unlikely that increase of Pr should have such an effect, it is more reasonable to attribute these differences to the different time–step size (Dt) of the solutions, especially in view that Dt = 9.45 10^{-5}, 5 10^{-5} for Pr = 7, 10^2, respectively. Nevertheless, the development stages parallel each other reasonably close, and it is clear that although the accuracy of the solutions would be improved with finer spatial resolution and finer timestep, the overall features of development would not change. (See Section 3 below.)

3. Accuracy of the Solutions

The accuracy of the original 25x40, Ra=10^6, Pr=7, S=0.1 solution was examined by making an additional run on a 30x80 grid. At steady–state the difference was 95% and 7% in terms of $u_{r_{max}}$ and 7% in terms of ψ_{max} (both maxima occur in the deep part of the domain). The finer grid solution revealed, however, the inadequacy of the discretization of the coarser grid at the pointed–end of the domain, since, ΔT_b = 8.48 for the 30x80 solution while ΔT_b = 6.93 for the 25x40 (18% difference). The reason for this discrepancy can be seen in Fig. IV–8, where the sharp corner–temperature drop is illustrated, and the bottom temperature profiles for the two different grids compared. The fact that the two profiles virtually coincide beyond r=2 and since, in addition, the flow quantities are within less than 1% (at steady–state), indicate that the corner–layer where conduction is dominant does not influence the flow very much (an attempt to analyze this corner–layer appears in Appendix IV). During the initial period of flow development, the calculations show that the grid significantly influences both the location and strength of the convection cells. This is shown in Fig. IV–9, where the calculated fields (u,v,t) at t=100 are shown for the two different grids (30x80 upper, 25x40 lower). The characteristic stages, however, such as the formation of cells, and the merging of cells to form one main cell (Fig. IV–5) are closely paralleled in the two grids (e.g. Fig. IV–9). In terms of maxima, for t < 500 the difference in $u_{r_{max}}$ is up to 25% and in and in ψ_{max} up to 30%. After this t > 500) the differences drop at 1.5% for ψ_{max} and 1% for $u_{r_{max}}$. The sensitivity of the flow pattern to the grid size is a strong indication of how delicate the flow is, and this extends, presumably, to the initial condition. It seems thus pointless to seek fine–grid solution for the initial period, especially since the main interest here is in an estimate of the time–scale to steady state and in characteristic velocities. Consequently, it was decided to check the accuracy of the Ra = 10^6, Pr = 7, S = 0.2 (higher slope) solution for the

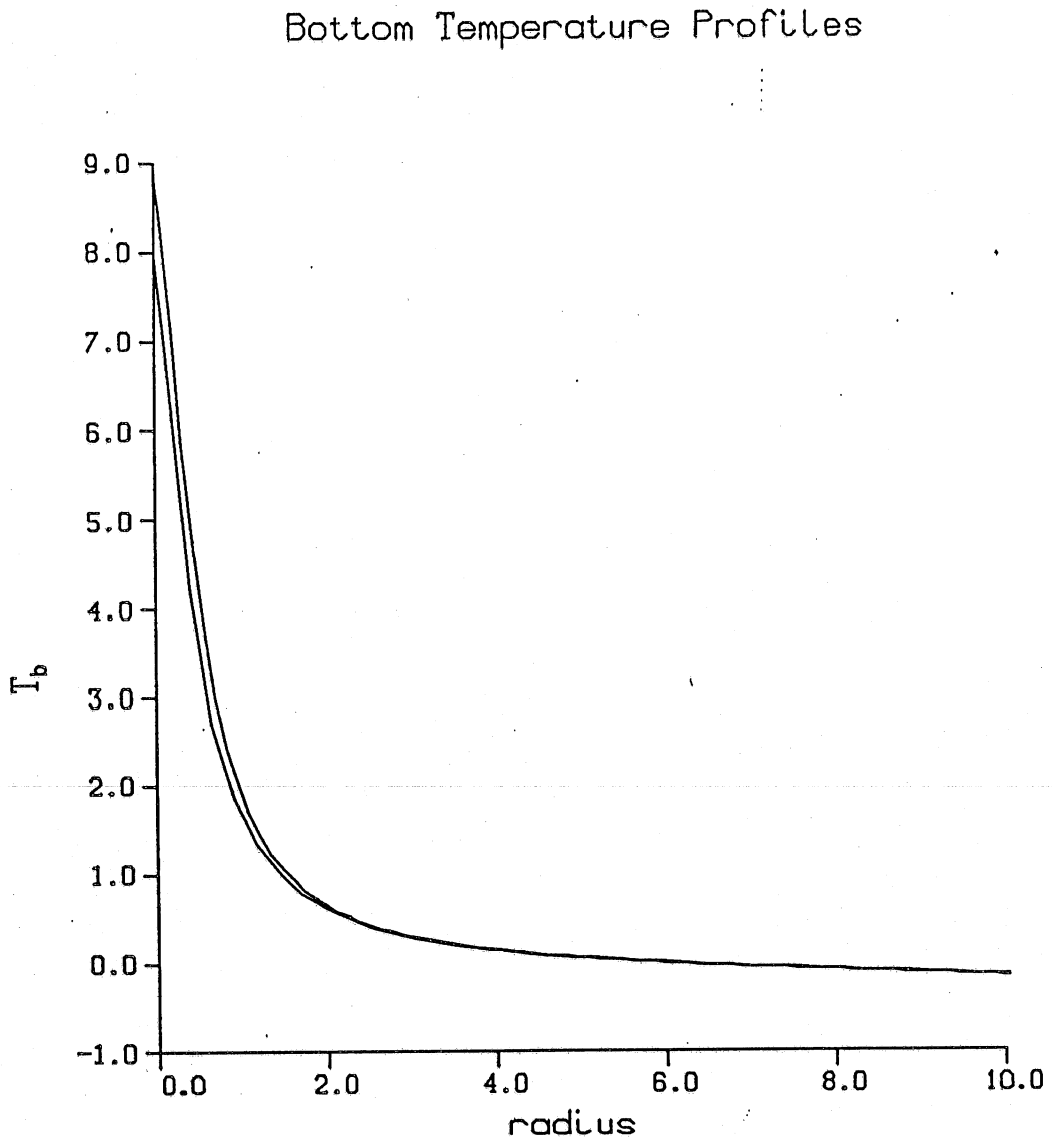

Fig. IV–8 Bottom temperature profile for Ra=10^6, Pr=7, S=0.1 on two different grids: 30x80 (upper curve), 25x40 (lower curve).

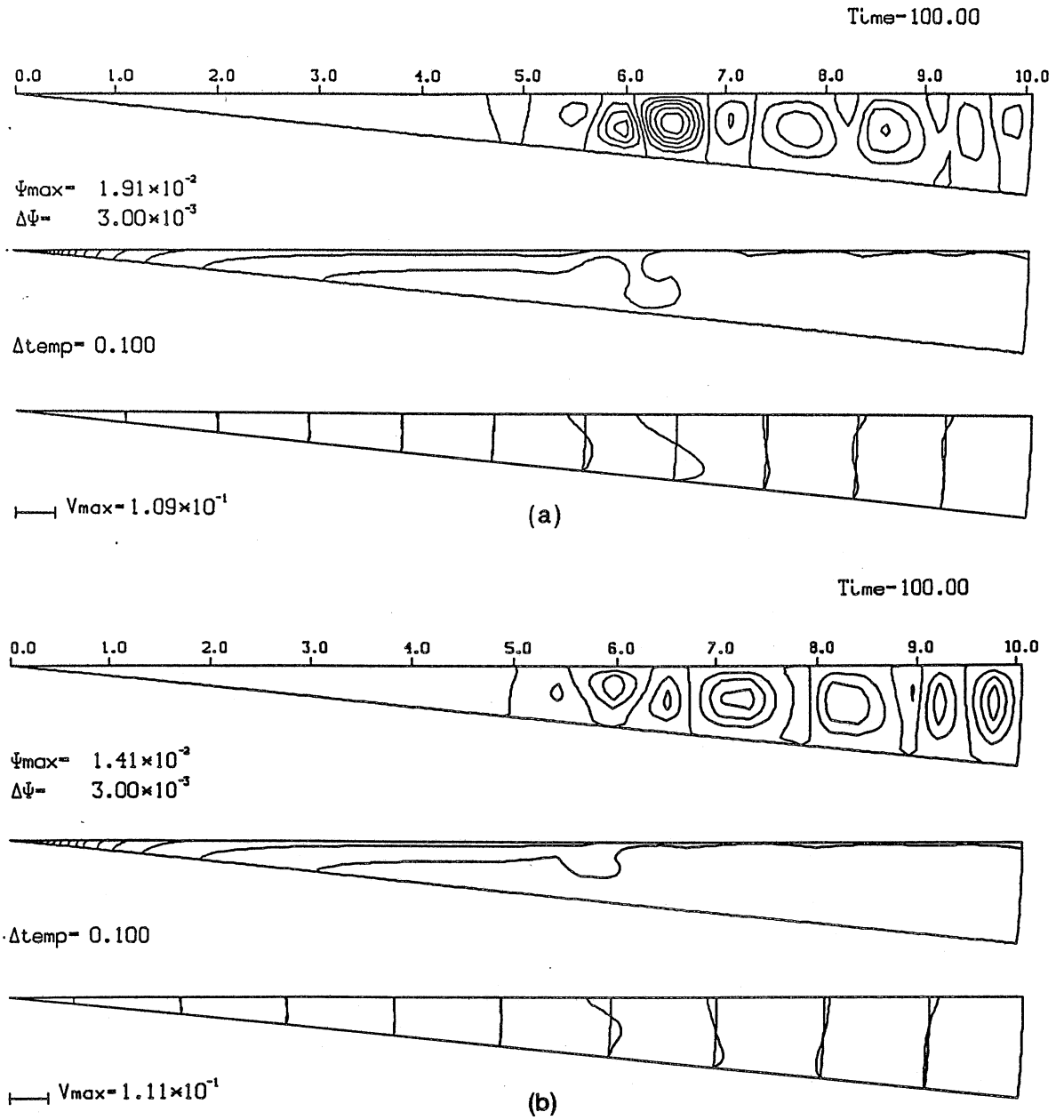

Fig. IV–9 Instantaneous streamlines, isotherms and radial velocity profiles for $Ra=10^6$, $Pr=7$, $S=0.1$ on two different grids (a) 30x80 (b) 25x40.

steady–state only. To this end, the steady state of the 25x40 grid was interpolated on a 30x80 grid, in order to get a close initial guess. This procedure was first tested for the S = 0.1 slope where the full unsteady solutions were available on both grids. Surprisingly it was found that a steady solution was obtained only through the method of false transients; otherwise the iterations diverged (except for impractically heavy underrelaxation). An explanation can be based on the observation (Fig. IV–10) that the initial conditions on the fine grid introduce small oscillations to the flow. If the flow is calculated as unsteady, the oscillations soon die out, and the steady solution is identical to the solution calculated from zero initial conditions. If, however, the "time step" is too large, these small disturbances are significant enough to cause divergence.

By applying this sort of refinement, the solutions at Ra = 10^6, Pr = 7, S = 0.2, or grids 25x40 and 30x80 were found to differ 0.5 in $u_{r_{max}}$ and less than 0.1 in ψ_{max}.

The effect of the time–step on the accuracy of the solution has been discussed in the section on Pr effects.

4. Comparison with Flow in an "Attic Space"

It is interesting to contrast the evolution of the flow described above, with flow developing in an attic space under night–time conditions [Poulikakos and Bejan, 1983]. "Attic space" describes a triangular geometry (wedge–like) with the upper wall sloping and the lower horizontal. Night–time conditions are represented by holding the sloping wall at constant low temperature and the horizontal bottom at constant high temperature. This arrangement can be considered as a variation of the Bénard setting, with the upper plate at a slope instead of horizontal. Thus viewed, the natural question arises whether this flow will consist of Bénard–like cells or not. A series of numerical solutions at aspect ratios (height to length) 0.2, 0.4 1.0 and Rayleigh numbers ($Ra_{\Delta T}$, i.e. based on ΔT rather than H) up to $6x10^5$ revealed that the flow evolved from quiescent and isothermal initial conditions to a single cell at steady–state, through a single–cell spin–up, albeit with transient oscillation. Even if the blatant difference of the boundary conditions is ignored, a comparison of the attic space flow with the flow studied herein is meaningful only if a rough equivalence between the different definitions of Ra is established. Using the notation adopted above:

$$Ra_{\Delta T} = \frac{g\beta\ \Delta T\ h^3}{\alpha\nu} \qquad \text{(IV–5)}$$

From the definition of Nusselt number Nu:

$$Nu = \frac{H\,\ell}{\frac{k\Delta T}{h}\,\ell} \qquad \text{(IV–6)}$$

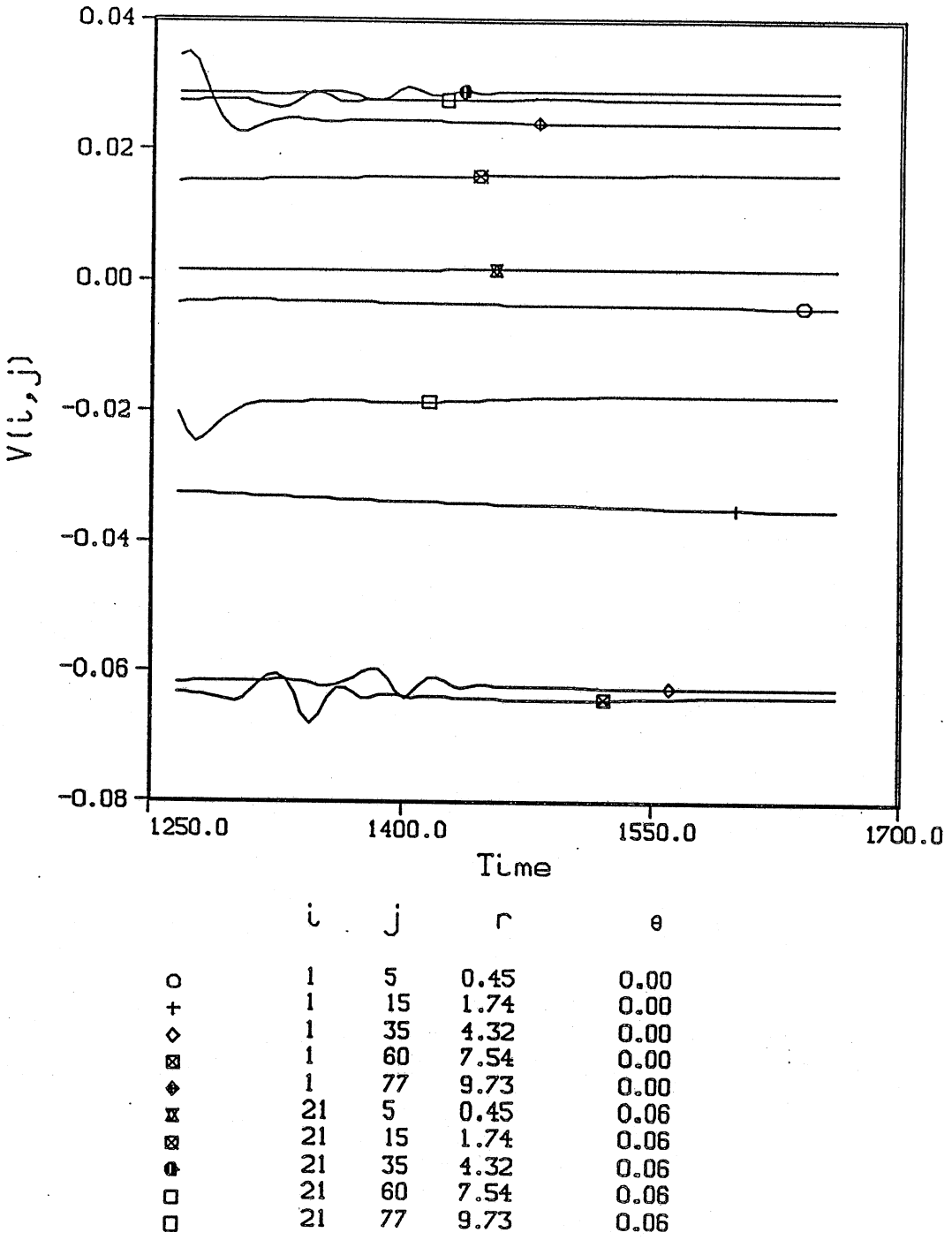

Fig. IV–10 Evolution of disturbances to the velocity field close to steady state for $Ra=10^6$, $Pr=7$, $S=0.1$ on a 30x80 grid. The disturbances are introduced by interpolation of the steady state on a coarser grid (25x40).

the average heat flux H on either boundary is:

$$H = k \frac{\Delta T}{h} Nu \qquad \text{(IV–7)}$$

Denoting Ra_H the Ra given by Eq. III–12,

$$Ra_H = Nu\ Ra_{\Delta T} \qquad \text{(IV–8)}$$

Since an attic space calculation for $Ra_{\Delta T} = 6x10^5$ gave $Nu \simeq 6.5$, it follows that $Ra_H = 3.9x10^6$. It is thus established that for values of the parameters reasonably close ($Ra_H = 3.9\ 10^6$, $Pr = 6$, $S = 0.2$, for the attic space and $Ra = 10^6$, $Pr = 7$, $S = 0.2$ for the littoral slope) the two problems exhibit an entirely different evolution.

The reason for this significant difference is clear. In the attic space problem, the cold, sloping boundary is not perpendicular to gravity. The flow is initiated all along this boundary and proceeds to steady state through a spin–up. In the littoral slope problem, the only thermally active boundary is horizontal, so that flow is generated only after a local horizontal gradient is created by vertical heat transfer.

It is interesting, however, to note that the values of the maximum circulation flow rate at steady–state are reasonably close at similar values of the independent parameters (Table IV–3). In spite of these similarities, the two problems are fundamentally different in the limit as $S \to 0$ (see section IV–G).

TABLE IV–3

Comparison of the Maximum Flow Rate Between the Attic Space and Littoral Slope Calculations

	Ra_H	Pr	Ψ/ν
Littoral Slope	10^4	7	0.74
Littoral Scope	10^6	7	4.2
Attic Space	$2.7\ 10^5$	0.72	3.7

D. HIGH RAYLEIGH NUMBER REGIME: Ra = 10^8

1. Introduction

The low– and intermediate–Rayleigh number solutions are instructive since they illustrate the essential features of the flow devoid of any of the complications that occur at higher Ra values. They do not, however, scale "immediately" up to water flows of realistic dimensions (although scaling can be reinterpreted using apparent viscosities, see Chapter V). At Ra = 10^8, the point is reached where the flow in a realistic laboratory size tank can be simulated. Unfortunately, several grave problems arise when a Ra = 10^8 calculation is attempted. As can be anticipated from the Ra = 10^6 solution, the difficulties stem from the three–dimensionality of the flow and accuracy of the solution on affordable grids. These problems are aggravated because, in contrast to the Ra = 10^6 flow, at Ra = 10^8 the single cell configuration is no longer stable (even in two dimensions) and consequently the solution is time–dependent even beyond the initial development.

The ultimate justification for performing two–dimensional calculations of a flow expected to exhibit three–dimensional behavior is lack of practical alternatives. An adequately discretized three–dimensional solution at Ra = 10^8 is prohibitively expensive. Even a large–eddy simulation [e.g. Grötzbach, 1982] of the entire evolution of the flow is impractical. It is therefore reasonable to exhaust the information that can be extracted from the two–dimensional model by performing calculations in the time–dependent regime of the flow. To put these two–dimensional calculations of a three–dimensional flow into perspective, the conclusions from similar numerical experiments reported in the literature are briefly reviewed.

Comparison of specific aspects of two–versus three–dimensional calculations appear in the literature for both the Bénard and the differentially heated side–wall settings. Freitas et al. [1985] compared two– and three–dimensional numerical solutions of a confined Bénard flow at Ra = 1.7 10^8. They concluded that the two–dimensional flow appeared more organized with flow structures having longer time–scales and larger length–scales. Lipps and Somerville [1971] studied the increase of cell wavelength with Ra for Bénard convection for Ra values up to 8000. Their initial–value calculations showed that when the space domain was several times the expected wavelength their three–dimensional solutions settled to all wavelengths in reasonable agreement with experimental values, whereas the two–dimensional solutions produced wavelengths shorter than the experimental, even in the range of the parameters where the flow is essentially two–dimensional. Lipps [1976] extended the three–dimensional calculations up to Ra = 25,000. He found that the Nusselt number is very nearly the same for two– and three–dimensional solutions. At the higher Ra, however, the wavelength of the two–dimensional solutions was found higher than the three–dimensional ones.

Mallinson and DeVahl Davis [1977] studied the enclosure with differentially heated end walls by extracting three–dimensional numerical solutions for Ra up to 10^6. They found that two–dimensional solutions produced a fair approximation to the average Nusselt number (less than 3% difference at Ra = 10^6) and noted that for high Ra and Pr the

two–dimensional model is adequate (provided that the three–dimensional enclosure is not narrow). Similar conclusions were reached by Lai and Ramsey [1987].

2. Time–Dependent Regime – Time–Averaged Quantities

The initial development of the flow at Ra = 10^8, Pr = 7, S = 0.2 from isothermal and quiescent initial conditions is similar to the already described initiation of flow at Ra = 10^6. The important difference between these two flows is that the one–main–cell configuration, which represents a steady state at Ra = 10^6, is no longer stable at Ra = 10^8. This is expected for flows of sufficiently high Ra values, such as those developing in natural scale, or even those observed in the laboratory (see Chapter VI for experiments at Ra ~ 10^{10}). The range around Ra = 10^8 is also where the thermal boundary layer that forms at the surface of a fluid layer cooled from above becomes intermittent (i.e. time–dependent) [Foster, 1971]. The recurrent formation and disappearance of ephemeral secondary cells that disrupt to varying degrees the horizontal flow is depicted in Fig. IV–11a, b. Remarkable in these figures is how uniform the temperature in the bulk of the domain is, compared to the sharp temperature drop at the shallow corner.

The time–averaged streamlines and isotherms are shown in Fig. VI–12. These quantities have been averaged over a time–interval that excludes the initial development. The criterion for the adequacy of the averaging interval was based on the closeness of the time–averaged, "depth" integrated (i.e. integrated over the angular direction) heat transfer with the steady–state values of this quantity (Eq. III–23). This criterion is arbitrary insofar as the degree of closeness of the two curves is arbitrary; it was found that different degrees of proximity resulted in differences of a few percent in mean values of Q_{max} and $v_{r_{max}}$. For the time interval chosen for the mean plots of Fig. IV–12, the time–averaged depth–integrated flow rate and heat transfer appear in Fig. IV–13, where it can be seen that the time–averaged heat transfer rate visually coincides with its steady–state space distribution. The standard deviation of the Q and $\bar{H}$ curves normalized by the local mean values are presented in Fig. IV–14. The shape of these curves, which initially increase linearly and then abruptly become almost constant, indicates a depth scale beyond which the flow is less dependent upon the local depth.

3. Spatial Resolution Criteria—Accuracy

For the numerical solution to the qualitatively correct, the intrinsic length scales of the problem have to be adequately discretized. The horizontal grid size is constrained by the length scale of the developing surface instability and the scale of the convective cells (thermals) that develop past marginal stability, while the vertical solution is constrained by the thickness of the surface thermal boundary layer. Estimates for each of these were used to make the grid of a Ra = 10^8, S = 0.2 and 0.1, Pr = 7 (which represents water of 20° C) run.

The stability of a fluid cooled from above has been studied analytically and experimentally by Foster (1965a,b). According to his calculations, at

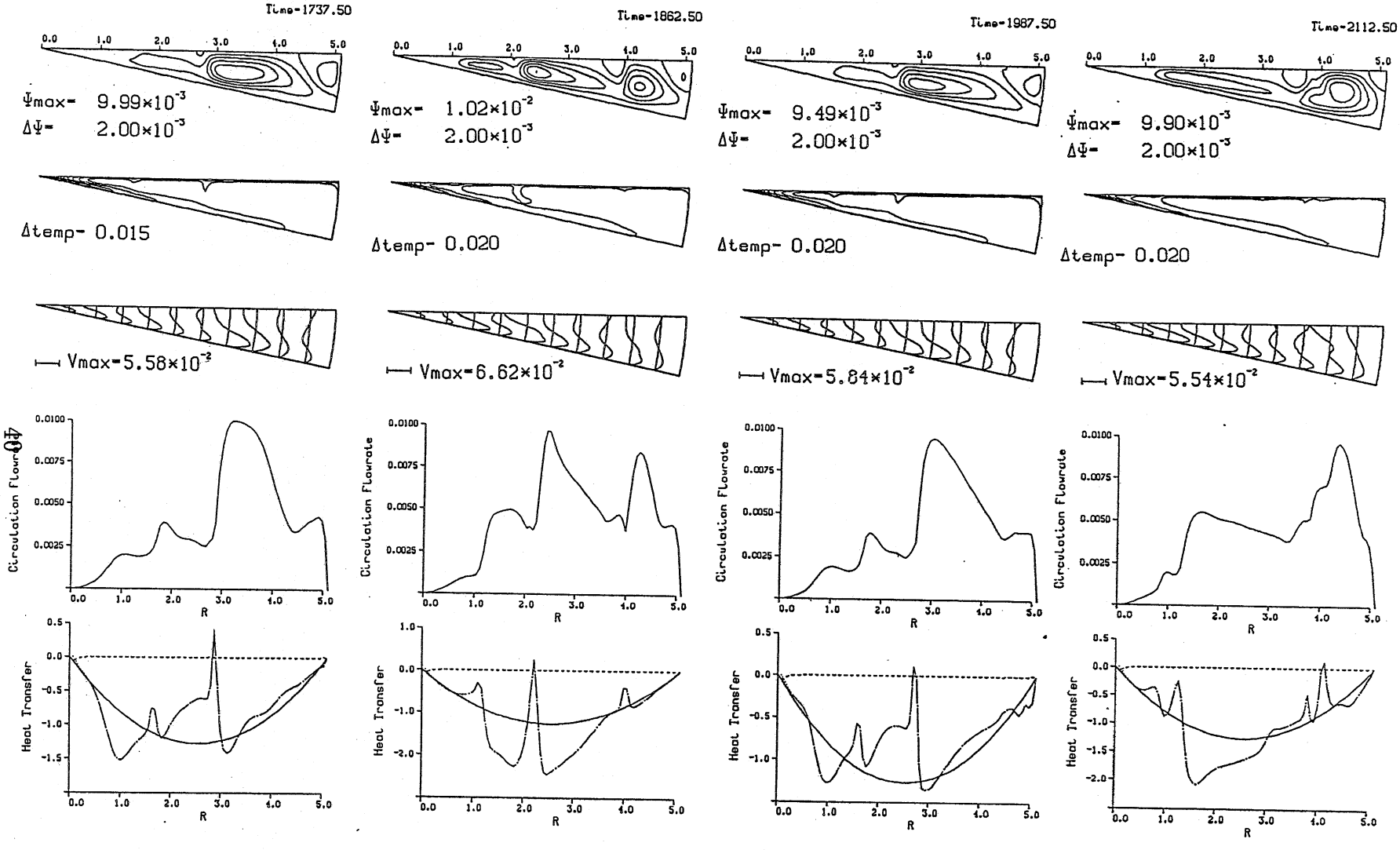

Fig. IV–11. Time–instants in the evolution of the Ra=10^8, Pr=7, S=0.2 flow. Included at each instant are (top to bottom) streamlines, isotherms, radial velocity profiles, horizontal flowrate and horizontal heat transfer.

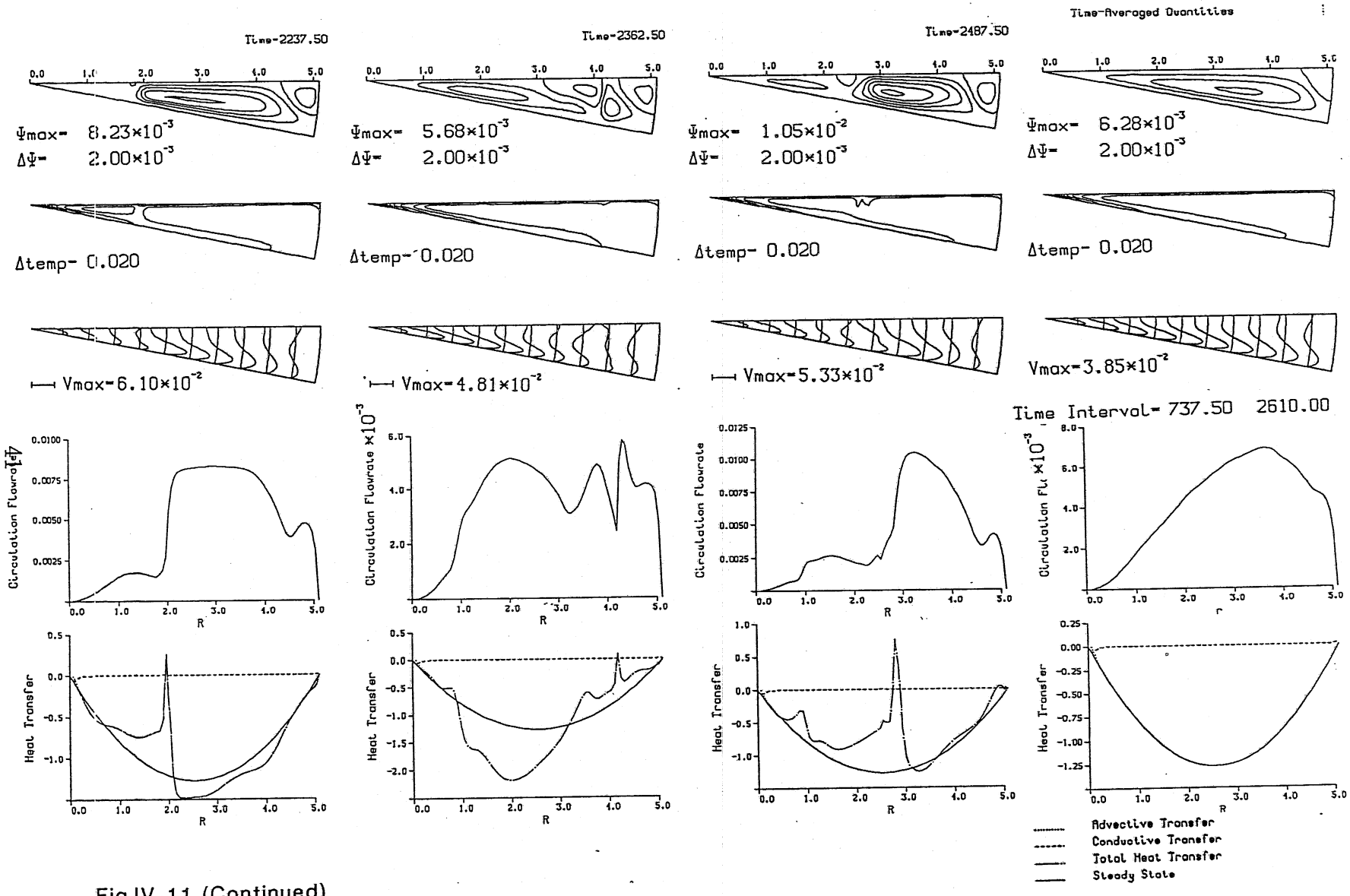

Fig.IV-11 (Continued)

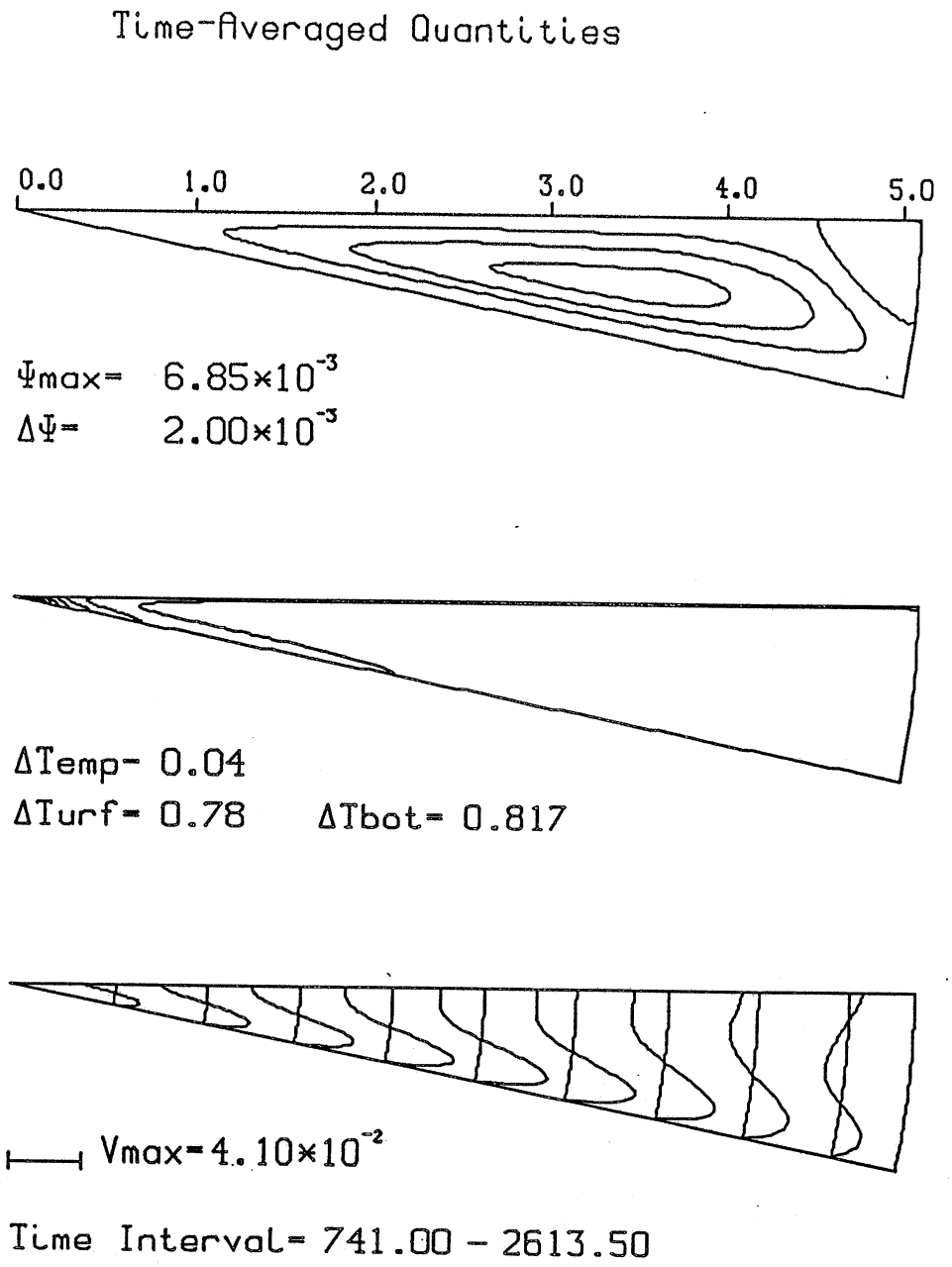

Fig. IV–12 Streamlines, isotherms and radial velocity profiles (top to bottom) resulting from averaging within the developed time-dependent state of Ra=10^8, Pr=7, S=0.2 on a 60x120 grid.

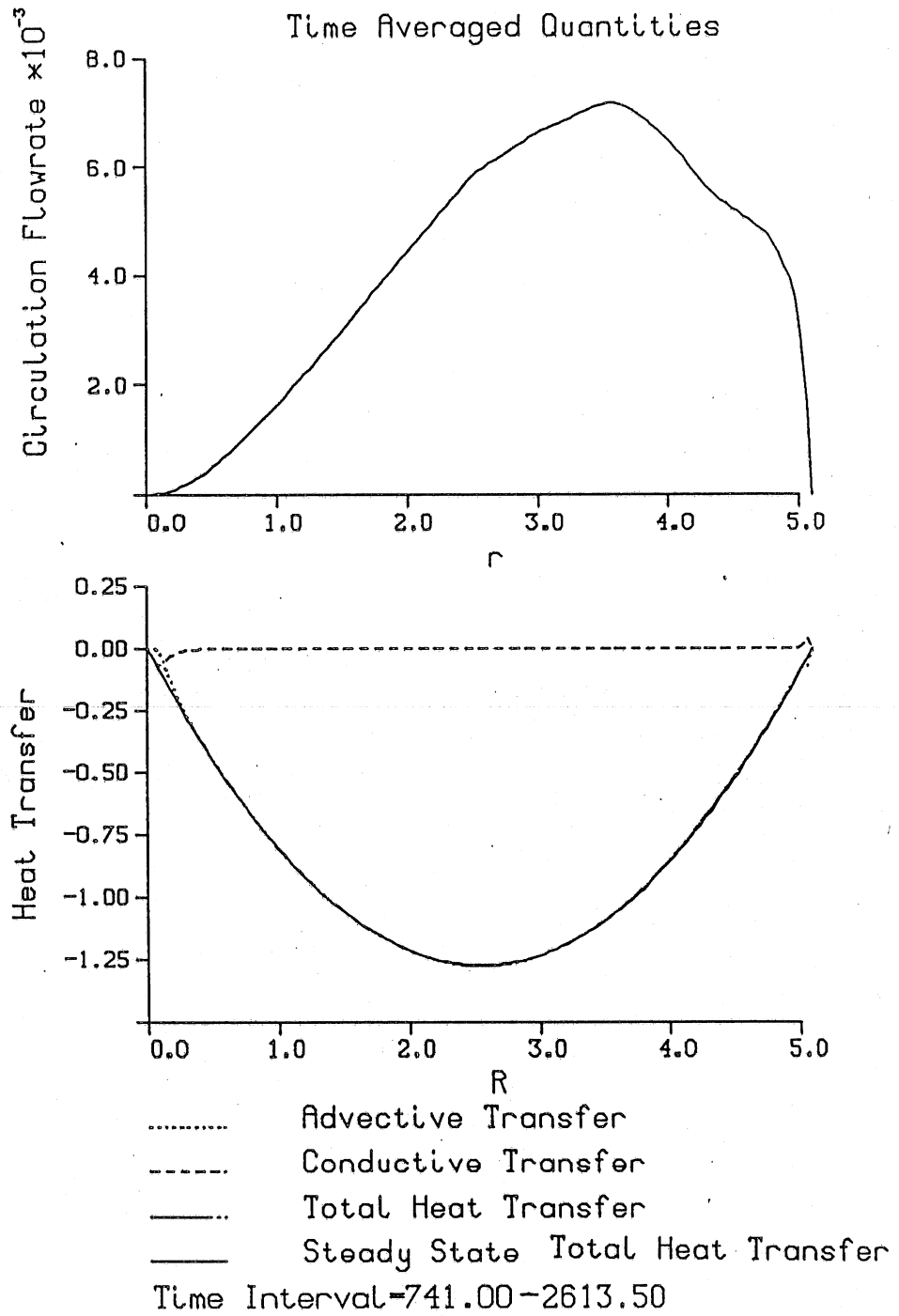

Fig. IV–13 Time–averaged flowrate and horizontal heat transfer corresponding to fields depicted in Fig. IV–12.

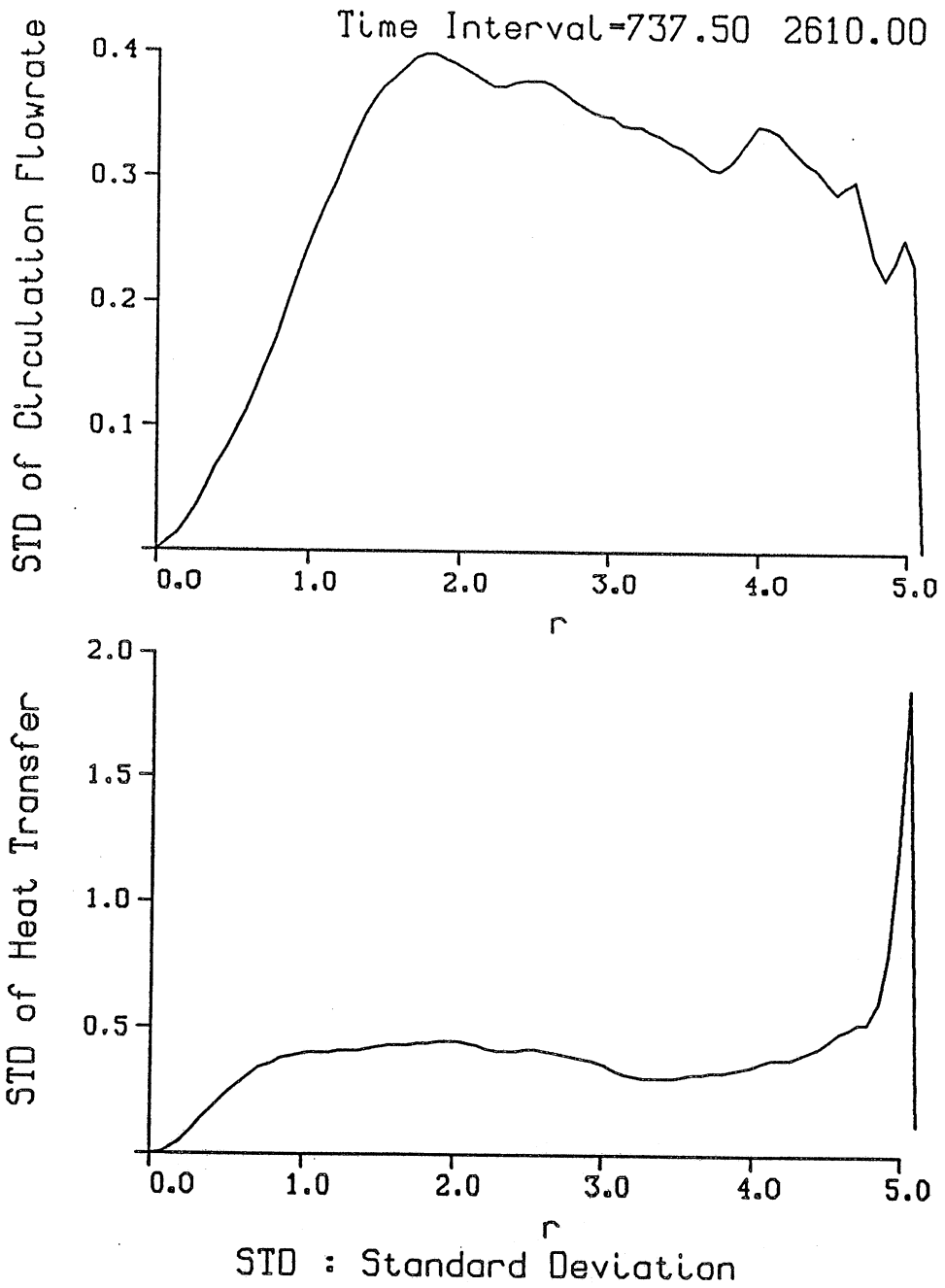

Fig. IV-14 Standard deviation corresponding to the mean fields shown in Fig. IV–13 .

$Ra = 10^8$, the most unstable wavelength is $\lambda = 0.57$ (wavenumber a = 11). As surface temperature boundary condition, he used linearly decreasing temperature instead of constant heat flux, which is used here. Nevertheless, since the surface temperature drop caused by a constant surface heat flux drops linearly for a short time, and since the theory compared well with an experiment using a very nearly constant heat flux, use of Foster's results is appropriate. The dimensionless grid size $\Delta x/h$, where Δx is the grid size, used in the numerical calculations was 0.064. It proved adequate, in that it allowed the formation of the instability, but the steep velocity gradients that develop indicate that accuracy would improve with a finer grid. Since the formation of surface instability represents a rather short–lived phase in the overall circulation simulation, and in order to keep the computation affordable, this inaccuracy was tolerated.

The development of the flow past marginal stability was previously investigated numerically also by Foster [1971]. His calculations of the wavelength of the intermittent convective cells (thermals) indicate that the horizontal grid size used here was adequate. Further, the average length scale (ℓ) of the thermals has been measured by Tamai and Asaeda [1984] who developed the empirical relation: $\ell/h = 64.2\ Ra^{-1/4}$ in the range $10^6 < Ra < 10^8$. At $Ra = 10^8$ $\ell/h = 0.64$ which also supports the adequacy of the resolution.

The surface thermal boundary layer (δ) can be estimated by the relation $\delta \sim k\Delta T/H$, where k is the thermal conductivity, ΔT is the temperature drop through this layer, and H is the surface heat flux. The relation between the temperature drop and the heat flux is implicit in the relation $Nu = 0.156\ Ra^{0.33}$ [Katsaros et al., 1977], where Nu is the Nusselt number defined as $Nu = Hh/k\Delta T$ and Ra_T the Rayleigh number based on $\Delta T (Ra_T = \beta g \Delta T h^3/\alpha\nu)$. By combining the above expressions, one finds $\delta/h = 4.029\ Ra^{-1/4}$. The vertical resolution (grid size) was made progressively finer towards the surface so as to include three points in the thermal boundary layer.

Since it is well known (and has been already observed for the $Ra = 10^6$ solution) that in the time–dependent regime the solutions are very sensitive to initial conditions and grid details [e.g. Thompson and Stewart, 1987], it is pointless to assess the accuracy of the solutions in terms of instantaneous fields; rather, the dependence of the solution on mesh size is made in terms of time–averaged quantities and the characteristics of fluctuations. Solutions of the flow at $Ra = 10^8$, Pr=7, S=0.2 were made for two different resolutions, namely 30x80 and 60x120, in the θ, r directions, respectively. On the coarser mesh, the solutions were started from isothermal and quiescent conditions. After the time–interval 741 to 2600 was found to be adequate for averaging according to the criterion discussed above, the instantaneous fields at t=741 were interpolated on the thinner mesh and a run of equal length was performed. It was found that the fine–grid solution satisfied the averaging criterion equally well. In terms of maxima, the two solutions differed by 8.3% in ψ_{max} and 6.1% in $u_{r_{max}}$, while the functional form of the ψ and u fields is very similar for the two

different grids. In terms of the standard deviation of the Q and $\bar{H}$ curves (Eq. III–26) reported in Fig. IV–14, the maximum difference between the two calculations was 7%.

E. INTERPRETATION OF THE Ra DEPENDENCE

Having described in the preceding sections the three flow regimes that correspond to three different Ra values, it is useful to summarize the results by examining the effects that the increase of Ra has on the flow. The dependence of $u_{r_{max}}$ and ψ_{max} on Ra is shown in Fig. IV–15a,b. From the description of the flow given in sections IV–2, 3, 4, it follows that, since the flow configuration (flow patterns) is different for each Ra value, it is not expected that a single scaling law will fit the v_r, ψ dependencies, so that Fig. IV–15 should be regarded as a mere summary of the results of the numerical experiments.

For a given fluid, e.g. water, an increase in Ra can be interpreted as being due to either an increase in surface heat loss rate H or an increase in maximum depth h_s (Eq. (III–12). Because of the importance this distinction has in applications, it is of interest to examine each case separately.

Effects of h_s *increase*

The effects that the increase of h_s has on the flow is of particular interest in examining the relevance of solutions of the model posed in section IV–1 to the analysis of cooling induced currents in a littoral–like domain, where the deep–end boundary is open rather than closed. This is because a domain corresponding to a smaller h_s (i.e. Ra) value can be considered as being imbedded into a domain of larger h_s (i.e. Ra) value. The flow of the overlapping part in the larger domain is regarded, then, as the open–ended equivalent of the flow of the small, closed–end domain. The relative size of domains corresponding to Ra = 10^4, 10^6, 10^8 is $1/10:1/\sqrt{10}:1$. The effects of the deep–end boundary are assessed by comparing the horizontal (radial) circulation flow rate curves in the two domains.

A dimensionless length r of a domain of corresponding Ra value Ra_1 can be rescaled to r' using the length scale of a domain of Ra_2 value by:

$$\frac{r'}{r} = \left(\frac{Ra_2}{Ra_1} \right)^{1/4} \qquad \text{(IV–9)}$$

Similarly, to rescale a dimensionless flow rate Q from Ra_1 to Q' of Ra_2 the formula to be used is:

$$\frac{Q}{Q'} = \left(\frac{Ra_2}{Ra_1} \right)^{1/2} \qquad \text{(IV–10)}$$

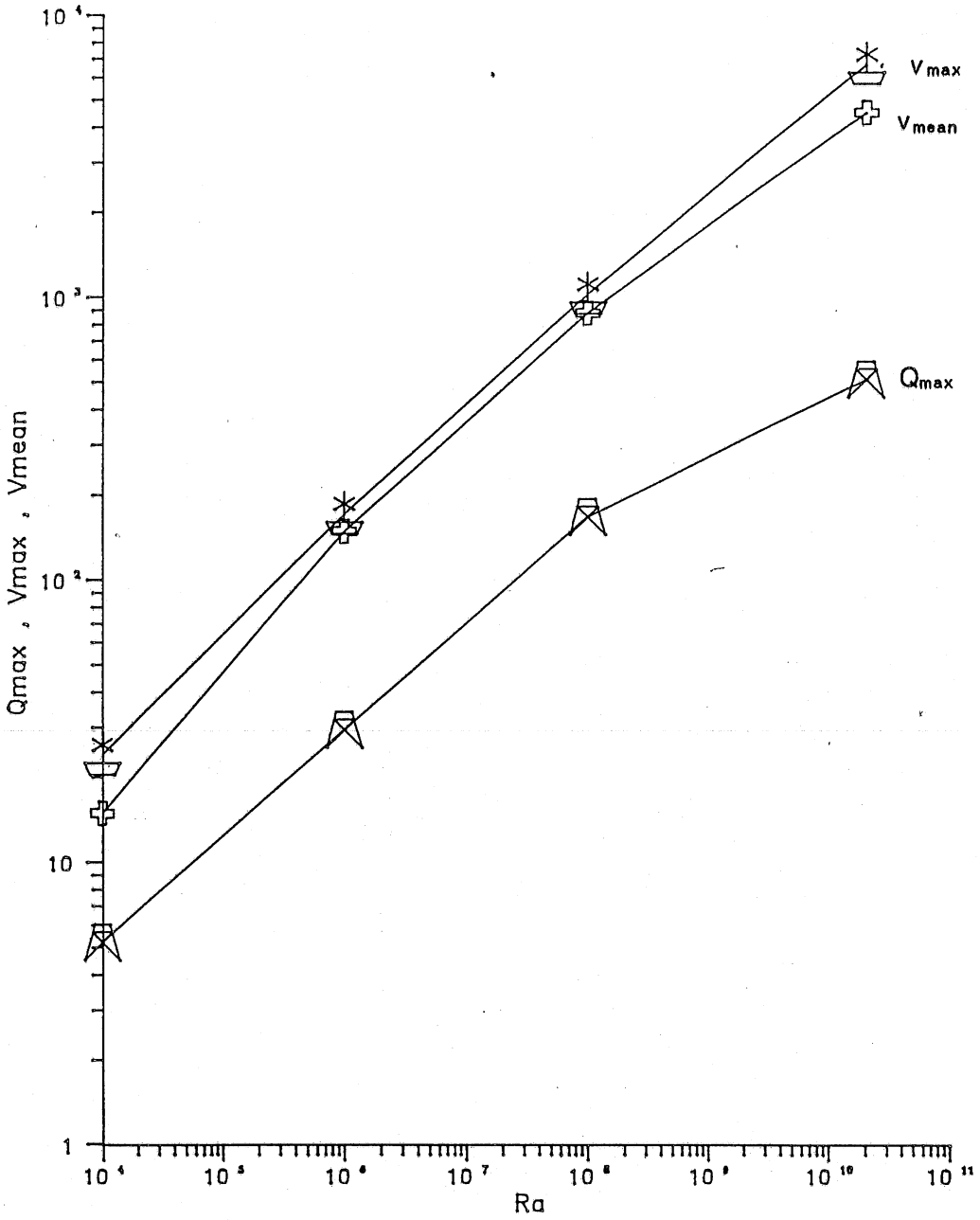

Fig. IV-15a The dependence of dimensionless v_{max}, Q_{max}, v_{mean} on Ra for Pr=7, S=0.2. The velocities have been normalized using a/h and the flowrate using a. The values corresponding to $Ra=2x10^{10}$ have been measured experimentally (Chapter V)

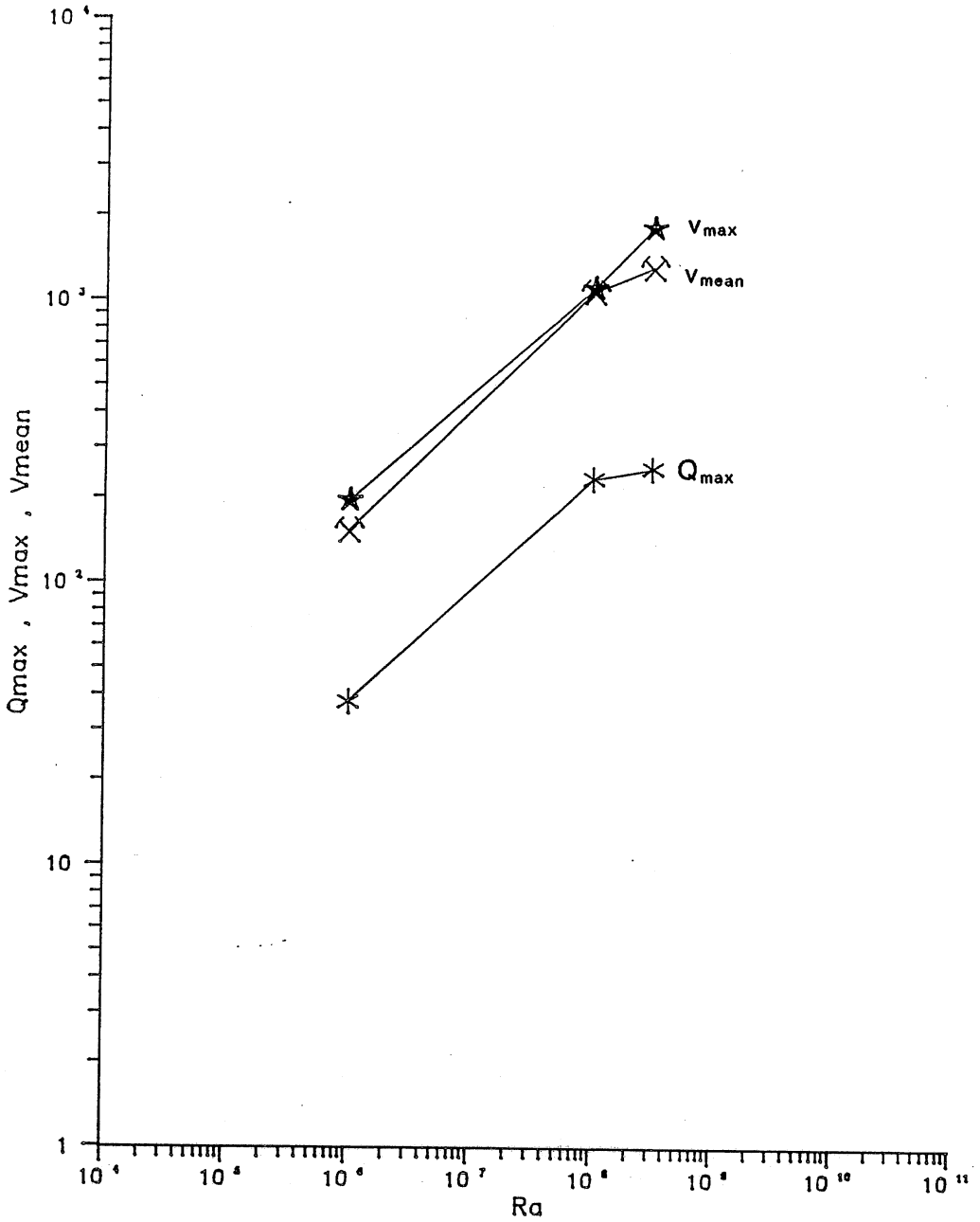

Fig. IV-15b The dependence of dimensionless v_{max}, Q_{max}, v_{mean} on Ra for Pr=7, S=0.1. The velocities have been normalized using a/h and the flowrate using a. The values corresponding to $Ra=3.1 \times 10^8$ have been measured experimentally (but for S=0.086, see Chapter V)

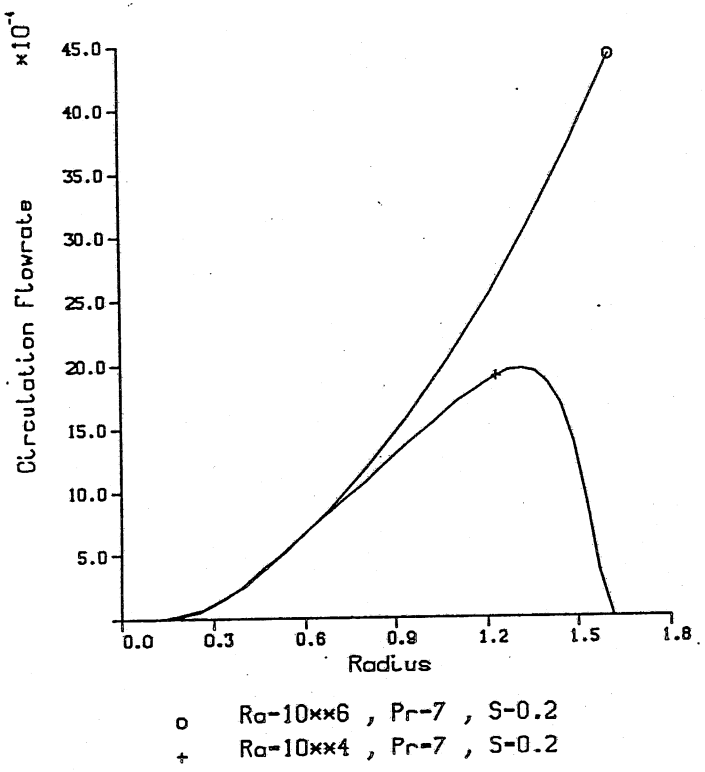

(a)

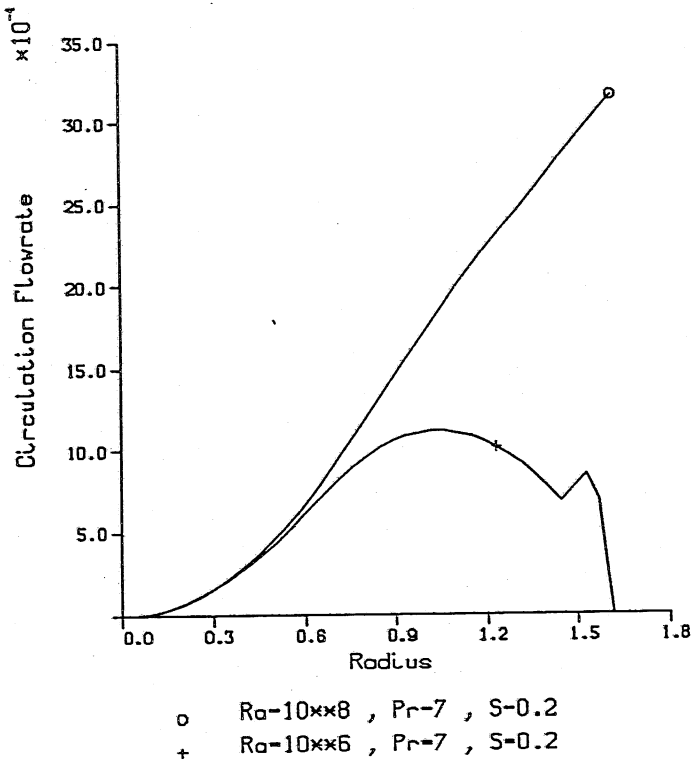

(b)

Fig. IV–16 Comparison between Q–curves for (a) $Ra=10^4$ and $Ra=10^6$ (b) $Ra=10^6$ and $Ra=10^8$ (time–averaged). In both cases the scales used correspond to the higher Ra.

The comparison between Ra = 10^4 and Ra = 10^6 Q–curves appears in Fig. IV–16a and for Ra = 10^6, 10^8 in Fig. IV–16b.

The most important outcome of the numerical solutions to be used in application is the flow rate that develops at the deep–end of the domain and establishes an exchange flow between the littoral and open waters. To extract the exchange flow rate from calculations or experiments in a closed–end domain, the linear portion of the Q–curves can be extrapolated up to the closed end. Figure IV–16 shows that such an extrapolation will tend to underestimate the exchange flow that would develop in a open–ended domain. Thus, use of solutions to the model formulated in Section III–1 in the analysis of cooling–induced exchange flow will produce low estimates.

Increase in H

Alternatively, an increase in Ra can be due to an increase in surface heat loss rate H while the fluid is specified and the maximum depth h_s is kept constant. In this case, the flow rates have to be rescaled according to Eq. IV–10, while the lengths remain unchanged. To observe the qualitative influence of the increase of H on the flow quantities, the flow fields for Ra = 10^4, 10^6, 10^8 have been juxtaposed in Fig. IV–17.

F. DEPENDENCE ON SLOPE

The effects that changes in slope have on the flow were investigated by comparing solutions at Ra = 10^6 and 10^8 with Pr=7 for S=0.1 and 0.2. In general, it was found that within this range of the parameters, changes in slope did not alter the distinctive characteristics in the evolution and the steady–state of the flow. For example the secondary cell in the deep–end of the domain at Ra=10^6 was present at the steady–state of both the S=0.1 and 0.2 solutions, and the same holds for the time–averaged fields at Ra=10^8.

Among the most interesting features of the model described in Section III–A and III–B is the behavior of the flow as the slope S decreases. It can be recalled from Section III–C that the steady, depth integrated heat transfer is given by:

$$\bar{H}_{st}(r) = H\, r\, \left(\frac{r}{R} - 1 \right) \qquad \text{(III–22)}$$

so that the average heat transfer is:

$$\frac{\bar{H}_{st}(r)}{r\,S} = H\left(\frac{r}{R} - 1 \right) S^{-1} \qquad \text{((IV–11)}$$

From Eq. IV–11 it follows that as S → 0 the average heat transfer increases as S^{-1}. In section III–D on pure conduction, it was shown that, as a result, as S → 0, the horizontal temperature scale increases as S^{-2} (Eq. III–27). In Appendix IV it is argued that in the case of a Newtonian fluid, there exists a flow region at the pointed–end of the domain where heat transfer is

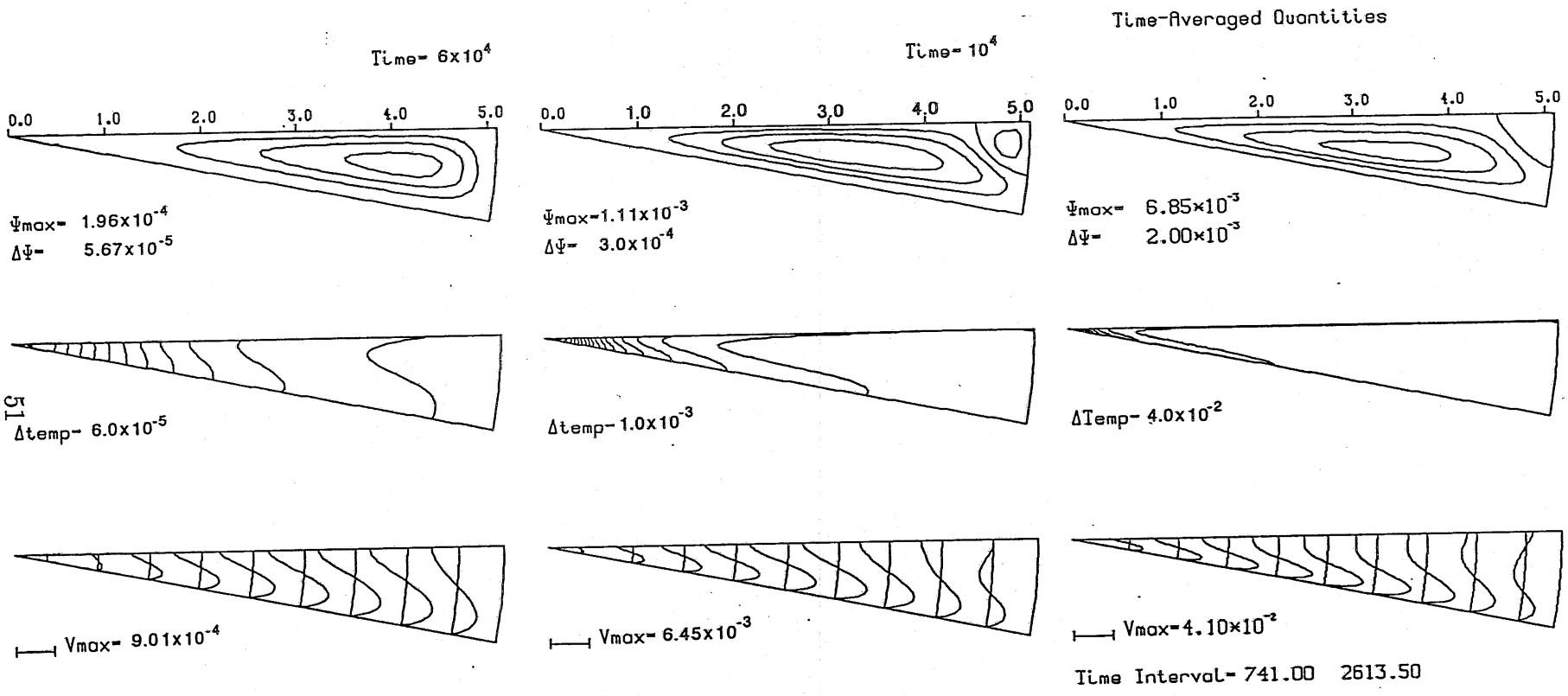

Fig. IV-17 Comparison of streamlines, isotherms and radial velocity profiles for Ra=10^4, 10^6, 10^8 (from left to right respectively). All quantities have been scaled with Ra=10^8 scales. (Pr=7, S=0.2 for all graphs).

dominated by conduction the length of which decreases as $S^{1/2}$ in the limit $S \to 0$. Thus, it can be expected that the strength of advection increases as the slope decreases, and the advective terms in the energy equation become dominant since, as the slope decreases, the radial amount of heat flow imposed by the boundary conditions is forced through a "shallower" depth.

The dependence of v_{max} and Q_{max} on S can be seen from the values included in Table IV–4.

Table IV–4

Ra	$V_{max}/\alpha/h$		Q_{max}/α	
	S = 0.1	S = 0.2	S = 0.1	S = 0.2
10^4	26.5*	23.8	5.89*	5.19
10^6	195	171	37.6	29.4
10^8	1110	1020	234	166

The values of V_{max}, Q_{max} for slopes S=0.1, 0.2. All values correspond to the Pr=7 calculation except those marked by * for which Pr = 1.

G. TIME TO STEADY STATE

The dimensionless time required to reach steady state is summarized in Table IV–5 as a function of Ra and S.

Table IV–5

Time to Steady–State
Normalized by the h^2/α Scale

Ra	S=0.1	S=0.2
10^4	5.0	2.0
10^6	0.5	0.2

From Figs. IV–1, IV–3, IV–5, and IV–7, it can be seen that the time–to–steady–state consists of the time required to reach the single cell configuration plus a diffusive adjustment necessary to reach the steady–state heat transfer. At Ra = 10^6, this diffusive adjustment is simultaneous with oscillations in the flow field caused by the adjustment of the secondary cell at the deep end.

At Ra = 10^8, where the solutions reach a steady state in a time–average sense only, the important time scales are the length of an adequate time–averaging interval and the initial development interval which should be excluded from the steady–state averaging.

As mentioned in Section IV–D.2, a suitable criterion for the adequacy of the length of time–averaging interval can be based on Eq. III–22; the time–averaged flow rate curves are shown in Fig. IV–13 for Ra = 10^8, Pr = 7, S = 0.2 and in Fig. IV–18 for Ra = 10^8, Pr = 7, S = 0.1.

As the time averaging interval is reduced, the averages deteriorate. To determine the time required for the initial development, averages were taken over intervals of fixed length but positioned at different instants within the calculated record. Using an interval of length $\Delta t = 125$, it was found that the qualities of the time–averaged radial flow rate and heat transfer curves change abruptly at $t \sim 400$, as is shown in Fig. IV–18.

H. VELOCITY PROFILE CHARACTERISTICS

As the Rayleigh number is increased, the flow configuration (regime) changes, as described above, so that the shape of the velocity profile also changes. The profile characteristics of greatest interest, since they enter the calculation of the flow rate curve, are the zero velocity point measured from the bottom and normalized by the local depth, the distance from the origin to the point where Q_{max} occurs, and the layer–mean velocity.

The normalized zero–velocity point is plotted as a function of Ra in Fig. IV–19, where experimental measurements are also included (see Chapter V). It is interesting to note that for Ra = 10^4, 10^6, i.e. before instability renders the solutions time–dependent, the zero–velocity point is located above mid–depth. The distance of the zero velocity point from the bottom becomes less than 0.5 times the depth for Ra = 10^8 and, including the experimental evidence, it continues to decrease as Ra increases. Harashima and Watanabe [1986] measured in their cooling–induced gravitational circulation experiments on a horizontal bottom, the zero velocity point to be at 0.4. They attributed the difference between their measurements and the similarity solution of Rattray and Hansen [1962] for stably stratified gravitational circulation, to the convective instability which developed in the surface layer of their experiments. Figure IV–19 seems to corroborate the validity of this claim.

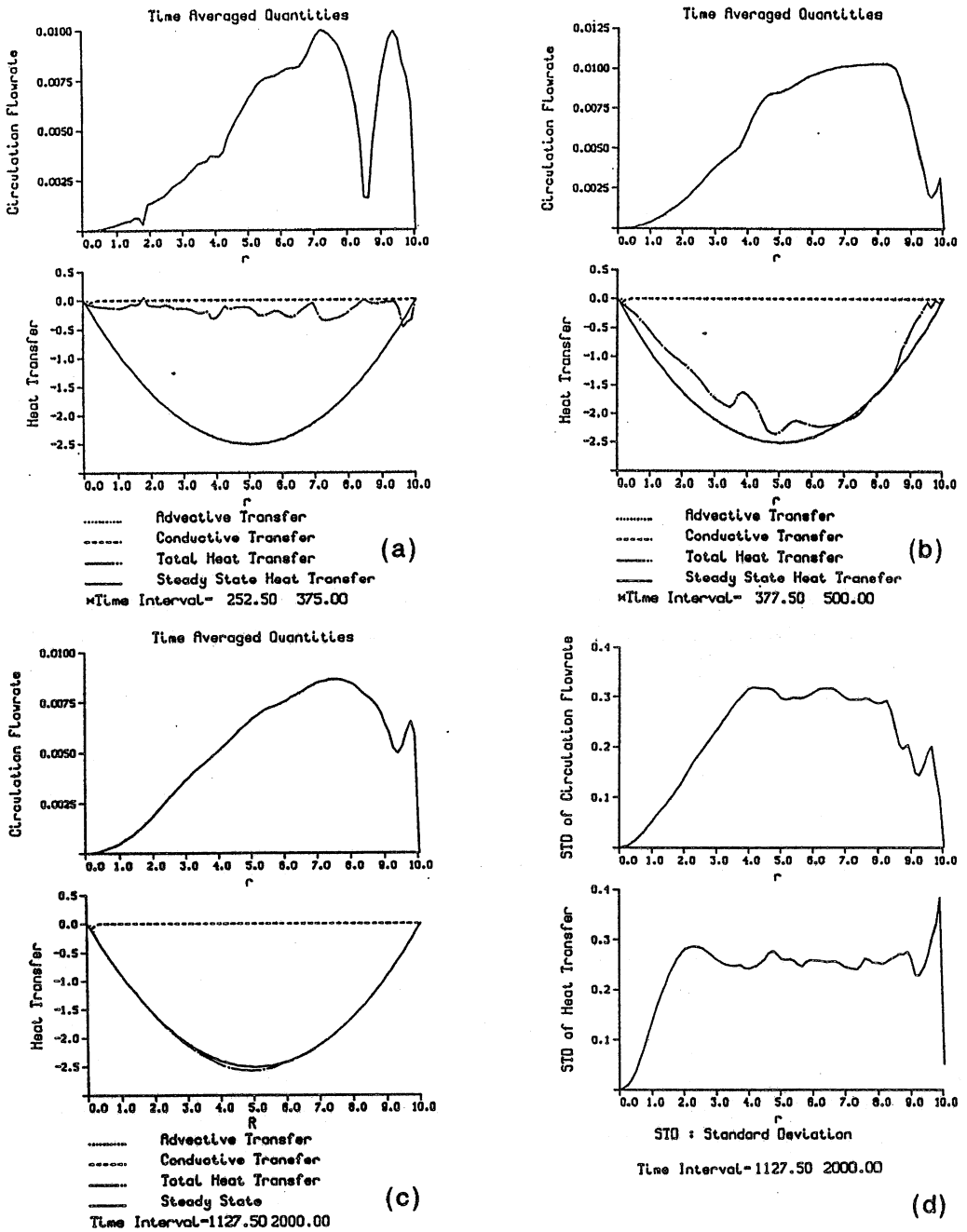

Fig. IV-18 Averages for the Ra=10^8,Pr=7, S=0.1 solution. Improvement of the quality of the time-averaged curves as averaging is moved from (a) within to (b) outside the initial development period. (c) Time-averaged radial flowrate and heat transfer curves over a long interval and (d) the corresponding standard deviations.

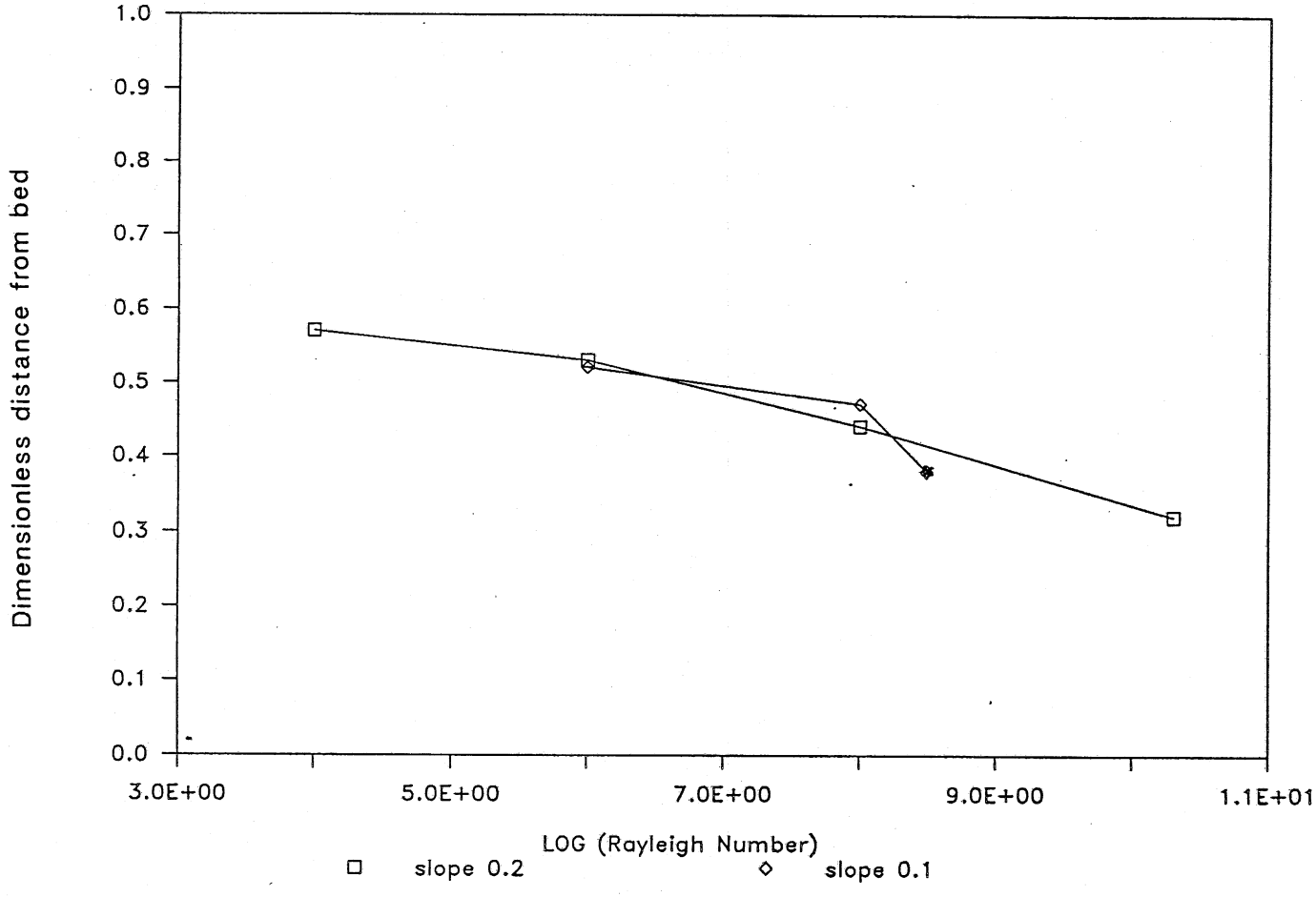

Fig. IV-19 Location of zero velocity point, measured from the bottom and normalized by the local depth, versus the Rayleigh number. The experimental point at 3.1×10^8 (*) corresponds actually to S=0.086.

The location where the highest underflow rate Q_{max} occurs is summarized in Table IV–6, as a function of Ra and S.

Table IV–6

Dimensionless Radial Distance of the Location of Q_{max} as a Function of Ra and S.

Ra	S=0.2	S=0.2	
10^4		4.2	numerical
10^6	7.4	3.2	numerical
10^8	7.6	3.7	numerical
3×10^8	8.8		experimental
2×10^{10}		2.3	experimental
S = 0.086			

This location is greatly influenced by the flow regime. For example, this point is displaced towards the center of the triangular flow domain when a secondary cell forms at the deep end for Ra = 10^6.

The constant mean–layer velocity was defined by approximating linearly the rising limb of the flow rate curve. Such a definition entails a degree of arbitrariness but is useful for applications and also because the mean velocity is directly related to the entrainment between the two layers. The mean velocity (u_{mean}) is plotted as a function of Ra in Figs. IV–15a,b.

V. APPLICATION TO VEGETATED LITTORAL SLOPES

It is often the case that numerical calculations and laboratory experiments of convective flows can only be performed for values of the independent parameters (e.g. Rayleigh number) that are much lower than values characteristic of natural systems. Recent examples are the experiments of Harashima and Watanabe [1986] on convective circulation in estuaries, the numerical calculation of Patterson [1987] on convective flows induced by radiative heating of lake–side arms, and the calculations of Foster [1971] on the diurnal evolution of cooling–induced convective cells in the ocean. To apply the results of these studies, recourse must be had to the use of eddy diffusivities, and in the aforementioned studies diffusivities equal to 1 cm^2/sec were assumed.

For the analysis of the flow studied herein on a scale representative of natural systems, simulations of Ra values in the range 10^{10} – 10^{14} are required, if Ra is based on the molecular properties of water as in Eq. III–12. The Ra = 10^8 calculation could describe the outcome of a laboratory experiment in a tank 10 cm deep subjected to H = 42 W/m^2 (if water properties are evaluated at 20° C). At present, extension of the simulations using the Navier–Stokes equations to Ra = 10^{10} to 10^{14} requires excessively large amounts of computational time, even if supercomputers are used.

Often the littoral regions of lakes are vegetated. Depending on light penetration, macrophyte populations may extend to depths of several meters. Even in eutrophic lakes rooted aquatic vegetation can often be found in water depths of up to 2 meters.

Such vegetation increases the resistance to flow appreciably. Some experimental measurements of drag on aquatic plants have been reported by Sear [1977]. If this resistance is translated into an apparent viscosity, the effective Raleigh numbers are reduced appreciably such that the range of numerical simulations or experiments is reduced and those results become applicable.

These situations are of special interest since the convective exchange flow is then a factor in the growth of the aquatic plants. The most satisfactory way to model this added resistance is by introducing a drag term in the momentum equations. This was done by Burke [1982], who extended the low Reynolds number turbulence κ–ϵ model to account for obstructed flow and applied the model to flow through tidally inundated marsh grass. In his study the vegetation was modeled as a collection of circular cylinders of constant diameter, i.e. the drag coefficient (c_D) of the term accounting for drag in the momentum equation, which corresponded to a single circular cylinder. Interference between cylinders was accounted for by adjusting vegetation density so as to improve the fit of the prediction to the data.

In practical terms, this method introduces an additional independent parameter to the problem, adding somewhat to the cost of computation. Herein, such computations have not been carried out. Instead it is proposed to assume that the drag–induced energy dissipation due to the presence of aquatic plants can be accounted for by an increased, spatially constant, apparent viscosity (ϵ). This assumption, as well as the arguments advanced to estimate the magnitude of the apparent viscosity are extremely crude and aim at merely assessing in a very simplified way the potential of the convective circulation in renewing the littoral waters.

To calculate the viscous dissipation in the flow, only the terms due to the laminar velocity profile are retained, neglecting the terms that arise when the flow becomes time–dependent at steady–state. The total dissipation ($\dot{E}$) within a vertical column (i.e., volume enclosed between 0 and θ_T, r_1 and r_2, and of width s) can be approximated by:

$$\dot{E} = \mu \, s \int_{r_1}^{r_2} \int_{0}^{\theta_T} \left[\frac{\partial v}{\partial \theta}\right] \frac{1}{r} \, d\theta \, dr \qquad (V\text{–}1)$$

To simplify the calculation of this integral it is assumed that: (i) the mean velocity V_{mean} is constant, or, equivalently, the flow rate increases linearly with r (see Fig. V–1); (ii) the velocity profiles are similar:

$$\frac{V(r,\theta)}{V_{max}} = f(\theta) \qquad (V\text{–}2)$$

Velocity profiles in the region where V_{mean} is nearly constant are superimposed in Fig. V–2(a), and they are averaged–out in Fig. V–2b to form $f(\theta)$. With these assumptions Eq. V–1 becomes:

$$\dot{E} = \mu \, v_{max}^2 \, \frac{s^2}{r} \int_{0}^{\theta_T} (f')^2 \, d\theta \qquad (V\text{–}3)$$

where it has been implicitly assumed that $r_2 - r_1 = s$, and s is small enough for $\ell n \, r_2/r_1 \simeq s/r$, if $r \sim r_1$.

Next, the dissipation caused by the presence of a cylindrical plant stem of diameter D is calculated. It is assumed that the stem extends up to the surface. The drag exerted on a cylindrical element is:

$$d(Drag) = \frac{1}{2} \, C_D \, \rho \, v \, |v| \, (D \, r \, d\theta) \qquad (V\text{–}4)$$

where C_D is the drag coefficient [e.g., Tritton, 1959] approximated in the range of Re_D=1 to 10 by:

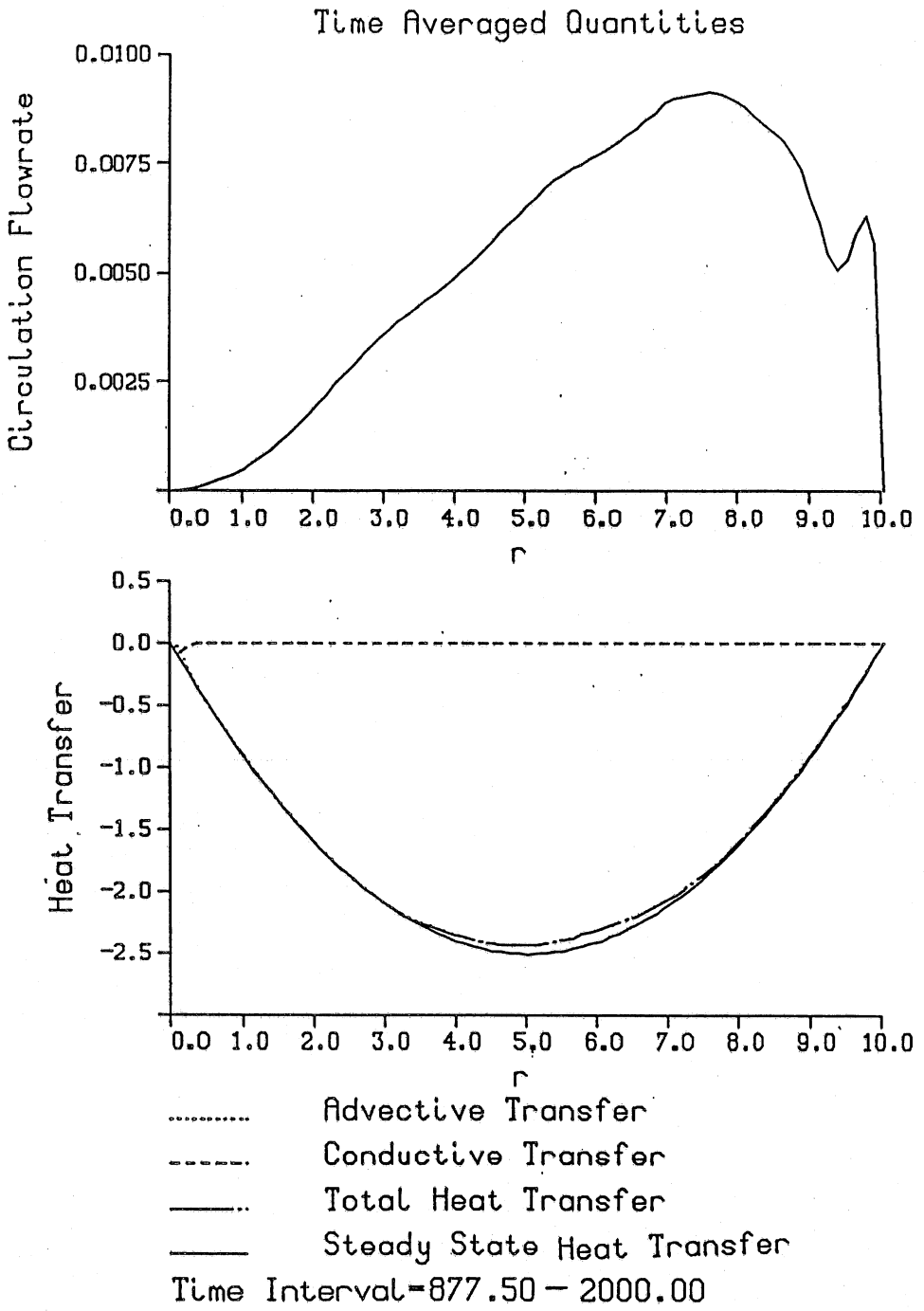

Fig. V-1 Time-averaged flowrate and horizontal heat transfer for $Ra=10^8$, $Pr=7$ $S=0.1$

$$C_D = \frac{C}{Re_D^{1/2}} = C \left[\frac{vD}{\nu}\right]^{-1/2} \qquad (V-5)$$

with $C = 10$.

The energy dissipation due to the drag (V–4) is given by:

$$d\dot{E} = \frac{1}{2} C_D \rho |v|^3 D r d\theta \qquad (V-6)$$

Integrating over the whole depth:

$$\dot{E} = \frac{C}{2} \rho r \sqrt{D\nu} v_{max}^{5/2} \int_0^{\theta_T} |f|^{5/2} d\theta \qquad (V-7)$$

As stated earlier, it is proposed to attribute the dissipation given by Eq. V–7 to an increased apparent viscosity $\rho\epsilon$, i.e. to replace μ by $\rho\epsilon$ in Eq. V–3. This procedure entirely neglects the alteration of the velocity profile (e.g., Fig. V–2) due to the presence of cylinders. The result is:

$$\frac{\epsilon}{\nu} = \underbrace{\left\{ \frac{C}{2} \frac{\int_0^{\theta_T} |f|^{5/2} d\theta}{\int_0^{\theta_T} |f'|^2 d\theta} \frac{v_{max}}{v_{mean}}^{1/2} \right\}}_{\text{shape factors}} \underbrace{\left[\frac{\bar{v}_{mean} h}{\alpha}\right]^{1/2} \left[\frac{\alpha}{\nu}\right]^{1/2}}_{\text{flow Re number}} \underbrace{\left[\frac{D}{h}\right]^{1/2} \left[\frac{r}{s}\right]^2}_{\text{plant characteristics}} \qquad (V-8)$$

Application

The shape factors in Eq. V–8 can be evaluated using the results of the $Ra = 10^8$, $S = 0.2$, $Pr = 7$ calculation:

$$\int_0^{\theta_T} |f|^{5/2} d\theta = 7.02 \times 10^{-2} , \quad \int_0^{\theta_T} (f')^2 d\theta = 61.5 ,$$

$v_{max}/v_{mean} = 1.17$ and $C = 10$. Unfortunately $Ra = 10^8$ is not high enough to get a realistic application. For this reason the results of an experiment described in Chapter VI in which $Ra = 2 \times 10^{10}$, $S = 0.2$ are used. From Table VI–1 $v_{mean} h/\alpha = 4480$ for $Ra = 2 \times 10^{10}$, $S = 0.2$, $Pr = 4.87$. Substituting into Eq. V–8

$$\frac{\epsilon}{\nu} = 0.188 \left[\frac{D}{s}\right]^{1/2} \frac{r^2}{h^{1/2} s^{3/2}} \qquad (V-9)$$

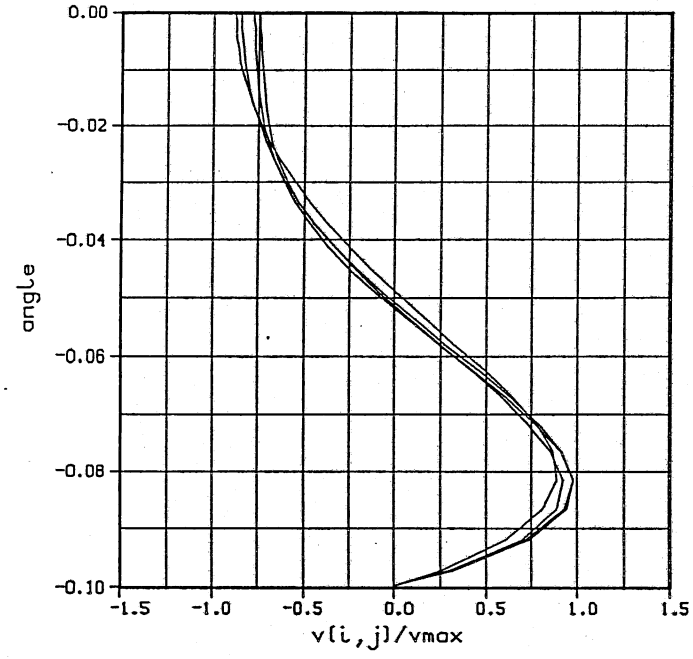

(a)

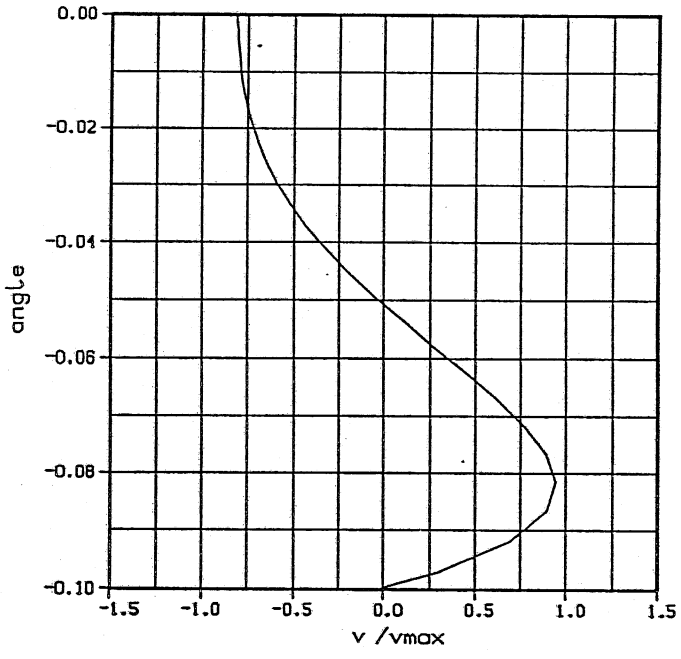

(b)

Fig. V-2 (a) Superposition of radial velocity profiles calculated at positions r(j) for $Ra=10^8$,S=0.1, Pr=7 . The velocity field has been time-averaged over interval t=877.5-2000. (b) The mean of the profiles shown in (a).

To illustrate the application of the foregoing results, consider a flow domain 5 m long and 1 m deep (S = 0.2) subjected to a heat loss H = 100 W/m^2, so that $Ra_\nu = 2.46\ 10^{12}$. To interpret this flow using $Ra_\epsilon = 2\times10^8$ (i.e. Ra based on ϵ rather than ν in Eq. III–8),

$$\frac{\epsilon}{\nu} = \frac{Ra_\nu}{Ra_\epsilon} = 123 \qquad \text{(V–10)}$$

Equation V–9 can then provide the plant spacing required for this value of ϵ/ν. Assuming D/s = 0.5 (the interference effects that would certainly arise could, in principle, be compensated for by adjusting the spacing as did Burke [1982]). Equation V–9 shows that the maximum spacing occurring at h = 1 m is s = 10 cm.

Since $v_{mean}h/\alpha = 4480$ it follows that $v_{mean} = 0.6$ mm/s; from Table VI–1, $q_{max} = 0.7$ cm^2/s; this region which is 2.5 m^3/m in volume will be renewed in 9 hours.

VI. LABORATORY VISUALIZATION EXPERIMENT

A. NATURAL CONVECTION EXPERIMENTS IN ENCLOSURES AND FLUMES

Cooling induced littoral currents were further examined by performing small–scale laboratory visualization experiments. The experiments should be viewed as complementing the numerical simulations because, while free from some of the undesirable idealizations underlying the numerical model, they are subject to small–scale effects (e.g. surface tension) as well as significant measuring difficulties.

The most valuable contribution of the experiments is the information they provide for conditions where the numerical simulation becomes impracticably expensive, i.e. for high Ra and low S values. Before proceeding to the discussion of the experimental facilities and the results, some of the experimental techniques used in similar natural convection studies and problems encountered are briefly highlighted.

1. Experiments Simulating Gravitational Circulation in Lake Sidearms and Estuaries

Sturm [1976] performed experiments of sidearm circulation in a horizontal flume, 67 ft in effective length. The convective currents were induced by heating rods immersed in one end of the flume. Velocity measurements were made by taking successive photographs of a time line created by potassium permanganate crystals. An earlier experimental procedure using hot water introduced at the surface of one end of the flume and withdrawn from the bottom was discarded because it was found to influence the velocity of the density current.

It is noteworthy that the vertical temperature profiles measured in this study indicate a non–uniform temperature in the upper layer. This seems curious in view of the fact that all the experiments of cooling–induced circulation [Brocard et al., 1977; Harashima and Watanabe, 1986; Katsaros, 1977] found a well mixed surface layer uniform in temperature. Jain [1982], who used these data to extract shape factors, found it necessary to modify these profiles.

Brocard et al. [1977] performed experiments of convective circulation in sidearms in a 35 ft flume connected to a rectangular basin. Circulation was generated by introducing heated water at the surface of the basin while withdrawing an equal amount near the bottom. The system was designed to minimize the impact of the added momentum of the forced inflow and withdrawal. Temperature measurements were made by stationary thermisters and a fast response moving probe. Some velocity measurements were made by successive pictures of dye crystal streaks.

The experiments of Harashima and Watanabe [1986] provide the most natural representation of sidearm currents. They were performed in a 4 m long flume (bay section) connected to a section deeper by 60 cm (outer ocean). The bottom of each of these sections was kept at a constant temperature. The surface water was cooled by air that circulated and was chilled in a wind tunnel situated above the experimental tank. With this arrangement, the thickness of the upper layer was internally determined rather than being imposed as in the experiments of Sturm [1976] and Brocard et al. [1977]. In this respect the experiments of Harashima and Watanabe [1986] resemble the experiments described below. Temperature measurements were made by traversing a copper–constant thermocouple. The air velocity was measured by a hot wire anemometer and water velocities were measured at the center of the channel with a laser–doppler velocimeter. The water velocities were averaged over 30 sec with a resolution of 0.1 cm/sec.

Imberger [1974] experimentally studied convective circulation in a shallow enclosure with differentially heated end walls as a model of gravitational circulation in well mixed estuaries. Velocity measurements were made using the thymol blue technique of Baker [1966]. The surface of the experimental tank had a solid lid because it was found that if the experiments were performed with a free surface, surface tension variations could significantly affect the convective velocities. At higher Ra numbers the same flow was studied by Bejan et al. [1981]. Velocities were calculated from photographs of potassium permanganate streaks.

2. Experiments of Flow Induced by Surface Cooling of a Horizontal Layer of Water

Katsaros et al. [1977] studied the structure of the thermal boundary layer that develops when a deep layer of water is cooled from the surface.

The bulk of the fluid under convection was found to be well–mixed; the relation between the temperature drop within the surface boundary layer $\Delta T = T_b - T_s$ (b full, s surface) was expressed as

$$Nu = 0.156\ Ra_{\Delta T}^{0.33} \qquad \text{(VI–1)}$$

where $Ra_{\Delta T}$ is as in IV–5 and Nu as in IV–6.

The flow was visualized using Kalliroscope crystals as tracers. To observe the motion in a vertical plane, the plane was illuminated by passing a laser beam through a cylindrical lens. This visualization technique was used in the experiments described below in order to get a global view of the flow.

Tamai and Asaeda [1984] studied the structure of the convective cells that develop in a layer of water heated from the bottom (or cooled by the surface). They visualized the flow using aluminum powder and laser illumination. Temperature measurements were performed by thermistors with 0.01°C sensitivity; this sensitivity was necessary to resolve the temperature variation along convection lines (i.e. lines that correspond to

sheet–like plumes). The dependence of the average length scale, ℓ, of the convection lines in a tank of depth d was expressed as:

$$\ell/d = 64.2\ Ra^{-1/4}\quad 10^6 < Ra < 10^8 \qquad \text{(VI–2)}$$

$$\ell/d = 14.0\ Ra^{-1/6}\quad 10^8 < Ra < 10^{11} \qquad \text{(VI–3)}$$

where Ra is as in III–12. This lengthscale (according to the precise definition they give) was not influenced by the width to depth (aspect) ratio of their tank, since in a tank of different aspect ratio essentially identical results were obtained. Thus, it seems noteworthy that Eq. VI–3, the higher Ra value formula, indicates that ℓ depends on the depth d, while Eq. VI–2, the lower Ra–value formula, shows ℓ to be independent of d.

Flow visualization by Tamai and Asaeda [1984] revealed that a sheet–like convective plume is composed by several successive thermals generated by the collapse of the conduction layer. They also measured additional features of the thermals including their frequency and duration. In a subsequent paper Tamai and Asaeda [1987] calculated the horizontal velocity mean distribution and fluctuating properties of the conduction lines.

In experiments of the interaction of natural convection plumes with mean flow in an enclosure heated from below and cooled above, Rhee et al. [1984] introduced a very effective visualization technique using temperature sensitive liquid crystals which simultaneously illustrate the flow structure and the temperature field. The color of the liquid crystals when illuminated with a white light changes continuously from red to blue over a prescribed fixed range of temperature. This technique could not be used in the experiments reported below where the temperature, instead of lying in a fixed range, continually decreased.

3. Experiments in Triangular Enclosures

The literature of experiments on natural convection in triangular enclosures is rather brief. Heat transfer data of natural convection in a triangular enclosure were published by Flack et al. [1979]. The temperature field and the local and overall heat transfer rates were obtained using a Schlieren interferometer. No observations of the flow were reported. Flack [1980] reports a few visual observations for a similar setting, where Bénard cells were observed until the flow turned turbulent.

Poulikakos and Bejan [1983] performed natural convection experiments in a triangular enclosure simulating night–time cooling of an attic space (see also section VI–C4). The Rayleigh number (Eq. IV–5) was in the range 10^6 – 10^9 where the flow was found to be turbulent. Temperature measurements were made by Chromel–Alumel thermocouples, while visualization was based on the thymol blue technique [Baker, 1966]. The temperature measurements revealed the existence of thermal boundary layers on both the upper and lower walls, while the core was isothermal. The temperature fluctuations were smaller in the core, indicating that the turbulence decreases away from the walls. The turbulence was attributed to boundary layer instability; no mention was made of the relevance of convective instability.

The experimental study described below was designed to closely represent the natural convection problem described in Section III–1. The goal was to obtain laboratory verification of the development of cooling–induced currents on a slope and provide a set of experimental observations to help evaluate the idealizations underlying the formulation of the numerical model. To this end, after describing the experimental facilities and techniques (Section IV–B), experimental observations pertaining to the two–dimensionality (Section IV–C1), the initial development (Section IV–C2) and the quasi–steady characteristics (Section IV–C3) of the flow are reported. Finally experimental and numerical results are combined to obtain a picture of the flow over a wider range of the independent parameters.

B. EXPERIMENTAL FACILITY AND TECHNIQUES

1. Experimental Tank

An experimental tank was designed and instrumented to physically model and measure the flow described above (Fig. VI–1,2). The tank was constructed of 1.3 cm thick clear plexiglas. The four sides and bottom were insulated with 5.1 cm thick polystyrene insulation which has a thermal resistance coefficient (R value) of 1.7°C m^2 W^{-1}. Along the length of the bottom of one side ran a 5.2 cm high multi–pane window (Figs. VI–1 and VI–3). This window was used for flow visualization and photographic velocity measurement. The tank could be tilted to any desired slope.

2. Instrumentation

Ideally, one would like measurements of velocity and temperature everywhere in the flow domain. This goal was unattainable both because of cost constraints and the intrusiveness of most measuring devices in what is inherently a delicate flow. Measurement was thus limited to non–intrusive techniques except in the deep end of the tank where temperature measurements were made of the interior of the flow and intrusiveness was less of a concern due to the nature of the flow in that region. Non–intrusive temperature measurement consisted of flush mounted thermistors (for bottom temperatures) and infrared thermography (for surface temperatures). A photographic technique of dye time–lines was used for velocity measurements.

Temperature measurements

The tank was equipped with a total of 16 thermistors; 10 thermistors were flush mounted in the bottom, three were mounted in the deep end wall and extended 5.5 cm into the interior of the box, and the remaining two were used outside of the tank to measure air and equilibrium temperatures (Fig. VI–4). Equilibrium temperature was established by measuring the internal temperature of a small (19 cm long, 14 cm wide, 7 cm deep) container of water insulated on all sides except the surface, set up adjacent to the experimental tank and allowed to come to thermal equilibrium with the room conditions for a number of days.

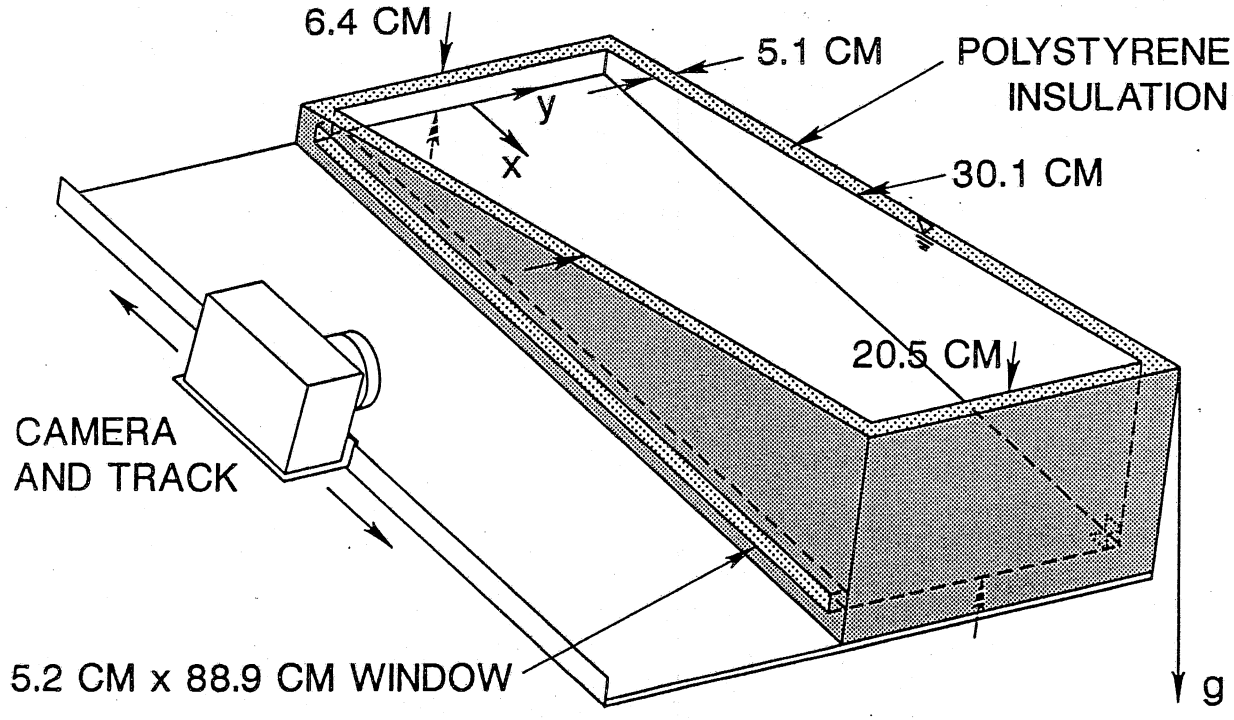

Fig. VI–1 Schematic of the experimental setup.

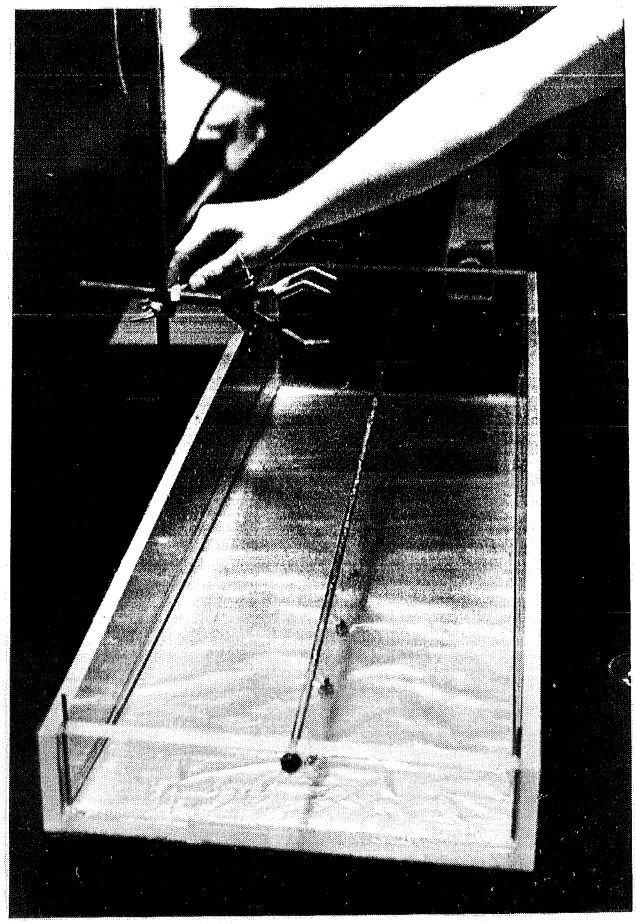

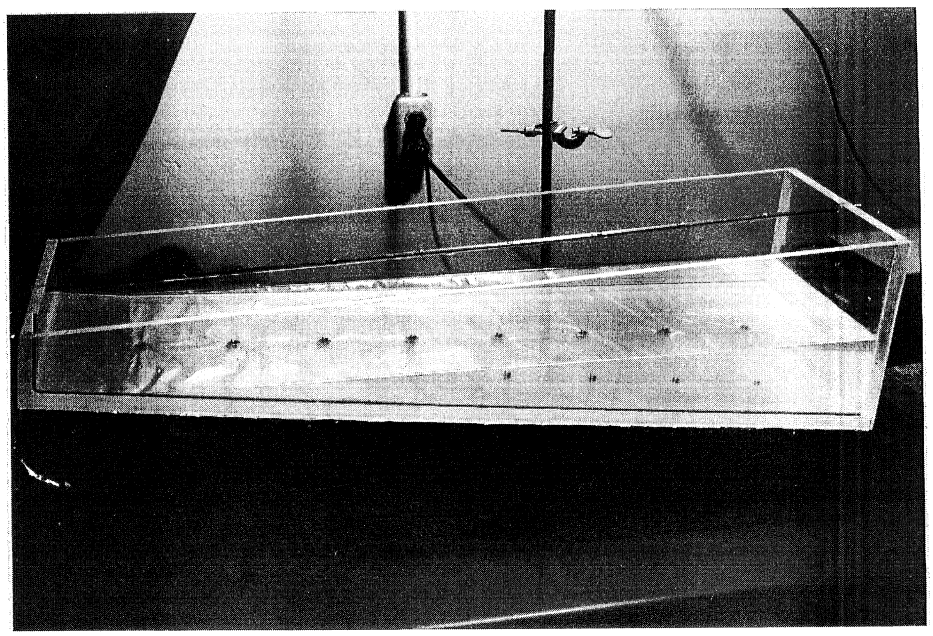

Fig. VI–2 The experimental tank without insulation.

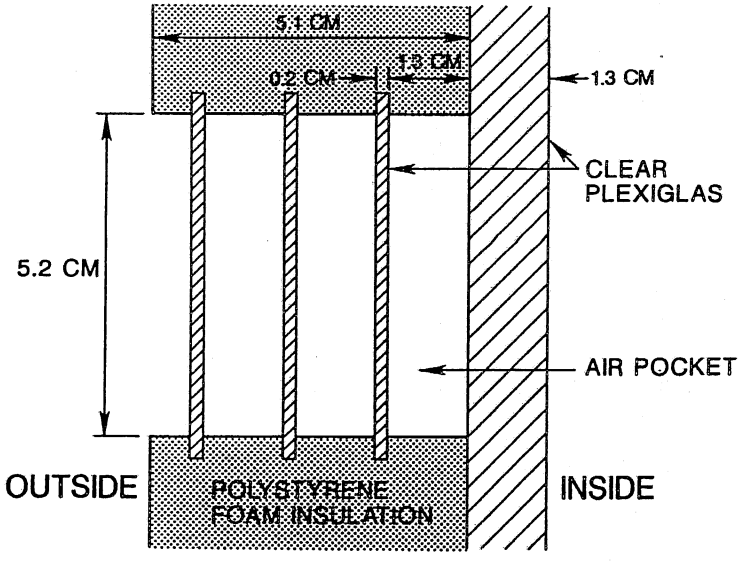

Fig. VI-3 Cross section of the observation window in the insulation of the experimental tank.

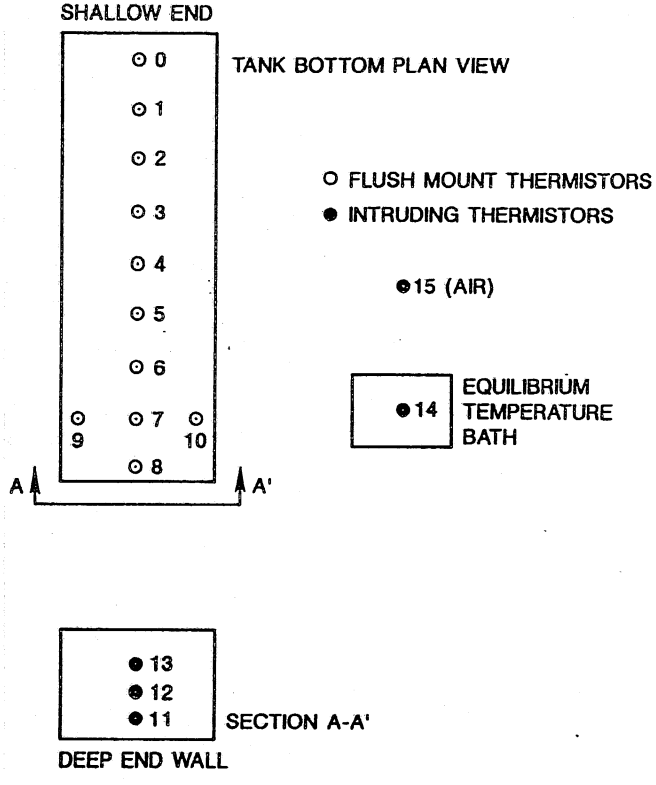

Fig. VI-4 Thermistor placement in experimental tank

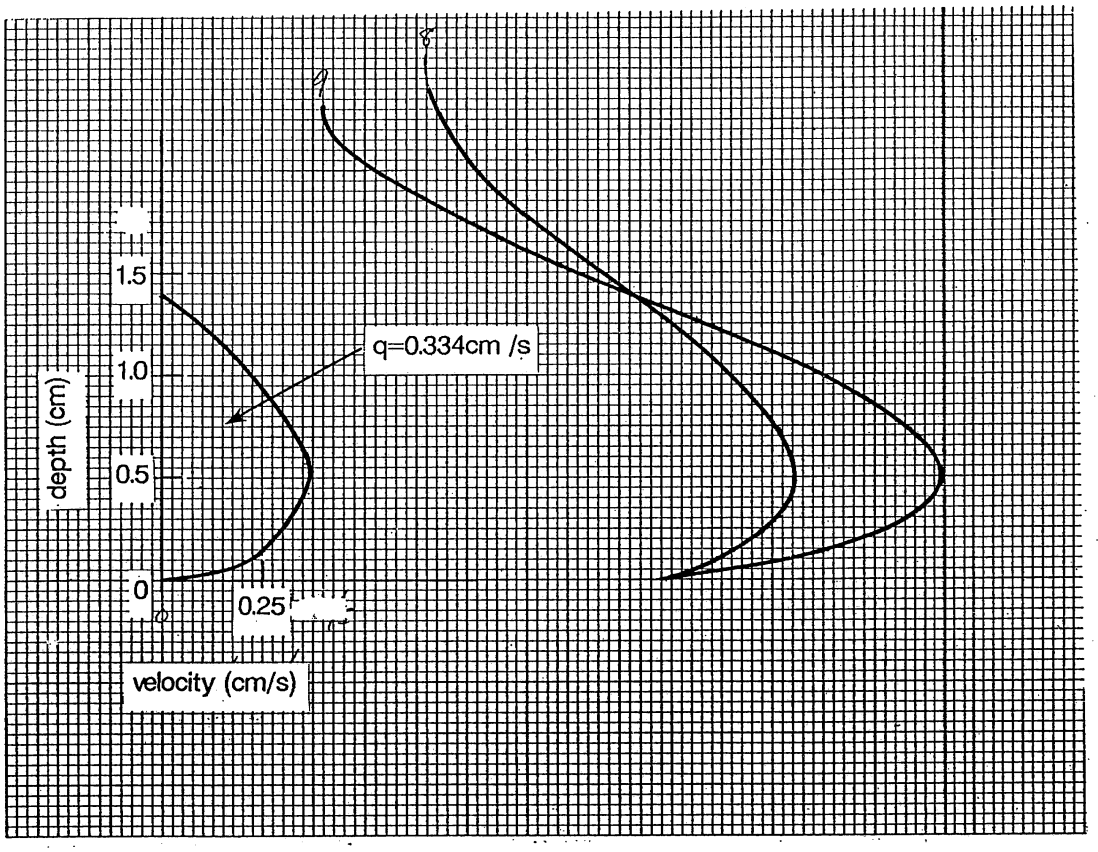

Fig. VI–6 Typical dye streak series and resulting velocity profile.

To begin an experiment (time = 0) the insulated lid was removed from the tank. To analyze the experimental data, the surface thermal boundary condition has to be clarified. The tank is cooling and evaporating in laboratory conditions as a result of temperature and humidity differences. Katsaros et al. [1977] noted that since under such conditions "any fluctuations in the surface temperature result in a larger fractional change ΔT (the temperature drop within the thermal boundary layer) than in H (heat flux), the boundary conditions of constant heat flux applies more closely."

Since the bulk temperature of the tank, however, is continually decreasing, the surface heat flux will be varying with time. If the water surface temperature lies within a narrow range, the complete surface heat balance can be simplified to a linear function of the average surface temperature $T_{b,s}$ [Edinger et al., 1968]

$$H = K(T_e - T_{b,s}) \qquad \text{(VI–4)}$$

where H = surface heat flux per area, T_e = equilibrium temperature and K = bulk thermal exchange coefficient. Assuming that K and T_e do not vary with time, the temperature of a well mixed water body subject to a surface flux given by Eq. VI–4 would be given by:

$$T_b - T_e = \exp\left(-\frac{K}{\rho c \bar{h}}\, t\right) \qquad \text{(VI–5)}$$

Strictly speaking, the boundary condition (VI–4) precludes the establishment of a quasi–steady state in the sense described in Section III–2, not because Eq. VI–5 introduces time dependent behavior in the momentum equation, but because it produces a time dependent (decreasing) source in the energy equation. For short periods of time, however, the surface heat flux, and thus the temperature gradients, can be considered quasi–constant (a maximum decrease of 25% per hour in H was determined) so that the experimental results can be characterized by a Rayleigh number based on constant surface heat flux (Eq. III–12). This is so in view of the fact that the "mean" quantities u_{max}, Q_{max} etc. have been found from the simulation to depend on a power of Ra between 1/2 and 1/3. In the experiments, T_e was measured as described in Section VI–B.2; K was determined by regression based on Eq. VI–5,

$$\ell n(T_{b,s} - T_e) = -\frac{Kt}{\rho c \bar{h}} \qquad \text{(VI–6)}$$

The closeness of the fit, Fig. VI–7, is a measure of the adequacy of formulation represented by Eq. VI–4. During the experiments, T_E actually varied at a maximum rate of 0.5° C per hour.

A comparison was attempted of H values from Eq. VI–4 with values determined by recasting Eq. VI–1 as:

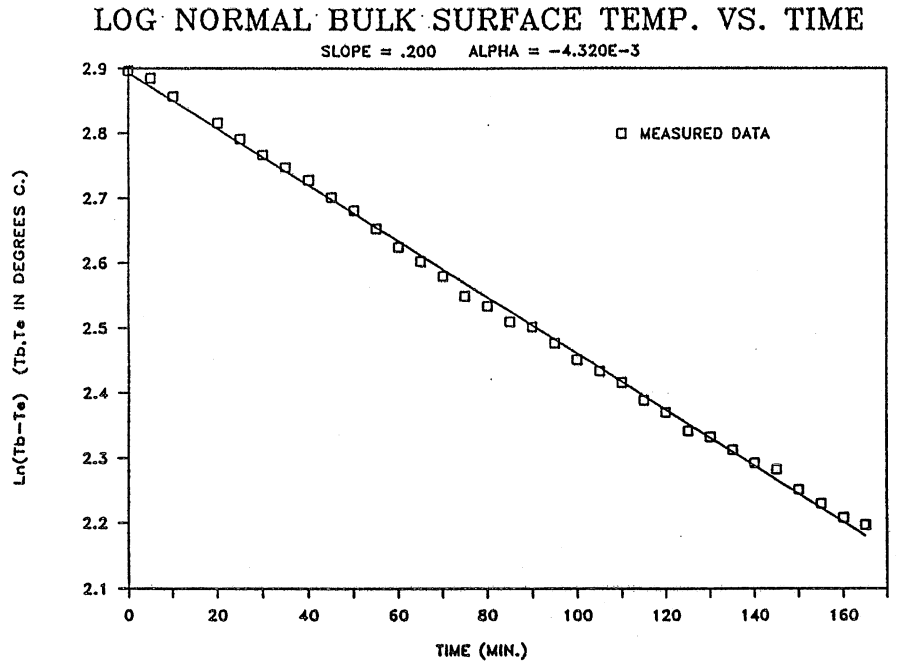

(a)

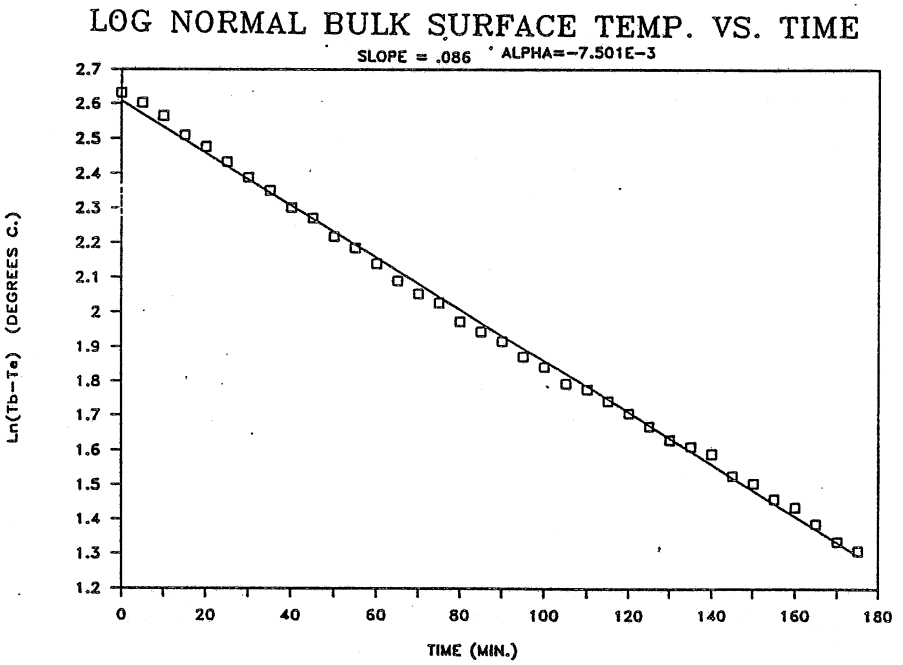

(b)

Fig. VI-7 Regression of experimental measurements to determine the parameter K of Eq. VI-4 for (a) S=0.2 and (b) S=0.086

$$H = 0.156\ k\ \left(\frac{g\beta}{\alpha\nu}\right)^{1/3} (T_{b,s} - T_b)^{4/3} \qquad \text{(VI–7)}$$

where $T_{s,b}$ = average surface T, T_b = bulk T and the rest of the symbols as in Section III–1. Unlike Eq. VI–4 in which $T_e - T_{b,s}$ is of the order of 15° C, Eq. IV–7 depends on $T_{b,s}$ which is typically slightly over one degree C. Using typical values of the parameters, it can be shown that a 0.3° C error would produce less than 2 percent error in H using Eq. VI–4 and about 30% using Eq. VI–7. Further, the existence of horizontal flow renders Eq. VI–4 not applicable here, in a strict sense.

The procedure used to estimate the heat loss from the side walls and bottom is described in Appendix III; it was found to be always less than 4% of the surface heat loss.

The initial development of flow was documented by taking temperatures everywhere and velocity profiles at one location every minute. After 20 minutes of this procedure, temperatures were measured every 5 minutes and velocity profiles were measured along the length of the tank centerline at various times for the duration of the experiment (approximately 3 hours).

The use of the velocity data was limited by the fact that the undercurrent demonstrated a degree of unsteadiness (primarily due to the influence of the thermals above it) while velocity profiles were measured on an instantaneous (not time averaged) basis. Approximately 100 profiles per experiment were taken. Where possible, two or three profiles were measured over a short time interval and averaged. Two–dimensional flow rates, maximum velocities, and layer thicknesses were computed from this information and longitudinal profiles of these quantities were plotted for different times during an experiment and were also averaged over each experiment as a whole.

Flow Visualization

The local velocity measurements were complemented with an overall visualization of the flow.

The flow was visualized by two methods: by rheoscopic crystals (rheoscopic concentrate, Kalliroscope Corporation, Groton, MA) and by creating colored streaks using the thymol blue technique of Baker [1966]. Eight tungsten wires were stretched vertically along the center plane of the tank 10 cm apart and attached to a metallic rod which provided the cathode required for the thymol blue technique, while two metallic rods fixed to the bottom of the tank served as anode.

A description of flow features observed by each method follows.

Rheoscopic crystals observations

To visually isolate the motion in a vertical plane along the slope, a two–dimensional light sheet was created by directing a laser beam through a cylindrical glass rod. This plane was not at the center of the tank but rather closer to the sidewall to provide more light for photography. This

technique (rheoscopic crystals–laser illumination) is similar to that used by Katsaros [1978].

Within a few minutes after the initiation of cooling, thermals were observed to be active. In the shallow part, the thermals were deflected by the slope. Their sense of rotation was apparently random, so that at times they seemed to be moving upslope. This feature was observed during the entire course of the experiment. Compared to the thermals forming in the deep part, those that formed in the shallow were less active, and it can be inferred that they were restricted by depth. A picture of the thermals is given in Fig. VI–8a.

After some time, a cold undercurrent was observed emanating from the shallow part and flowing along the whole span of the slope. This current can be seen in Fig. VI–8. Thermals which continue to dominate the upper layer, interact with the undercurrent; as a result the current exhibits recurrent bursts as, at some locations, thermals tend to compress it, while at other locations they provide uplift. In addition to the activity of thermals in the upper layer, a transitory drift of this layer was perceptible from the deep part towards the shallow. Since the rheoscopic crystals are dispersed uniformly in the fluid, observations from the side tend to average events occurring transversely to the slope, in spite of the fact that only a single vertical plane is illuminated. The local behavior is clarified by the thymol blue observations. The combined effect of the shorewise drift and deflection by the sloping bottom current causes the thermals to appear slanted, as can be seen in Fig. VI–8b.

Thymol Blue observations

The first vertical wire was only a few centimeters from the edge of the water. Blue streaks created at this wire showed that the two–layer system (undercurrent–upper layer return flow) extends nearly to the shallow edge of the water. However, at this very shallow part (i.e. at a place where Ra based on local depth is low), the surface layer exhibits less activity of thermals.

Another set of thymol blue observations involved the transverse appearance of the flow. For these observations a wire was stretched parallel to the bottom and orthogonal to the direction of the slope. The transverse blue streaks thus created soon acquired an undular appearance which was attributed to the activity of thermals. The behavior of these streaks did not seem to be different near the side walls.

Since the thymol blue streaks were very difficult to photograph, this technique was abandoned in favor of the dye streak technique described above for use in velocity measurements.

The values of the parameters and the results of the experiments are summarized in Table VI–1.

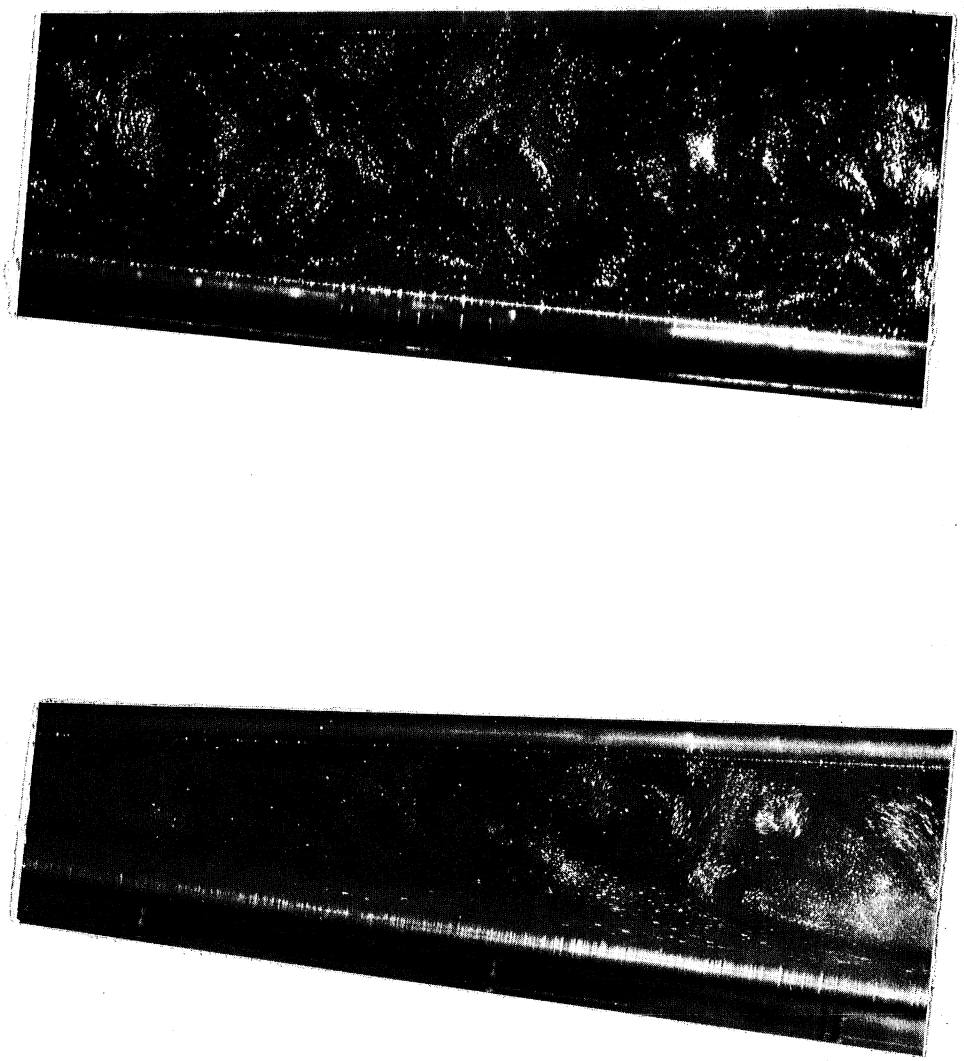

Fig. VI–8. Flow visualization using rheoscopic crystals showing (a) the initial development of thermals (b) the developed undercurrent with the upper layer convecting.

TABLE VI-1. Synopsis of Experimental Parameters and Results

	Slope	h_{max} cm	Time Interval min	T Bulk °C	α m^2/s	Pr —	H W/m^2	Ra —	V_{max} cm/s	q cm^2/s	$\bar{V}$ cm/s	$V_{max}/\frac{\alpha}{h}$	q/α	$\bar{v}/\frac{\alpha}{h}$	z_o/b
Onset	0.086	7.61	0–21	37–35	$1.50\ 10^{-7}$	4.66	385–325	$7.0\ 10^8$–$5.4\ 10^8$	0.38	0.301		1930	201		
Quasi–Steady	0.086	7.42	0–175				268–71	$3.9\ 10^8$–$6.6\ 10^7$							
	↓	↓	4–36	33–31	$1.47\ 10^{-7}$	5.24		$3.1\ 10^8$	0.36	0.374	0.262	1820	254	1320	0.38
	↓	↓	97–129	27–25	$1.44\ 10^{-7}$	6.07		$1.1\ 10^8$	0.17	0.225		876	156		
Onset	0.20	17.42	0–16	37.5	$1.5\ 10^7$	4.61	449–243	$2.2\ 1^{10}$	0.83	0.913		9640	609		
Quasi–Steady	↓	↓	16–165					$2.3\ 10^{10}$–$9.5\ 10^9$							
	↓	↓	29–40	35.5	$1.49\ 10^{-7}$	4.87		$2.0\ 10^{10}$	0.57	0.575	0.383	6660	508	4480	0.32
	↓	↓	78–92	33	$1.48\ 10^{-7}$	5.12		$1.5\ 10^{10}$	0.51	0.775		6000	524		
	↓	↓	153–162	30.5	$1.46\ 10^{-7}$	5.49		$9.7\ 10^9$	0.37	0.748		4410	512		

C. EXPERIMENTAL RESULTS

1. Two–Dimensionality

The development of flow structures that are not two–dimensional may be important in modeling the flow. Instrumentation able to detect three–dimensional flow characteristics was limited, consisting of two flush mounted thermistors symmetrically positioned near the tank sidewalls (Fig. VI–4, probes 9 and 10) and the infrared thermographs. Since the temperature gradients that drive the flow are small, it is difficult to document flow structures from temperature measurements alone. The existence of three–dimensional effects is apparent in the instantaneous transverse surface temperature profiles in Fig. VI–9; these effects become much more pronounced as the depth increases. A transverse profile near the shallow end at different times is shown for two different slopes in Fig. VI–10. It is noteworthy that averaged over the duration of the experiment, the 3–d effects are very weak for S = 0.20 but not for S = 0.086. Three–dimensional effects are also evident from the bottom temperature series (Fig. VI–11). For S = 0.086, no systematic difference can be detected between the output of the two thermistors symmetrically placed with respect to the centerline. In contrast, for S = 0.2, a systematic deviation of probes 9 and 10 of the order of –0.1 to –0.2° C from the centerline can be seen. This seems in congruence with (subjective) visual observations that the undercurrent seemed slightly more vigorous on that side of the tank. Finally the appearance of unexpected structures can be seen in the time series of bottom temperatures (Fig. VI–14).

2. Initial Flow Development

The flow onset was explored by taking velocity measurement series as quickly as the photographic technique allowed. For this purpose the measurements had to be confined to one location, x=35 cm, and the velocity profiles were measured every minute for up to 16 minutes. Any reliable criterion of the initial flow development would involve considerations of the characteristics of the velocity profile fluctuations which are impossible to capture with the dye–streak photographic technique. The velocity profiles at any fixed location were characterized by the flow rate of the undercurrent (Q) (integral of the profile), the maximum velocity within the undercurrent (v_{max}) and the zero velocity point (z_o). The flow onset measurements aimed at establishing how fast the velocity profile characteristics at x=35 cm rose to the range of their quasi steady values.

According to Tamai and Asaeda [1984] the average duration of a thermal D_t is given (using the present notation) by

$$D_t = 9.9 \left(\frac{g\beta H}{\rho c \nu} \right)^{-1/2} \qquad \text{(VI–8)}$$

For the heat fluxes determined at the onset of the flow for both S = 0.086 and S = 0.2 (Table VI–1), Eq. VI–8 gives average duration of thermals in the 10–20 sec. range. Thus, the influence of thermals on velocity profiles taken over a 16 min period should average out. For S = 0.086 the plots of

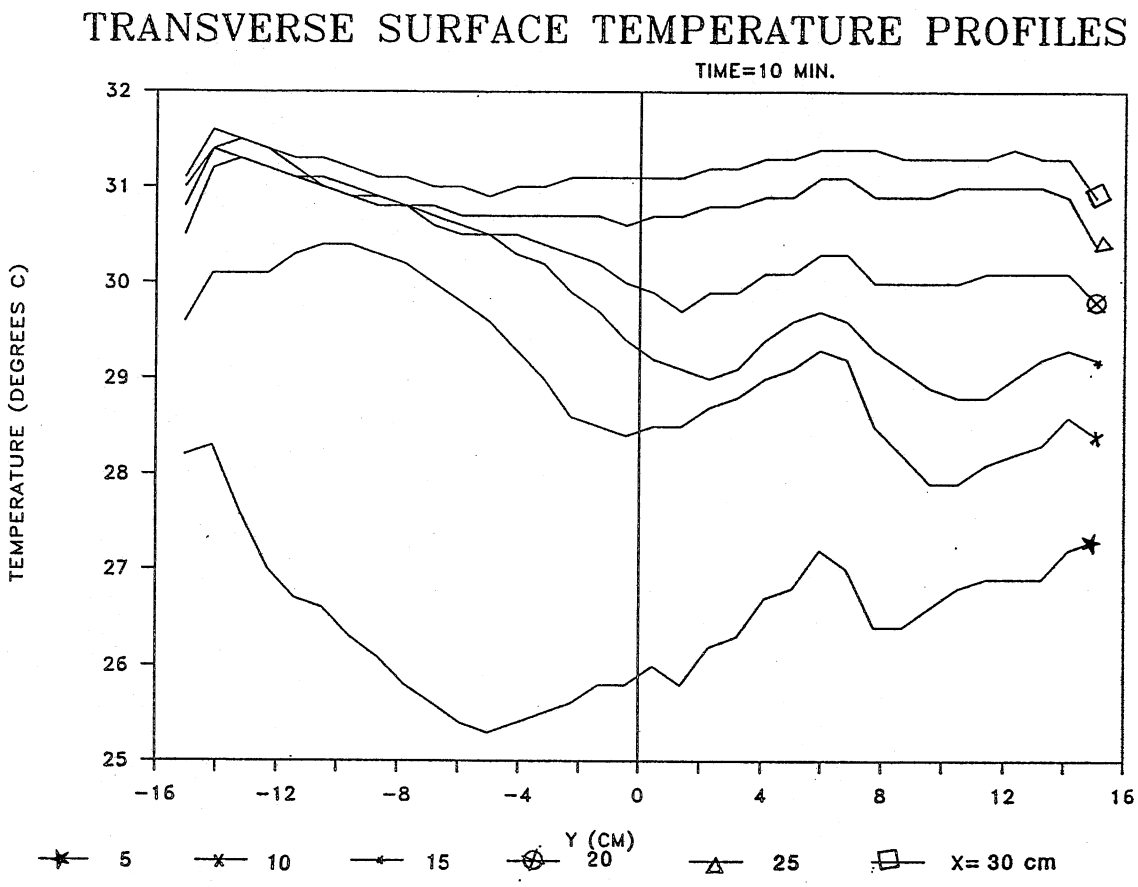

Fig. VI–9 Transverse surface temperature profiles at selected locations at t=10 min for the S=0.086 experiment.

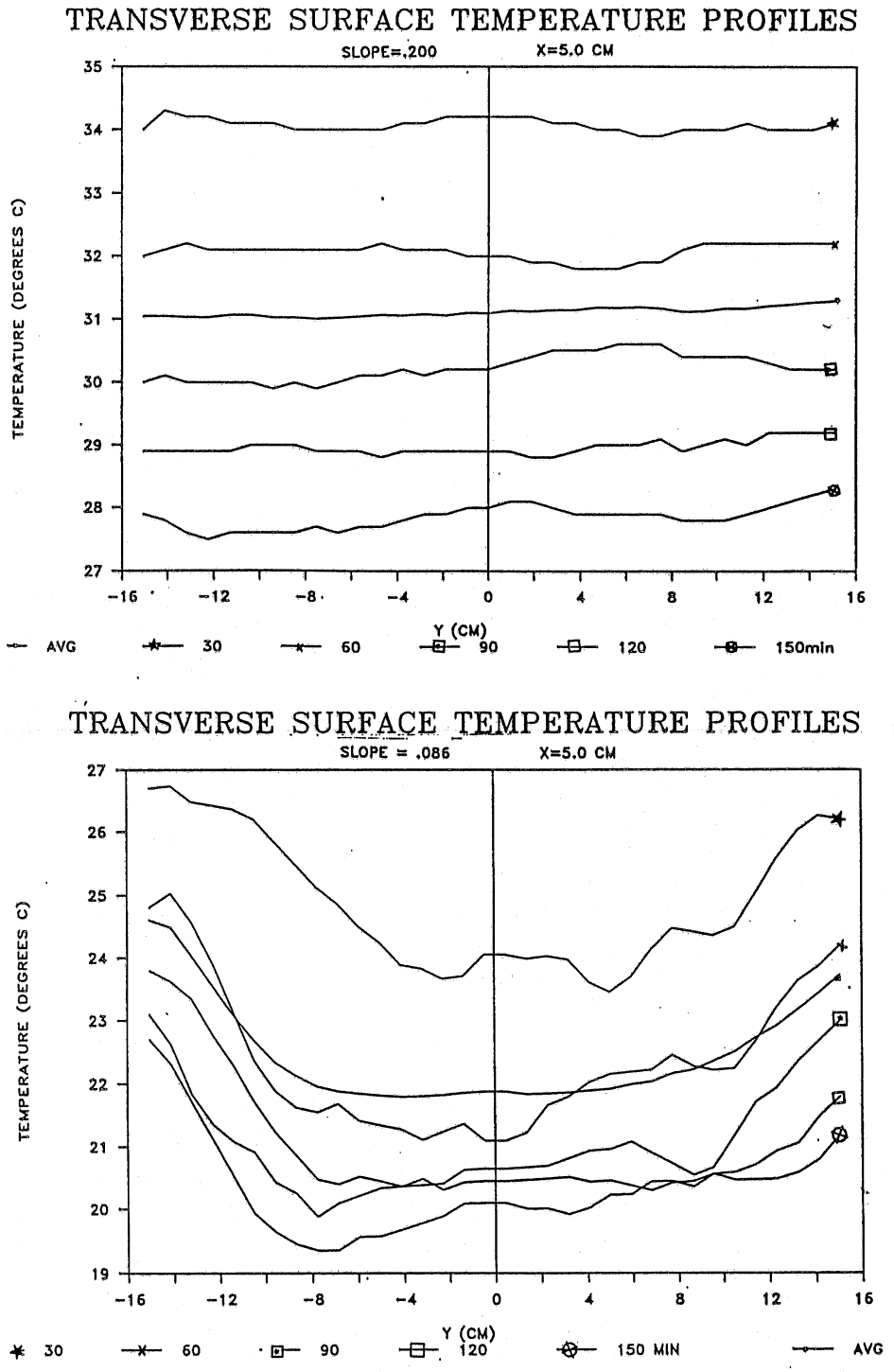

Fig. VI–10 Transverse surface temperature profiles at x=5cm for selected time instants.

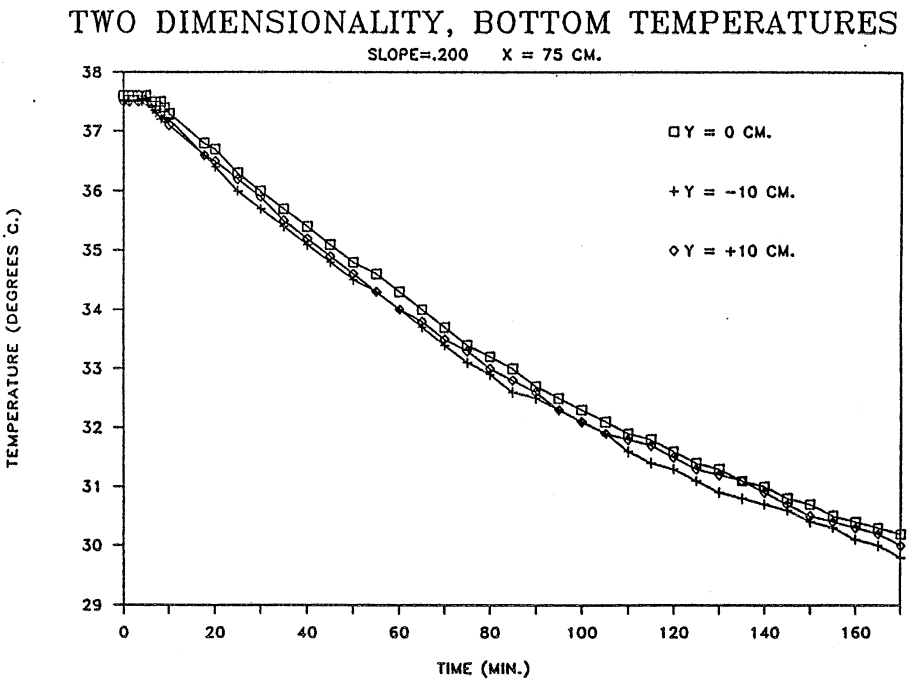

(a)

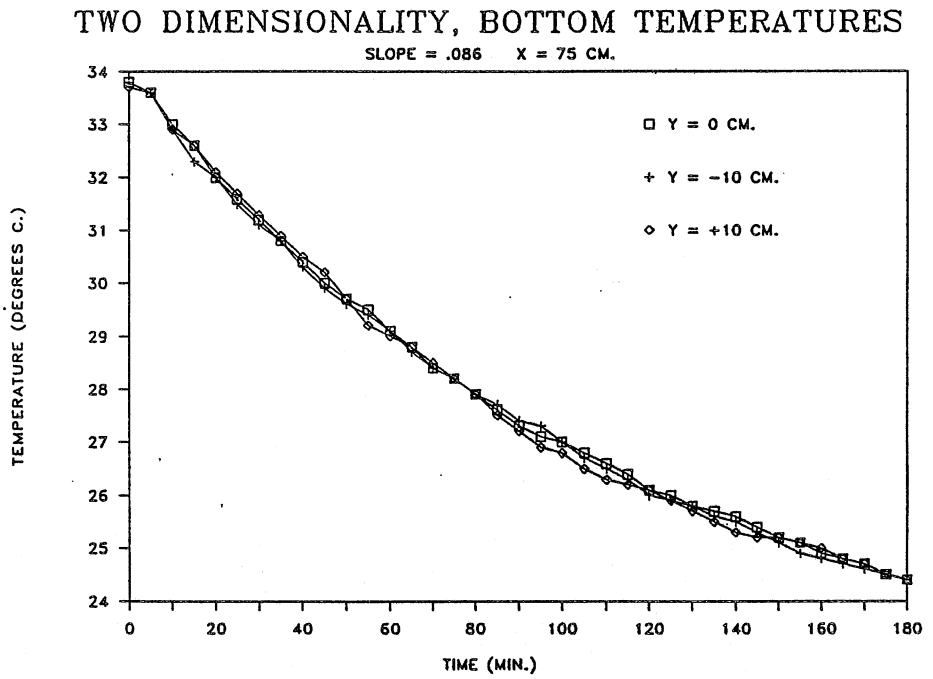

(b)

Fig. VI-11 Evolution of bottom temperature given by thermistors 9, 7, 10 for (a) S=0.2 (b) S=0.086

Q, v_{max}, Z_o versus time, Fig. VI–12b, seem to indicate that these quantities reach their quasi–steady ranges within 6 min; this is corroborated by the bottom– and surface–temperature versus time graphs (Fig. VI–12a,b). In addition, the quasi–steady values of these quantities, Q, v_{max}, Z_o, determined in a previous experiment (of slightly different Ra value, see section II–C and Table VI–1), are in reasonable agreement with the developed values of Q, v_{max}, Z_o.

The situation is less clear for S = 0.2 because Q, v_{max} and Z_o exhibit wider fluctuations and v_{max}, but not Q and Z_o might be exhibiting an ascending trend (Fig. VI–13). Nonetheless, again the averages determined later during the same experiment to represent quasi–steady values fall within the ranges of Q, v_{max}, Z_o measurements determined.

The longitudinal temperature profiles (Figs. VI–14, VI–15) can be seen to have a functional form similar to that of the calculated profiles (e.g. Fig. IV–8); they are characterized by a steep temperature gradient at the very shallow end and a much milder temperature increase towards the deep end. The bottom temperature time series for S = 0.086 (Fig. VI–14) reflect, overall, the exponential drop of the mean temperature. Some very intriguing anomalies appear, however, in the form of substantial local rises of temperature (up to 1°C). This is most pronounced at x = 15 cm but is also apparent in the x = 25 and x = 35 cm series. The duration of these structures is up to ~ 20 min, which makes it unlikely that they reflect activity of thermals. No explanation of this phenomenon is available.

3. Quasi–Steady State

The temperature and velocity profile characteristics of the quasi–steady state of development are shown in Figs. VI–14 and VI–15 for S = 0.086 and 0.2, respectively. The temperature values from both the bottom (thermistors) and the surface (thermographs) are values averaged over 10 sec. Continuous records of surface temperature exist, but bottom temperatures were measured every five minutes only. The local velocity profile characteristics were also determined from averages. Each velocity profile was traced from two or occasionally three successive pictures of dye time–lines. For the experiment S = 0.086, the profiles were taken at one location three times and averaged while for profiles were taken at S = 0.2 only two times.

The ratio of the Z_o values to the local depth b was found to be 0.38 and 0.32 for S = 0.086 and 0.2, respectively (Figs. VI–14, VI–15). It is interesting to note that in the experiments of Harashima and Watanabe (1986), on side–arm convective currents on a horizontal bottom, in which the thickness of the two layers were allowed to develop naturally, this ratio was found equal to be 0.4.

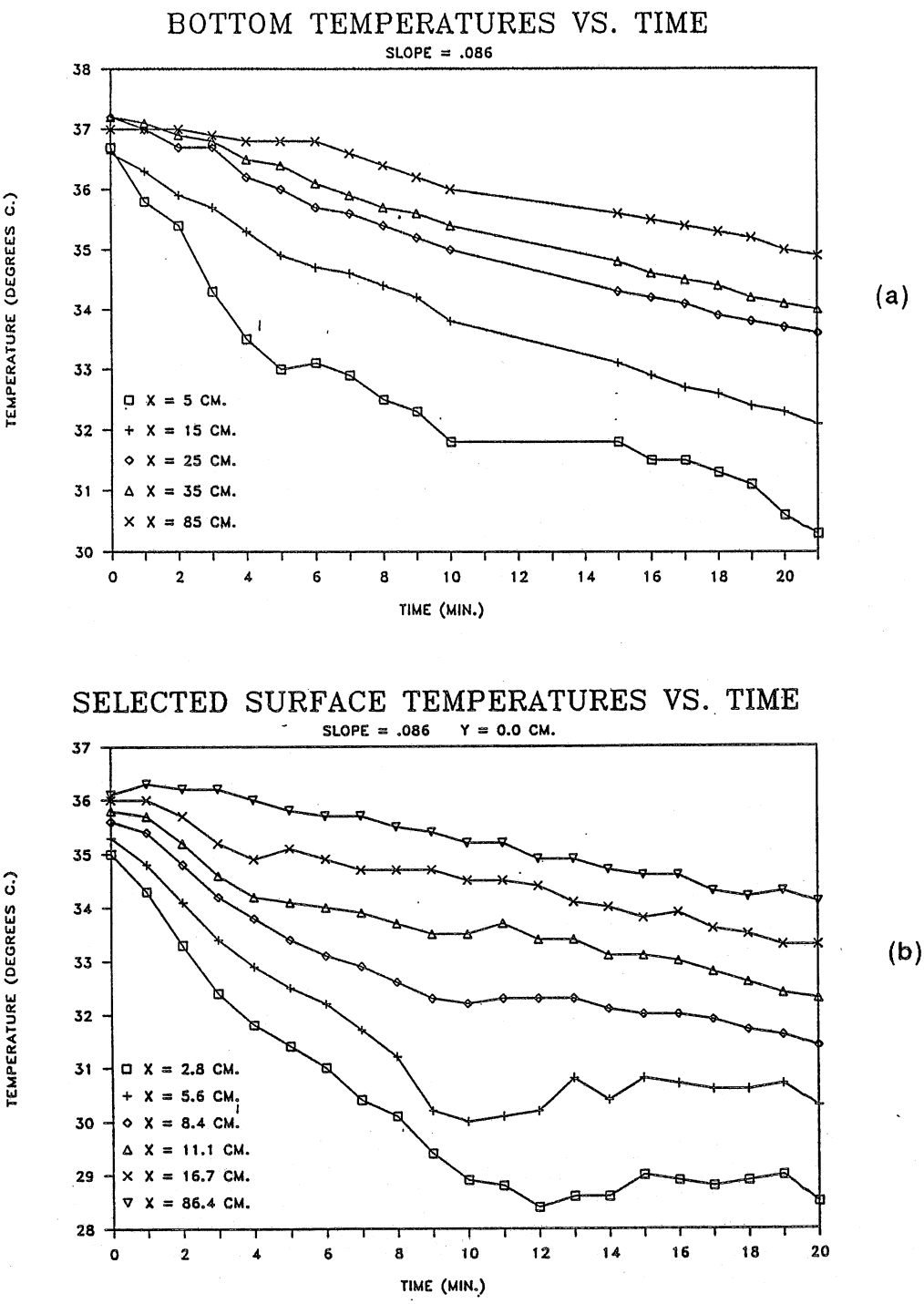

Fig. VI-12 Flow-onset characteristics for S=0.086 including (a) bottom temperature, (b) surface temperature.

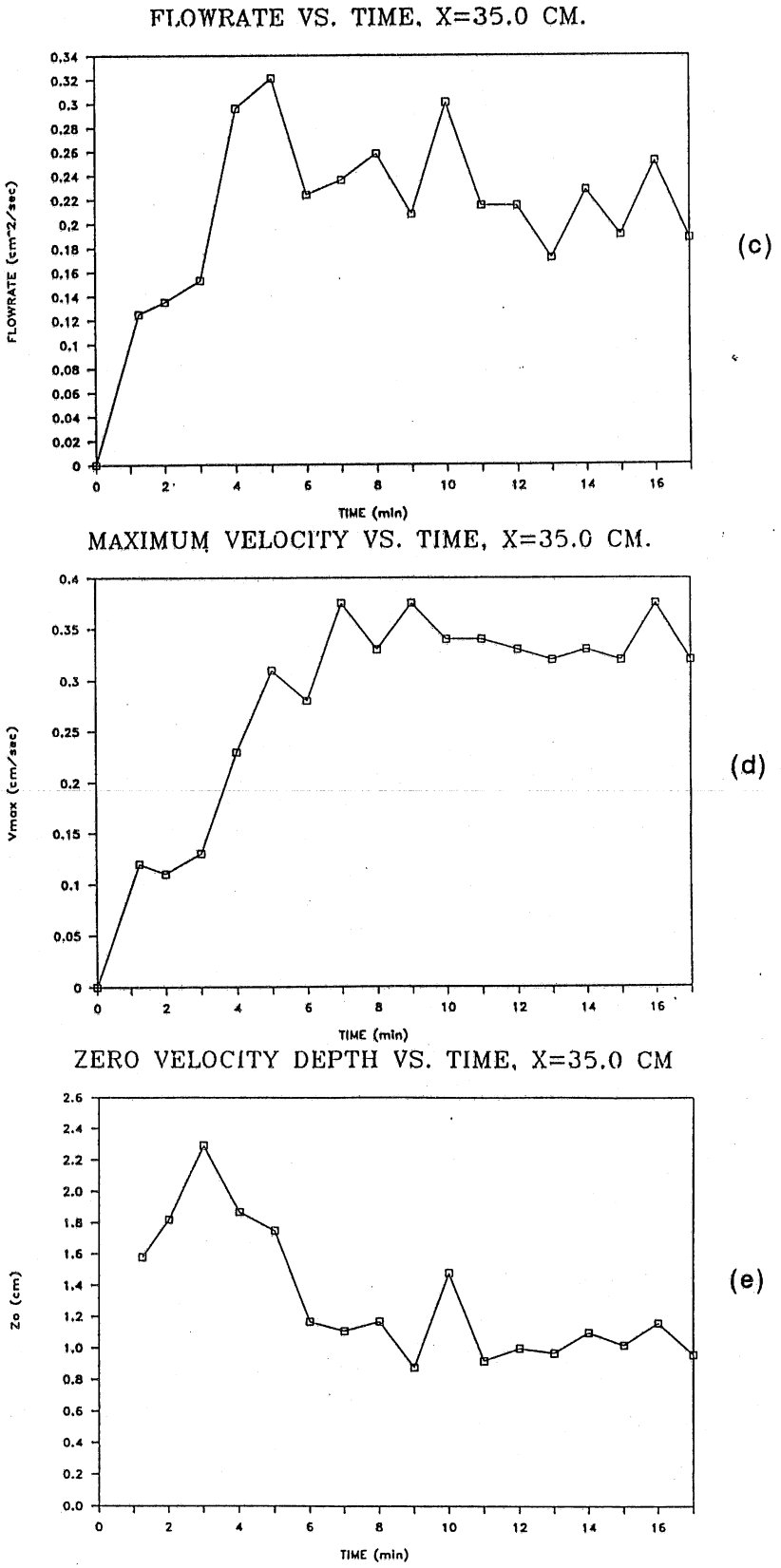

Fig. VI-12 (Continued) (c) flowrate, (d) local maximum velocities, and (e) location of zero velocity depth.

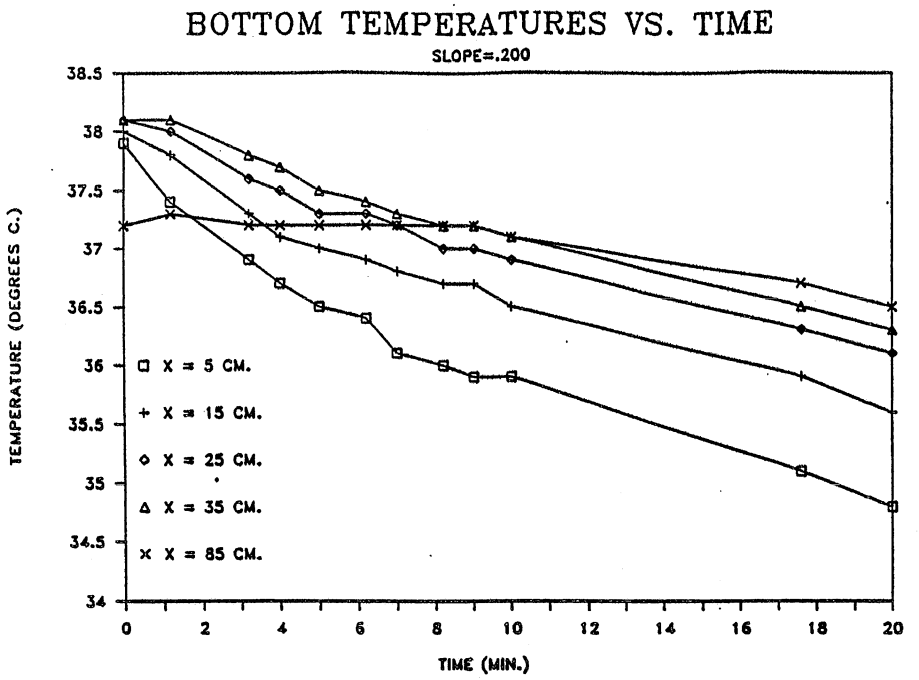

(a)

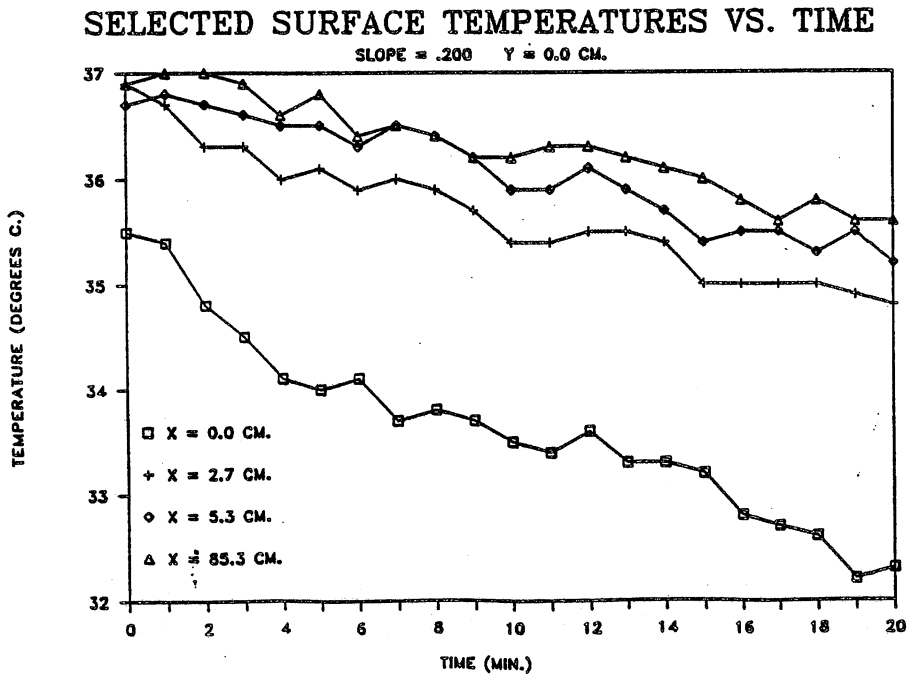

(b)

Fig. VI-13 Flow-onset characteristics for S=0.2 including (a) bottom temperature, (b) surface temperature

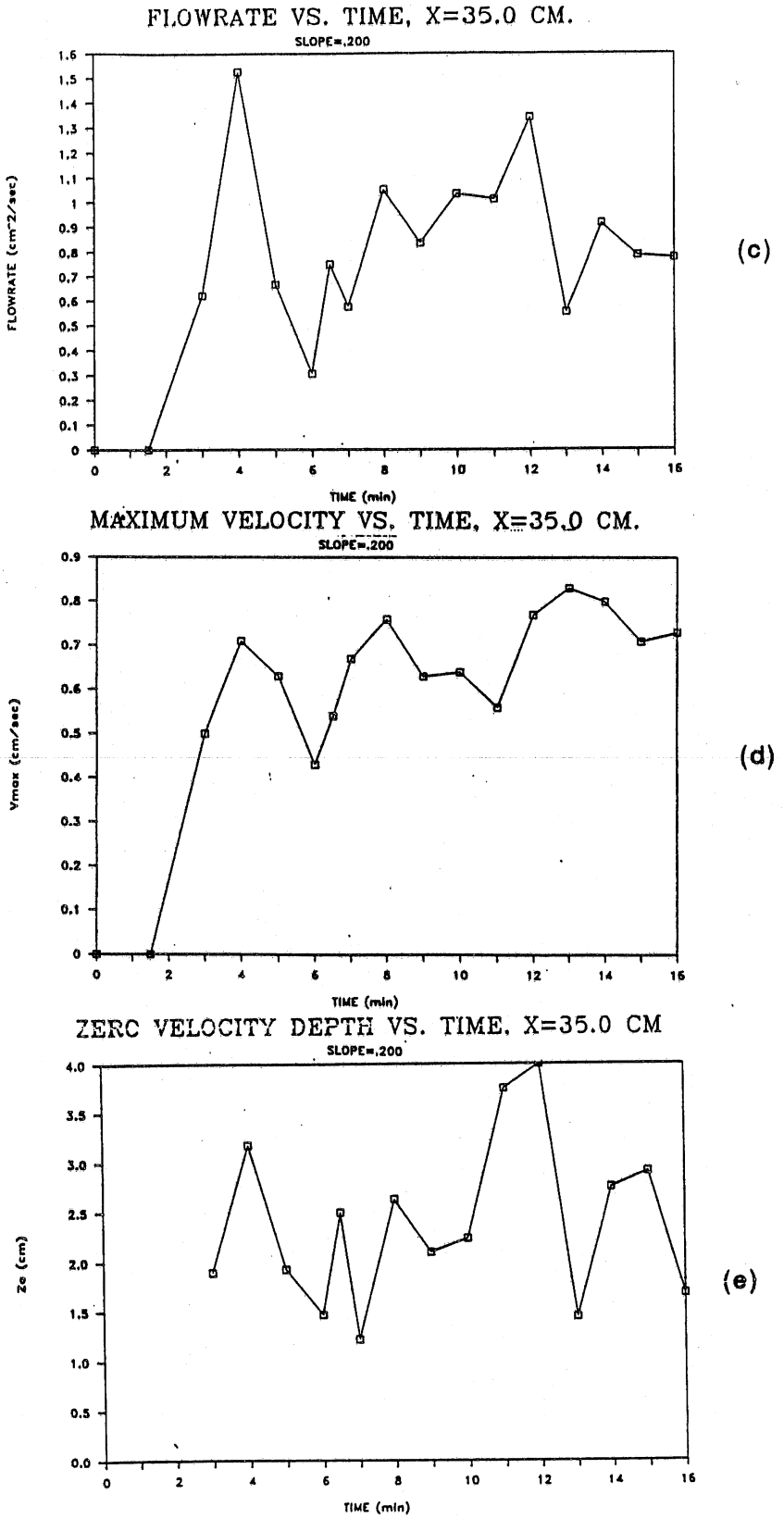

Fig. VI-13 (Continued) (c) flowrate, (d) local maximum velocities, and (e) location of zero velocity depth.

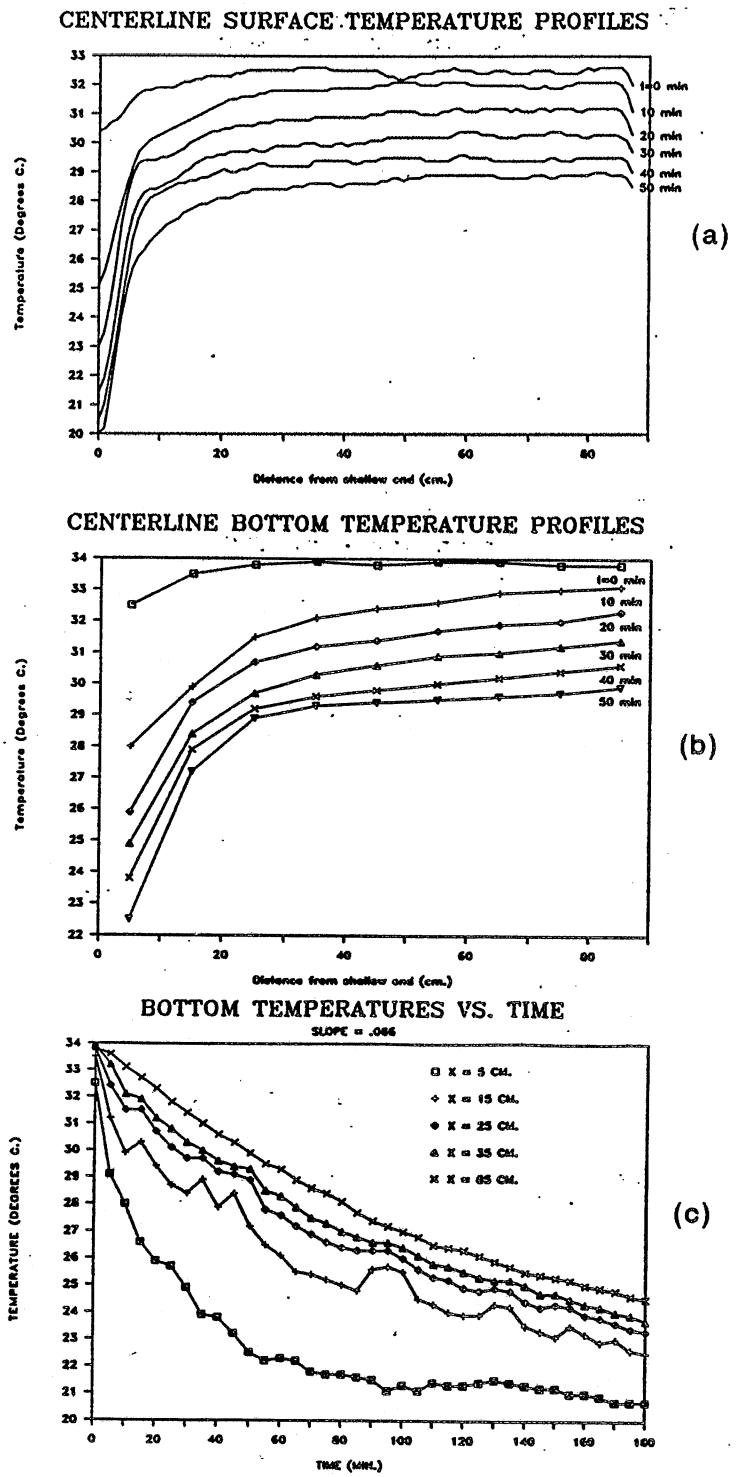

Fig. VI-14 Quasi-steady flow characteristics for S=0.086 including (a) centerline surface temperature, (b) bottom temperature profiles, (c) bottom temperature time series.

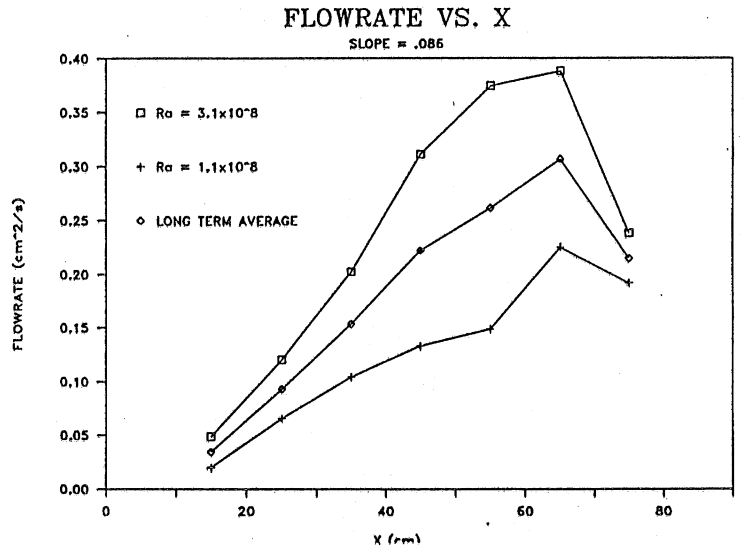

(d)

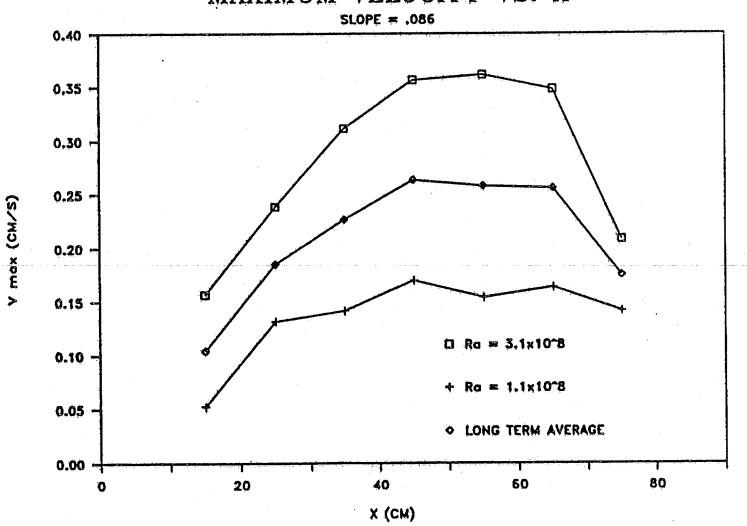

(e)

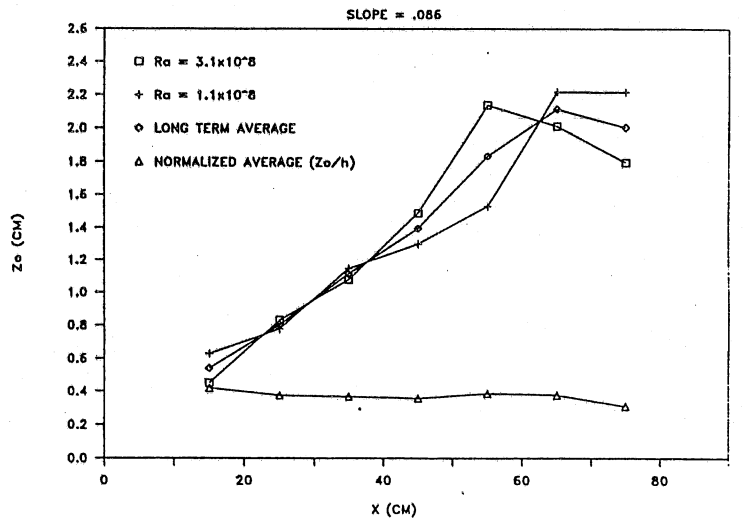

(f)

Fig. VI-14 (Continued) (d) flowrate, (e) local maximum velocities, (f) location of zero velocity depth.

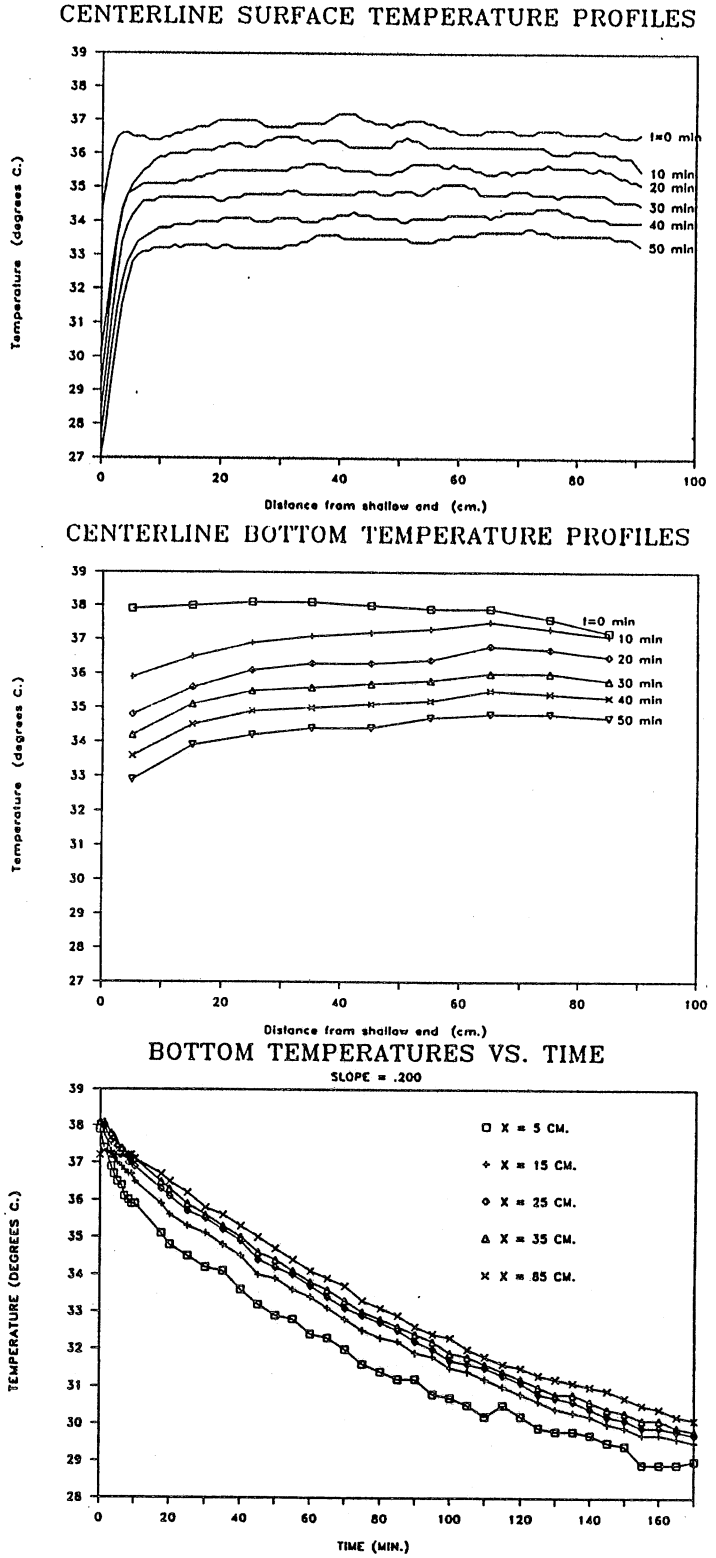

Fig. VI-15 quasi-steady flow characteristics for S=0.2 including (a) centerline surface temperature (b) bottom temperature profiles (c) bottom temperature time series.

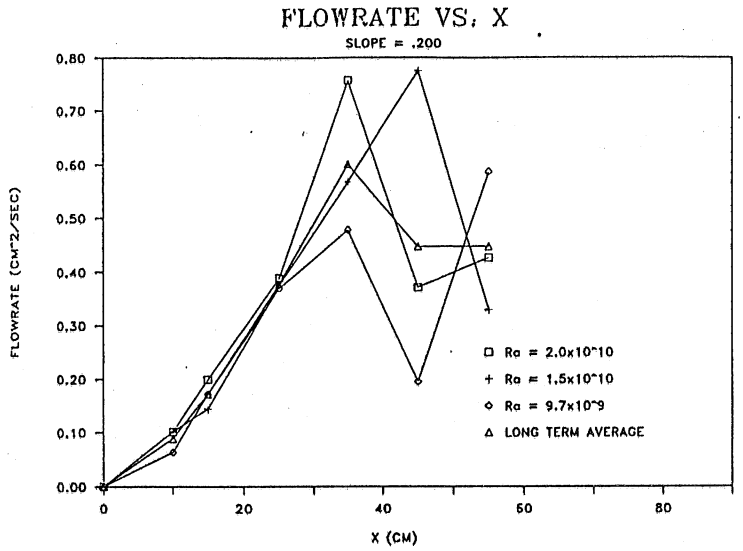

(d)

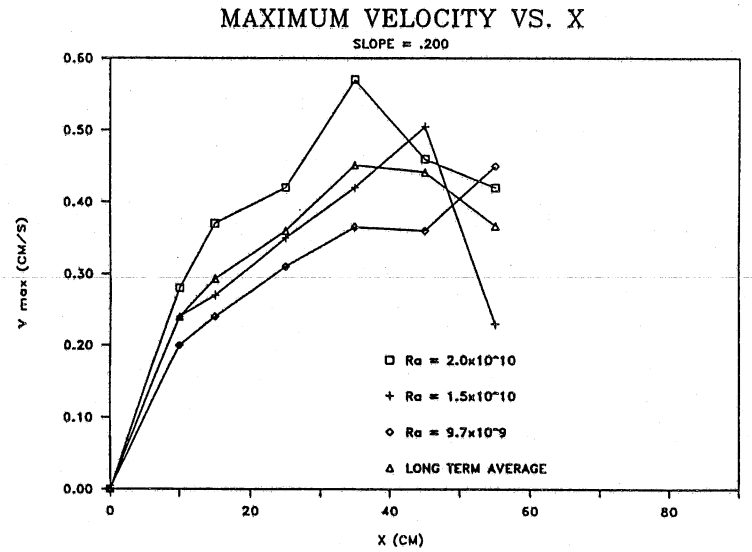

(e)

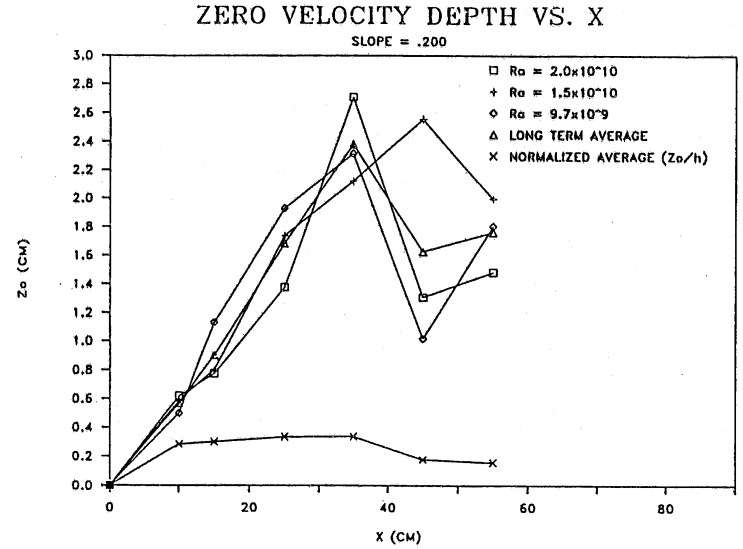

(f)

Fig. VI-15 (Continued) (d) flowrate, (e) local maximum velocities, (f) location of zero velocity depth.

VII. A MIXED–CELLS IN SERIES MODEL FOR THE ESTIMATION OF CONVECTIVE EXCHANGE IN THE LITTORAL REGION OF A SHALLOW LAKE DURING COOLING

The similarity between the phenomenon of cooling–induced convective circulation in the littoral zone of lakes and the convective circulation in the side arms of cooling lakes has already been pointed out in the Introduction. A significant difference, however, is that, because of excess heat disposed in cooling lakes, the cooling period is significantly longer than overnight cooling. Thus the side arm phenomenon can be meaningfully analyzed as a steady–state phenomenon [Brocard et al., 1977; Sturm and Kennedy, 1980; Jain, 1982]. In contrast, in practical field applications of the littoral circulation, the unsteady nature of this circulation needs to be taken into account. Unsteady models for the analysis of convective circulation exist neither for the side arm case nor for the littoral zone phenomenon. A second important difference between the two phenomenon, which significantly alters the nature of the flow, is the boundary condition at the junction of the side arm with the main lake. Brocard and Harleman [1980] showed that, if the side arm depth is more than double the epilimnion depth, a two–layer flow is established in the side arm. If, however, the side arm depth is less than approximately twice the epilimnion depth, then significant downflow from the upper to the lower layer occurs all along the side arm, rendering the two–layer schematization less useful. Under this condition, circulation in the littoral zone, which is usually contained in the epilimnion, cannot be expected to form a distinctly two–layer system. Rather, as has been confirmed the area above the upper, convectively unstable layer, vigorously interacts with the stable undercurrent.

Thus, in the developing exchange flow induced by cooling of the littoral zone of lakes, the vertical stratification that necessarily forms when the flow develops will be rather weak. The weakness of the vertical stratification makes possible the formulation of a very simple model, presented below, which is applicable if the depth of the littoral zone considered is less than the mixed layer depth of the lake. In shallow lakes and ponds this is often the case. The model requires input measurements of the evolution of vertical water temperature profiles in the littoral zone. This input accounts implicitly for the unsteadiness of the flow, as well as littoral geometrical details and even the existence of aquatic plants. Given that the temperature profiles can be easily measured in the field, whereas the low and intermittent velocities cannot, the model is useful and intended for the analysis of field measurements. To obtain exchange flow rates in a littoral region, a better model would rely on meteorological parameters as input, but such a model does not exist at present. To set the stage for the justification of some drastic simplifications, some features of the cooling induced littoral circulation that can be substantiated by referring to the experiments of Katsaros [1978], Sturm and Kennedy [1980], Rhee et al. [1984], or Harashima and Watanabe [1986], as well as the experiment described in Chapter V, are reviewed below.

A. DEVELOPMENT OF A HORIZONTAL TEMPERATURE GRADIENT ALONG A LITTORAL SLOPE IN RESPONSE TO COOLING

Where a horizontal layer of water is subjected to surface cooling, a cool thin layer formed at the surface breaks up periodically, generating sinking sheets of cool water (thermals) which force a return flow towards the surface. The thermals are active as long as cooling continues and provide a vertical stirring mechanism that keeps the horizontal layer vertically nearly well–mixed except for the very thin surface cool boundary layer.

The temperature evolution of a horizontal layer in response to surface cooling can be appropriately approximated by the heat budget for a well–mixed water body (Figure VII–1):

$$\rho \, c \, \forall \, \frac{dT}{dt} = HA \qquad \text{(VII–1)}$$

where

T = temperature of the well–mixed layer (°C)

A = surface area of the layer (m^2/m)

h = depth of the layer (m)

$\forall$ = volume of the layer $\forall = Ah (m^3/m)$

ρ = the water density (kg/m^3)

c = specific heat of water ($J \, kg^{-1} \, °C^{-1}$)

H = the rate of surface cooling (W/m^2)

The solution of the differential equation is

$$T(t) = \frac{H}{\rho \, c \, h} \, t + T_o \qquad \text{(VII–2)}$$

where T_o is the initial temperature (at $t = 0$). Equation VI–2 illustrates that layers of different depth (h) will, in time, develop different temperatures, even if they were initially at the same T_o and have the same A and are subjected to the same H.

If no horizontal flow takes place between the two (arbitrarily outlined) cells in Fig. VII–2, the temperature of each cell can be provided by Eq. VII–1 (using the mean depths h_1, h_2). $h_2 > h_1$ implies $T_1(t) < T_2(t)$, for $t > 0$. Assuming that all temperatures are above 4° C, heavier water (T_1) would be lying next to lighter water (T_2). Thus, even in the absence of an externally driven circulation (e.g. by wind), an exchange flow will arise naturally in a sloping littoral zone during cooling. Since such an exchange flow implies also exchange of heat, Eq. (VII–2) is no longer adequate but should be modified as follows. For the sake of simplicity of the exposition only exchange through boundary b is considered below, while the equations accounting also for exchange through a and c are given in Appendix I.

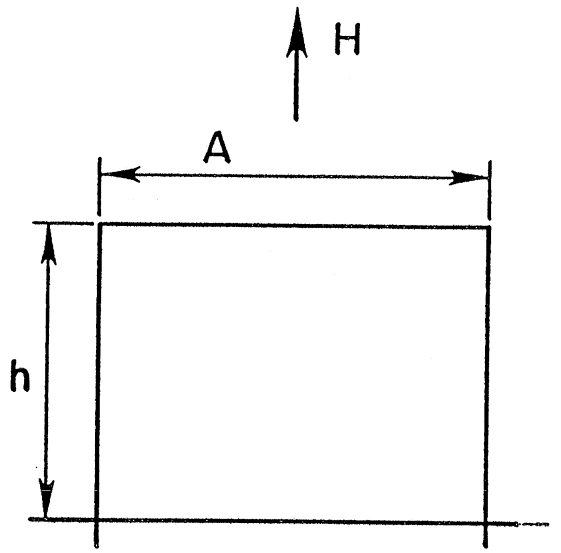

Fig. VII–1 Schematic of a well–mixed cell.

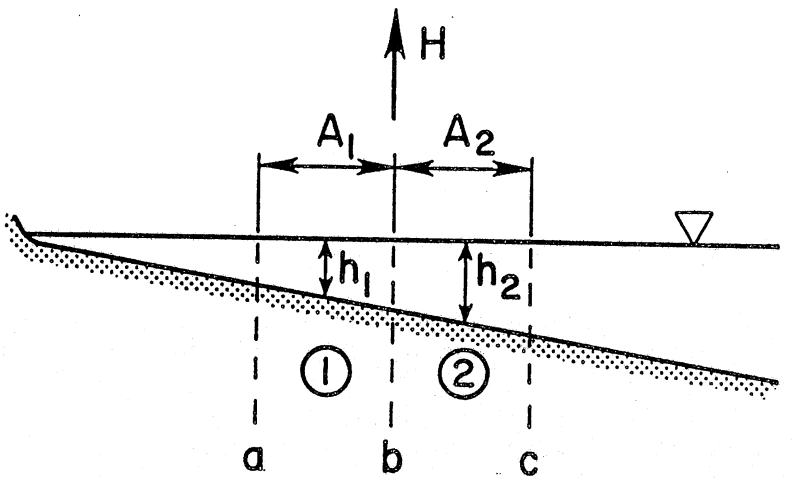

Fig. VII–2 Adjacent mixed cells on a littoral slope.

$$\text{Cell 1:}\quad \rho\, c\forall_1 \frac{dT_1}{dt} = H\, A_1 + Q\, \rho c\, T_2 - Q\, \rho c\, T_1 \qquad \text{(VII–3a)}$$

where the term on the left represents the rate of change of energy content, the first term on the right the surface heat loss, the second term the heat carried by inflow, and the last term the heat carried by outflow.

$$\text{Cell 2:}\quad \rho\, c\forall_2 \frac{dT_2}{dt} = H\, A_2 + Q\, \rho c\, (T_1 - T_2) \qquad \text{(VII–3b)}$$

where Q = hydraulic exchange flow rate between cells 1 and 2 ($m^3\ sec^{-1}\ m^{-1}$). In a field application, the temperature cells 1 and 2 need to be monitored, so that the terms dT_i/dt, i = 1,2, can be estimated by casting them into finite difference form. Equations VII–3a and 3b can then be regarded as two equations for Q and H since the remaining parameters describe the geometry and water properties. The solution is:

$$H = \rho c \frac{\forall_1 \frac{dT_1}{dt} + \forall_2 \frac{dT_2}{dt}}{A_1 + A_2} \qquad \text{(VII–4a)}$$

and

$$Q = \frac{A_2\, \forall_1 \frac{dT_1}{dt} - A_1\, \forall_2 \frac{dT_2}{dt}}{(T_2 - T_1)(A_1 + A_2)} \qquad \text{(VII–4b)}$$

B. A WELL–MIXED CELLS–IN–SERIES MODEL FOR THE ESTIMATION OF A HYDRAULIC EXCHANGE FLOW ALONG A LITTORAL SLOPE

Equations VII–3a and 3b illustrate how the heat budget equations of two adjacent water columns (cells) can be used to estimate the exchange flow that develops between them. To estimate the horizontal exchange at different points along the littoral zone, the zone is divided into n cells (Fig. VII–3). The temperature of each of these cells can be monitored in the field (e.g. by several thermisters), and the temperature profile can be averaged to extract a mean temperature that is considered to be the average temperature of the well–mixed cells.

A heat budget, similar to Eqs. VII–3a and 3b can be written for each of the n cells. These equations form a system of n equations, which contain no unknowns H, $Q_{1,2},\ldots,Q_{n-1,n}$; it has a unique solution which is written in recurrent form in Appendix I.

This formulation is based on the assumption that no exchange flow occurs at the outer boundary of the last cell (number n). For this to be true no appreciable horizontal temperature gradient between the last cell and the open waters should exist. An appropriate location for such a cell can be estimated using Eq. VII–2 as follows. Equation VII–2 can give the temperature gradient that develops between two cells when no exchange flow between them exists. This temperature gradient represents, then, an upper

bound of the temperature gradient that forms when an exchange flow actually develops. For this analysis we assume that beyond cell n, there is cell n+1 (Fig. VII–3).

$$T_n(t) = \frac{H}{\rho c}\frac{1}{h_n}\,t + T_o \quad \text{and} \quad T_{n+1} = \frac{H}{\rho c}\frac{1}{h_{n+1}}\,t + T_o \qquad \text{(VII–5)}$$

or assuming identical initial temperature T_o:

$$T_{n+1} - T_n = \frac{H}{\rho c}\left[\frac{1}{h_{n+1}} - \frac{1}{h_n}\right]t \qquad \text{(VII–6)}$$

For example, using as a typical heat loss $H = -200$ W/m^2, $\rho c = 4.2\times10^6$ J$_m^{-3}$°C^{-1}, if the depths are $h_n = 0.5$ m and $h_{n+1} = 1$ m, then after 6 hrs, $T_{n+1} - T_n = 1$°C. If instead $h_n = 10$ m and $h_{n+1} = 12$ m, then $T_{n+1} - T_n = 0.02$°C. If instead $h_n = 10$ m and $h_{n+1} = 12$ m, then $T_{n+1} - T_n = 0.02$°C. At 1°C temperature difference a significant exchange flow will develop but at 0.02°C it can be ignored.

In more general terms, from the recurrent nature of the solution of the system of equation (Appendix I) it can be seen that $Q_{n,n+1}$ does not enter in the calculation of $Q_{1,2},\ldots,Q_{n-1,n}$. However, the assumption $Q_{n,n+1} = 0$ enters implicitly Eq. A2–1, which, with $Q_{n,n+1} \neq 0$, would be:

$$H = \frac{\forall_1 \frac{dT_1}{dt} + \ldots + \forall_n \frac{dT_n}{dt} - Q_{n,n+1}\,\rho c(T_{n+1} - T_n)}{A_1 + \ldots + A_n} \qquad \text{(VII–7)}$$

From this equation, it can be seen that a sufficient criterion for selecting the last cell is that $T_{n+1} \simeq T_n$.

C. CRITICAL EXAMINATION OF THE ASSUMPTIONS, AND MODEL REFINEMENTS

(i) In developing the model it was assumed that all cells are subjected to the same surface heat loss rate H. This would be true if the heat loss were a function of the meteorological condition only. However, H depends on the water surface temperature and a possible formulation for H is

$$H = K(T_e - T_s) \qquad \text{(VII–8)}$$

where T_e = equilibrium temperature (i.e. the temperature at which the net surface heat loss H would be zero, see e.g. Edinger et al. 1968, page 1139), T_s = water surface temperature; and K = bulk heat exchange coefficient. This formulation can be incorporated into the model if T_e is monitored in

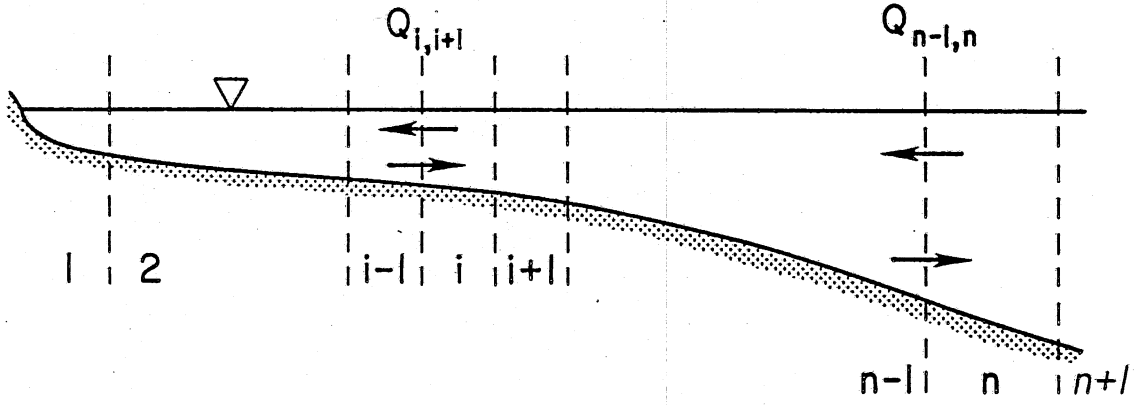

Fig. VII–3 Division of the littoral slope into cells in series.

the field. This can be approximately achieved by measuring the temperature of water in shallow buckets placed in situ. Then the first equation in set A2 becomes an equation for K instead of H. The equilibrium temperature formulation is somewhat preferable because the assumption of a spatially constant H will cause overestimation of the exchange flow rate Q. If $T_s - T_e$ is large relative to variations in T_s, the resulting error in Q will, however, be negligible.

(ii) The concept of well–mixed cells was justified before introducing Eq. VII–1 by noting that when a layer of water is cooled from the surface the thermals that develop keep the layer well–stirred. This schematization was retained in the formulation of Eq. VII–3a and 3b, even though the formation of the undercurrent implies that a two–layer system develops. A partial justification for this erroneous practice is that the two–layer system is a weak one because, as shown by Brocard and Harleman [1980] as well as the visualization experiment described in Chapter VI, significant downflow from the upper to the lower layer occurs.

A remedy might be to use the lower part of the temperature profile to calculate the heat outflow from a cell, while using the upper part of the profile for the heat inflow. Such a procedure would introduce some degree of arbitrariness with regard to depth and should be implemented only after further study of the two–dimensional flow field. This is the main shortcoming of the model and the reason why the outcome of this cell in series model can only give an estimate of the exchange flow rate.

(iii) The development of stable vertical density stratification during the heating phase of a diel cycle renders the application of this model to that phase of the diel cycle problematic and not recommendable.

(iv) The exchange flow examined here is induced during the cooling part of the diel cycle and is thus inherently unsteady. If the measurements are taken too early after the onset of cooling, a convective flow may not have developed. In that case, the model will predict zero exchange flow. The only prerequisite for Eq. VII–3 to hold is that substantial vertical stratification be absent. This is insured by natural convection during surface cooling. In the example presented in Section VII–4, the convective circulation in the up to 1.3 m deep water developed within much less than four hours.

D. EXAMPLE

The application of the model is illustrated by the following example. The unpublished temperature profiles used here were obtained as part of a more general field research program conducted in a densely vegetated littoral region at Eau Galle Reservoir, Wisconsin [Filbin and Barko, 1985].

The geometry of the site where the temperature profiles were measured is sketched in Fig. VII–4. The temperature measurements used in this example were taken between 1700 and 2300 hours on September 2, 1981; cubic spline interpolation was used to calculate values at exactly 1800 and 2200 hours.

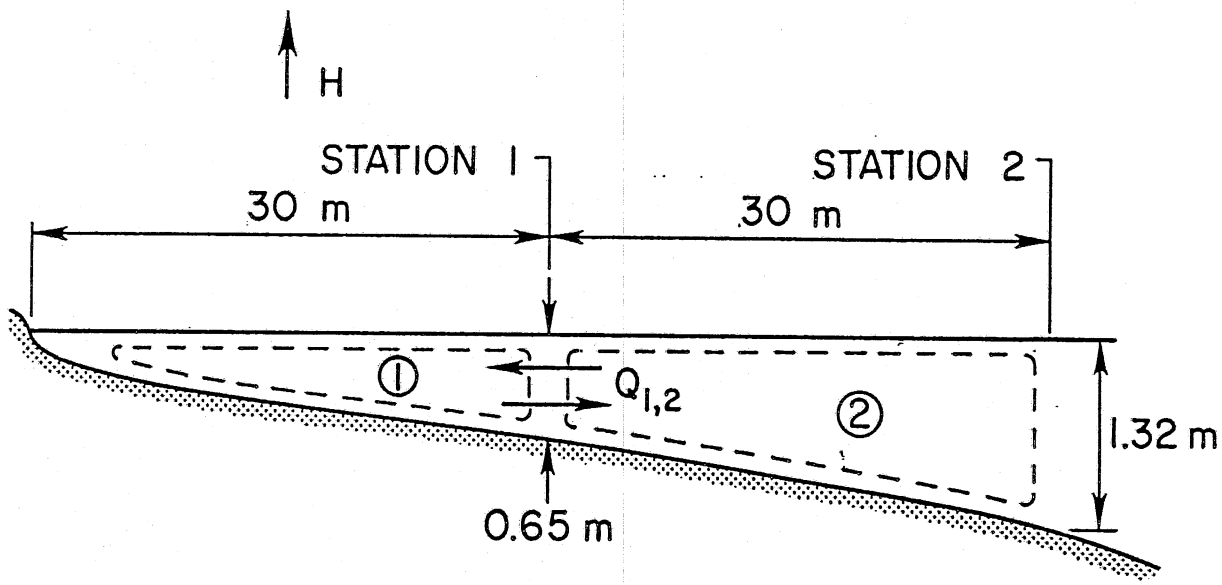

Fig. VII–4 Geometry of the field study.

Before Eqs. VII–4a and 4b can be used, the averages of cell temperatures T_1, T_2 have to be calculated and the derivatives dT_1/dt, dT_2/dt have to be approximated in finite difference form; this is shown in Table VII–1.

Using the numbers from Table VII–1 and Eqs. 4a and 4b, one obtains

$$H = 4.2\times10^6 \frac{9.75 \times (-6.62\times10^{-5}) + 29.6 \times (-8.21\times10^{-5})}{60} = 215 \text{ W m}^{-2}$$

$$Q = \frac{30.0 \times 9.75 \times (-6.62\times10^{-5}) - 30.0 \times 29.6 \times (-8.21\times10^{-5})}{(21.79 - 21.18) \times 60)}$$

$$= 1.46\times10^{-3} \text{ m}^3 \text{ s}^{-1} \text{ m}^{-1}$$

The calculation of H is based on the measured rate of change of the water temperature and is therefore the most direct determination of H. An independent estimate of H would have to be based on meteorological parameters [see e.g. Edinger et al., 1968], but that method would involve greater uncertainty. The value of 215 W m^{-2} is reasonable.

The calculation of Q should be regarded as an estimate, as has been discussed above. The magnitude of the mean velocity corresponding to the calculated Q is 5 mm/s and falls within the range of velocities measured in laboratory experiments of convective circulation [e.g. Sturm and Kennedy, 1980].

The exchange rate Q = 1.5×10^{-3} m^3 s^{-1} m^{-1} was the mean value over four hours. Additional data of the same study showed that such a flow rate could actually occur for 8 hours. The volume of water exchanged between cells 1 and 2 in 4 hours is 21.6 m^3 m^{-1}. The volume of cell 1 is only 9.8 m^3 m^{-1} and that of cell 2 is 29 m^3 m^{-1}. This implies that water in cell 1 is renewed hydraulically every two hours and that in cell 2 every five hours. Expressed otherwise, the hydraulic residence times ($t_r = \forall/Q$) in cells 1 and 2 are two and five hours, respectively. These estimates, which are comparable to the turnover time (7.9 h) estimated for water in the littoral zone of Lake Wingra, WI [Weiler, 1978], show how important the convective exchange flow induced by cooling can be.

E. APPLICATION TO DISSOLVED MATERIAL TRANSPORT

The convective exchange will not only transport heat between cells 1 and 2 but also materials in solution such as nutrients, pesticides, etc. If it is assumed that, at time t = 0, the concentration in cell 1 is $C_1(0) = C_{10}$ and in cell 2 it is $C_2(0) = C_{20}$, then after time t the concentrations will be given by the solutions of the equations

$$\forall \frac{dC_1}{dt} = Q(C_2 - C_1) - K_1C_1\forall_1 \qquad \text{(VII–9a)}$$

$$\forall_2 = Q(C_2 - C_1) - K_2C_2\forall_2 \qquad \text{(VII–9b)}$$

Table VII–1 Computation of Well–Mixed Cell Temperature and Rate of Temperature Change with Time

Depth from Surface (m)	Depth Increment Δd (m)	T at 22 hrs (°C)	T at 18 hrs (°C)	$(T_{22}-T_{18})*\Delta d$ (°C·m)	$(T_{18}+T_{22})*\Delta d/2$ (°C²m)
Cell 1					
0.	0.12	20.85	23.06	–0.27	2.63
0.24	0.195	20.83	22.94	–0.41	4.27
0.39	0.15	20.91	21.05	–0.02	3.15
0.54	0.185	20.33	19.92	0.08	3.72
0.65				–0.62	13.77

$$T_1 = \frac{13.77}{0.65} = 21.18^\circ C \quad \text{(depth averaged temperature in cell 1)}$$

$$\frac{dT_1}{dt} \simeq \frac{\Delta T_1}{\Delta t} = \left[-\frac{0.62}{0.65}\right]/(4\times3600) = -6.62\times10^{-5}\ ^\circ C/s$$

Depth from Surface (m)	Depth Increment Δd (m)	T at 22 hrs (°C)	T at 18 hrs (°C)	$(T_{22}-T_{18})*\Delta d$ (°C·m)	$(T_{18}+T_{22})*\Delta d/2$ (°C²m)
Cell 2					
0.	0.055	21.28	22.22	–0.05	1.20
0.11	0.13	21.33	22.22	–0.12	2.83
0.26	0.15	21.44	22.30	–0.13	3.28
0.41	0.225	21.45	22.30	–0.19	4.92
0.71	0.305	21.48	22.29	–0.25	6.67
1.02	0.305	20.81	22.40	–0.48	6.59
1.32	0.15	20.67	22.95	–0.34	3.27
				–1.56	28.76

$$T_2 = \frac{28.76}{1.32} = 21.79^\circ C \quad \text{(depth averaged temperature in cell 2)}$$

$$\frac{dT_2}{dt} \simeq \frac{\Delta T_2}{\Delta t} = \left[-\frac{1.56}{1.32}\right]/(4\times3600) = -8.21\times10^{-5}\ ^\circ C/s$$

From Fig. VI–4, the geometry of the cells is taken as:

	Surface area per unit width m^2/m	Volume per unit width m^3/m
Cell 1	30	9.75
Cell 2	30	29.6

In these equations, C_1 and C_2 are concentrations and K_1 and K_2 are reaction (loss) rates of materials in cell volumes 1 and 2, respectively.

Equations 9a and 9b describe essentially a diffusion process between two cells. If the loss rates are equal ($K_1 = K_2 = K$), the concentrations in cell 1, $C_1(t)$ and in cell 2, $C_2(t)$ will vary with time as follows:

$$C_1 = \frac{C_{10} - C_{20}}{\forall_1 + \forall_2} \forall_2 \exp\left[-\left[Q\,\frac{\forall_1 + \forall_2}{\forall_1\,\forall_2} + K\right]t\right] + \frac{C_{10}\forall_1 + C_{20}\forall_2}{\forall_1 + \forall_2} \exp(-Kt) \qquad \text{(VII–10a)}$$

$$C_2 = \frac{C_{20} - C_{10}}{\forall_1 + \forall_2} \forall_1 \exp\left[-\left[Q\,\frac{\forall_1 + \forall_2}{\forall_1\,\forall_2} + K\right]t\right] + \frac{C_{10}\forall_1 + C_{20}\forall_2}{\forall_1 + \forall_2} \exp(-Kt) \qquad \text{(VII–10b)}$$

If the transported material is conservative, the convective exchange will tend to make concentrations in cells 1 and 2 identical (completely mixed system). The steady–state concentration after complete mixing of cells 1 and 2 is

$$C_m = \frac{C_{10}\forall_1 + C_{20}\forall_2}{\forall_1 + \forall_2} \qquad \text{(VII–11)}$$

To reach concentrations C_1 and C_2 that are within ± x% of C_m by convective exchange between cells 1 and 2, requires a time

$$t_{x1} = \frac{\forall_1\,\forall_2}{Q(\forall_1 + \forall_2)} \ell n \left[\frac{|C_{10} - C_{20}|}{\left[C_{10}\,\frac{\forall_1}{\forall_2} + C_{20}\right]x}\right] \qquad \text{(VII–12a)}$$

$$t_{x2} = \frac{\forall_1\,\forall_2}{Q(\forall_1 + \forall_2)} \ell n \left[\frac{|C_{20} - C_{10}|}{\left[C_{10} + C_{20}\,\frac{\forall_2}{\forall_1}\right]x}\right] \qquad \text{(VII–12b)}$$

If $C_{20} = 0$ (no material in cell 2),

$$t_{x1} = \frac{1}{\alpha} \ell n \left[\frac{\forall_2}{\forall_1 x}\right] \qquad \text{(VII–13a)}$$

$$t_{x2} = \frac{1}{\alpha} \ell n \left[\frac{1}{x}\right] \qquad \text{(VII–13b)}$$

where α is a time constant $Q\,(\forall_1\,\forall_2/\forall_1\,\forall_2)$. Applied to the example in Section VI–D, with $\forall_1 = 9.8$ m^3 m^{-1}, $\forall_2 = 29$ m^3 m^{-1}, $C_{20} = 0$, $C_{10} = C_0$, and $Q = 1.5\times10^{-3}$ m^3 s^{-1} m^{-1} one finds $\alpha = 0.74$ hrs^{-1}, and for x = 10%, $t_{x2} = 3.1$ hrs and $t_{x1} = 4.6$ hrs.

A more general solution for $K_1 \neq K_2$ is given in the Appendix.

Throughout this section, it has been assumed that the flow rate Q is constant. In reality, Q may vary with time throughout a cooling period, especially during the onset of the convective flow. Any computations with a constant Q are, of course, valid only for the time interval to which Q applies. Since different Q values can be calculated from frequent temperature profile measurements, the unsteady behavior can be simulated by repeating the above procedure.

F. IMPLICATIONS

Studies of nutrient exchange between littoral and pleagic regions of lakes have been particularly hampered by a general inability to accurately account for hydraulic exchange. Considering the importance of phosphorus in freshwater systems and the very real possibility that littoral vegetation contributes prominently to phosphorus pools in the open water [e.g. Carpenter, 1983], it is notable that very few studies provide estimates of net phosphorus flux between littoral and open water [Adams and Prentki, 1982]. As emphasized recently by Carpenter and Lodge [1986], one of the most important questions concerning the role of littoral zones in the functioning of lake ecosystems is the extent to which beds of vegetation act as sources or sinks for dissolved constituents in general. With continued improvements in understanding of hydraulic exchanges between littoral and pelagic regions, ability to estimate associated nutrient fluxes will also improve.

A cells–in–series model formulated for extracting estimates of the hydraulic exchange flow that develops along a littoral slope during cooling has been presented. The model requires the evolution of vertical temperature profiles measured along the littoral zone as input. In spite of the drastic simplifications that underlie its formulation, the model can provide a useful complement or alternative to other types of hydraulic exchange studies. Application of the model to a set of sample data shows that the exchange flow that develops during cooling can be very significant, with potential for massive transport of dissolved constituents in the water of a northern temperate lake.

VIII. SYNOPSIS

Some aspects of the circulation induced by surface cooling of water on a littoral slope (i.e. a region bounded by a sloping bottom) were studied by numerical simulation, a laboratory experiment and analysis of field data.

The numerical model is formulated in Chapter III, in terms of the equations of continuity and the two–dimensional, unsteady Navier–Stokes equations coupled with the energy equation through the buoyancy term. The dimensionless independent parameters that emerge once the equations are made dimensionless are the Rayleigh number (Ra), the Prandtl number (Pr), and the slope of the domain (S). Some consequences of the thermal boundary conditions on the heat transfer are clarified by examining the flow of heat imposed by the same boundary conditions in a solid domain (conduction problem).

Numerical solutions of the model problem are included in Chapter IV for different values of Ra, Pr and S. These solutions illustrate the development of different flow regimes as Ra is increased. For $Ra = 10^4$, the flow, starting from quiescent and isothermal boundary conditions, is initiated at the shallow end in the form of a cell that grows, and in time, fills the entire enclosure. For $Ra = 10^6$, simultaneously with the shallow–end cell, several cells form at the deep end as a result of a Bénard–like instability due to surface cooling. The steady state, however, consists of a single elongated cell that spans the entire enclosure, with a small cell at the deep end. For $Ra = 10^8$, the several convective cells that form during the flow initiation merge, in time, to form larger structures. The single elongated cell, however, is no longer stable and the flow remains time–dependent. A steady state is reached in a time–average sense only. The maxima of the flow field, Q_{max} and v_{max}, increase proportionally to r^n, where $1/3 < n < 1/2$. For high enough values of Pr (higher than ~ 7) the flow variables, appropriately scaled, are found independent of Pr, which implies that the contribution of the advective terms is minor. As the slope is decreased the flow accelerates in order to transport the imposed heat flux through a decreased depth, and it takes a longer time for the steady state to be reached.

In Chapter V an attempt is made to assess the effects of littoral plants on the convective circulation. It is argued that, as a rough approximation, the additional energy dissipation due to the presence of the aquatic plants can be introduced as an increased apparent viscosity. An example of a short littoral zone is given.

In Chapter VI the results of a laboratory experiment, conducted under conditions approximating the model of Chapter III, are summarized. The experimental measurements document the flow for Ra values beyond the range where numerical simulation is affordable. It is found that at $Ra \sim 10^{10}$, the dominant flow characteristics in the experiments such as the strong temperature gradient in the shallow part, the undercurrent, the intermittent

thermals, the unstable surface return flow are similar to those predicted by the numerical simulation. The experimental flow, however, was found to exhibit indications of three–dimensional structures, especially for the smaller slope.

Finally, in Chapter VII, field measurements of the evoluation of temperature profiles along the littoral slope of a lake undergoing cooling are shown to be compatible with the development of convective circulation. Based on a simplified cells–in–series model, it is shown that the exchange flow estimated to develop between the littoral and pelagic zones can cause significant renewal of the littoral water.

REFERENCES

Adams, M. S. and R. T. Prentki, 1982. Biology, metabolism and functions of littoral submersed weedbeds of Lake Wingra, WI, U.S.A., *Arch. Hydrobiol.* (Suppl.), Vol. 62, pp. 333–409.

Baker, D. J., 1966. A technique for precise measurements of small fluid velocities, *J. Fluid Mechanics*, Vol. 26, pp. 573–575.

Bejan, A., 1984. *Convective Heat Transfer*, J. Wiley.

Bejan, A., A. A. Al–Homoud, and J. Imberger, 1981. Experimental study of high–Rayleigh–number convection in a horizontal cavity with different end temperatures, *J. Fluid Mech.*, Vol. 109, pp. 283–299.

Brocard, D. N., G. J. Jirka and D. R. F. Harlemann, 1977. A model for the convective circulation in side arms of cooling lakes, R. M. Parsons Laboratory, *Report 223*, MIT.

Brutsaert, W. H., 1982. *Evaporation Into the Atmosphere; Theory, History, and Applications*, D. Reidel Company, Boston.

Burke, R. W., 1982. *Free Surface Flow Through Salt Marsh Grass*, Ph.D. Thesis, MIT, Woods Hole Oceanographic Institute, WHDI–82–50.

Busse, F. H., 1978. Non–linear properties of thermal convection, *Rep. Prog. Phys.*, Vol. 41, pp. 1929–1967.

Carpenter, S. R., 1983. Submersed macrophyte community structure and internal loading: Relationship to lake ecosystem productivity and succession, in J. Taggart (ed.), *Lake Restoration, Protection and Management*, USEPA, Washington, D.C., pp. 105–111.

Carpenter, S. R. and Lodge, D. M., 1986. Effects of submersed macrophytes on ecosystem processes, *Aquatic Botany*, Vol. 26, pp. 341–370.

Carslaw, H. S. and Jaeger, J.C., 1959. *Conduction of Heat in Solids*, Oxford University Press.

Cormack, D. E., Leal, L. G., and Imberger, J., 1974a. Natural convection in a shallow cavity with differentially heated end walls. Part 1. Asymptotic theory. *J. Fluid Mechanics*, Vol. 65, pp. 209–229.

Cormack, D. E., Leal, L. G., and Seinfeld, J. H., 1974b. Natural convection in a shallow cavity with differentially heated end walls. Part 2. Numerical solutions, *J. Fluid Mechanics*, Vol. 65, pp. 231–246.

Csanady, G. T., 1982. *Circulation in the Coastal Ocean*, D. Reidel Publishing Company.

Dale, H. M. and Gillespie, T. J., 1977. The influence of submerged auatic plants on temperature gradients in shallow water bodies. *Can. Jour. Bot.*, Vol. 55, pp. 2216–2225.

De Vahl Davis, G., 1968. Laminar natural convection in an enclosed rectangular cavity, *Int. J. Heat Mass Transfer*, Vol. 11, pp. 1675–1693.

Edinger, J. E., D. W. Dutweiler, and J. C. Geyer, 1968. The response of water temperatures to meterological conditions, *Water Resources Research*, Vol. 4, No. 5, pp. 1137–1143.

Filbin, G. J. and J. W. Barko, 1985. Growth and nutrition of submersed macrophytes in a eutrophic Wisconsin impoundment, *J. Freshwater Ecology*, Vol. 3, pp. 275–285.

Flack, R. D., T. T. Konopnicki, and J. H. Rooke, 1979. Measurements of natural convective heat transfer in triangular enclosures, *J. Heat Transfer*, Vol. 101, pp. 648–654.

Flack, R. D., 1980. The experimental measurement of natural convection heat transfer in triangular enclosures heated or cooled from below, *J. Heat Transfer*, Vol. 102, pp. 770–772.

Foster, T. D. and S. Waller, 1985. Experiments on convection at very high Rayleigh numbers, *Phys. Fluids*, Vol. 28, Part 2, pp. 445–461.

Foster, T. D., 1971. A convective model for the diurnal cycle in the upper ocean, *J. Geophysical Res.*, Vol. 76, pp. 666–675.

Foster, T. D., 1971. Intermittent convection, *Geophysical Fluid Dynamics*, Vol. 2, pp. 201–217.

Foster, T. D., 1969. The effect of initial conditions and lateral boundaries on convection, *J. Fluid Mech.*, Vol. 37, Part 1, pp. 81–94.

Foster, T. D., 1965a. Stability of a homogeneous fluid cooled uniformly from above, *Physics of Fluids*, Vol. 8, pp. 1249–1257.

Foster, T. D., 1965b. Onset of convection in a layer of fluid cooled from above, *Physics of Fluids*, Vol. 8, pp. 1770–1774.

Freitas, C. J., A. Findikakis, and R. L. Street, 1985. Three–dimensional simulation of a buoyancy driven cavity flow, in *Hydraulics and Hydrology in the Small Computer Age*, ASCE Conference, Florida, W. R. Waldrop, editor, pp. 1101–1105.

Grotzbach, G. Direct numerical simulation of laminar and turbulent Bénard convection. *J. Fluid Mechanics*, Vol. 119, pp. 27–53.

Harashima, A. and M. Watanabe, 1986. Laboratory experiments on the steady gravitational circulation excited by cooling of the water surface, *J. Geophysical Research*, Vol. 91, No. C11, pp. 13056–13064.

Harleman, D.R.F. and Hurley, K. A., 1977. Heat transport mechanisms in lakes and reservoirs. *Proceedings of the 17th Congress*, IAHR, Baden Baden.

Imberger, J., 1985. Thermal characteristics of standing waters: An illustration of dynamical processes, *Hydrobiol.*, Vol. 125, pp. 7–29.

Imberger, J., 1974. Natural convection in a shallow cavity with differentially heated end walls, Part 3. Experimental results, *J. Fluid Mechanics*, Vol. 65, pp. 247–260.

Jain, S. C., 1982. Buoyancy–driven circulation in free–surface channels, *J. Fluid Mech.*, Vol. 122, pp. 1–12.

Katsaros, K. B., 1981. Convection patterns in a pond, *Bulletin American Meteorological Soc.*, Vol. 62, No. 10, pp. 1446–1453.

Katsaros, K. B., 1978. Turbulent free convection in fresh and salt water. Some characteristics revealed by visualization, *J. Phys. Oceanography*, Vol. 8, No. 4, pp. 613–626.

Katsaros, K. B., W. T. Liu, J. A. Businger, and J. E. Tillman, 1977. Heat transport and thermal structure in the interfacial boundary layer in an open tank of water in turbulent free convection, *J. Fluid Mechanics*, Vol. 83, pp. 311–336.

Krishnamurti, R., 1970. On the transition to turbulent convection. Part 1. The transition from two– to three–dimensional flow. *J. Fluid Mechanics*, Vol. 42, pp. 295–314.

Krishnamurti, R. and L. N. Howard, 1981. Large scale flow generation in turbulent convection, *Proc. Natl. Acad. Sci., U.S.A.*, Vol. 78, pp. 1981–1985.

Lai, W. T. and J. W. Ramsey, 1987. *Natural Heat and Mass Transfer in a Rectangular Enclosure*, University of Minnesota Supercomputer Institute, 87/79, November.

Lipps, F. B., 1976. Numerical simulation of three–dimensional Bénard convection in air, *J. Fluid Mech.*, Vol. 75, pp. 113–148.

Lipps, F. B. and R. C. J. Somerville, 1971. Dyanmics of variable wavelength in finite–amplitude Bénard convection, *Phys. of Fluids*, Vol. 14, pp. 759–765.

Mallinson, G. D. and G. DeVahl Davis., 1977. Three–dimensional natural convection in a box: A numerical study, *J. Fluid Mechanics*, Vol. 83, pp. 1–31.

Moore, D. R. and N. O. Weiss, 1973. Two–dimensional Rayleigh–Bénard convection, *J. Fluid Mech.*, Vol. 58, part 2, pp. 289–312.

Ookubo, K. and Y. Muramoto, 1987. Density currents induced by surface cooling in Lake Biura, *IAHR Congress*, Lausanne.

Ostrach, S., 1982a. Low–gravity fluid flows, *Ann. Rev. Fluid Mech.*, Vol. 14, pp. 313–345.

Ostrach, S., 1982b. Natural convection heat transfer in cells and cavities, *Proceedings, the Seventh International Heat Transfer Conference*, München, F.D. R. (U. Grigull et al., eds.), Hemisphere, pp. 365–379.

Patankar, S. V., 1982. *A General Purpose Computer Program for Two–Dimensional Elliptic Situations*, Mech. Eng. Dept., University of Minnesota.

Patankar, S. V., 1981. A calculation procedure for two–dimensional elliptic situations, *Numerical Heat Transfer*, Vol. 4, pp. 409–442.

Patankar, S. V., 1980. *Numerical Heat Transfer and Fluid Flow*, McGraw–Hill, New York.

Patankar, S. V. and D. B. Spaulding, 1972. A calculation procedure for heat, mass and momentum transfer in three–dimensional parabolic flows, *Int. J. Heat and Mass Transfer*, Vol. 15, pp. 1787–1794.

Patterson, J. C., 1987. A model for convective motions in reservoir sidearms, *IAHR Congress*, Lausanne.

Patterson, J. and J. Imberger, 1980. Unsteady natural convection in a rectangular cavity, *J. Fluid Mechanics*, Vol. 100, Part 1, pp. 65–86.

Phillips, O. M., 1970. On flows induced by diffusion in a stably stratified fluid, *Deep–Sea Research*, Vol. 17, pp. 435–443.

Phillips, O. M., 1966. On turbulent convection currents and the circulation of the Red Sea, *Deep–Sea Res.*, Vol. 13, pp. 1149–1160.

Poulikakos, D. and A. Bejan, 1983. The fluid dynamics of an attic space, *J. Fluid Mech.*, Vol. 131, pp. 251.

Poulikakos, D. and A. Bejan, 1983. Natural convection experiments in a triangular enclosure, *J. Heat Transfer*, Vol. 105–652.

Quon, C., 1972, High Rayleigh number convection in an enclosure–a numerical study, *Phys. Fluids*, Vol. 15, pp. 12–19.

Rattray, M. and D. Hansen, 1962. A similarity solution for circulation in a estuasry, *J. Marine Res.*, Vol. 20, pp. 121–133.

Rhee, H. S., J. R. Koseff, and R. L. Street, 1984. Flow visualization of a recirculating flow by rheoscopic liquid and liquid crystal techniques, *Experiments in Fluids*, Vol. 2, pp. 57–64.

Sear, T. R., 1977. *Experiments on the Vertical Diffusion Coefficient in Flow Through Aquatic Plants*, M. S. Thesis, University of Wisconsin–Madison.

Spangenberg, W. G. and W. R. Rowland, 1961. Convective circulation induced by evaporative cooling, *Physics of Fluids*, Vol. 12, pp. 2482.

Stefan, H. and D. E. Ford, 1975. Temperature Dynamics in Dimictic Lakes, *Jour. Hydraulics Div.*, ASCE, HY1, pp. 97–114.

Sturm, T. W., 1976. *An Analytical and Experimental Investigation of Density Currents in Sidearms of Cooling Ponds*, Ph.D. Thesis, Mechanics and Hydraulics, University of Iowa.

Sturm, T. W. and J. F. Kennedy, 1980. Heat loss from sidearms of cooling lakes, *J. Hydraulic Div.*, ASCE, Vol. HY5, pp. 783.

Sturm, T. W., 1981. Laminar gravitational convection of heat is dead–end channels, *J. Fluid Mechanics*, Vol. 110, 97–113.

Tamai, N. and T. Asaeda, 1984. Sheetlike plumes near a heated bottom plate at large Rayleigh number, *J. Geophysical Res.*, Vol. 89, No. C1, pp. 727–734.

Tamai, N. and T. Asaeda, 1987. Convection lines on a heated bottom plate at large Rayleigh number, *J. Geophysical Research*, Vol. 92, No. C5, pp. 5489–5495.

Thompson, J. M. T. and H. B. Stewart, 1987. *Nonlinear Dynamics and Chaos*, John Wiley.

Tritton, D. J., 1959. Experiments on flow past a circular cylinder at low Reynolds numbers. *J. Fluid Mechanics*, Vol. 6, part 4, pp. 547–567.

Weiler, P. R., 1978. Littoral–pelagic water exchange in Lake Wingra, Wisconsin, as determined by a circulation model, *Report 100*, Inst. Environ. Studies, University of Wisconsin, Madison, 34 pp.

APPENDIX I

The notation $Q_{i,i+1}$ refers to the exchange flow rate between cells i and i+1 (see Fig. VI–3).

$$\left.\begin{aligned}
\rho c\, \forall_i \frac{dT_i}{dt} &= HA_i + Q_{1,2}(T_2 - T_1)\rho c \\
&\vdots \\
\rho c\, \forall_i \frac{dT_i}{dt} &= HA_i + Q_{i,i-1}(T_{i-1} - T_i)\rho c + Q_{i,i+1}(T_{i+1} - T_i)\rho c \\
& \quad i=2,\ldots,n-1 \\
&\vdots \\
\rho c\, \forall_n \frac{dT_n}{dt} &= HA_n + Q_{n,n-1}(T_{n-1} - T_n)\rho c
\end{aligned}\right\} \quad (A1)$$

Solution of the system of Equations (A1):

$$\left.\begin{aligned}
H &= \frac{\rho c \left[\forall_1 \frac{dT_1}{dt} + \ldots + \forall_n \frac{dT_n}{dt}\right]}{A_1 + \ldots + A_n} \\
Q_{1,2} &= \frac{\rho c\, \forall_1 \frac{dT_1}{dt} - HA_1}{(T_2 - T_1)\rho c} \\
Q_{i,i+1} &= \frac{\rho c\, \forall_i \frac{dT_i}{dt} - HA_i - Q_{i-1,i}\, \rho c(T_{i-1} - T_i)}{\rho c(T_{i+1} - T_i)} \\
i &= 2, \ldots, n-1
\end{aligned}\right\} \quad (A2)$$

APPENDIX I

The notation $Q_{i,i+1}$ refers to the exchange flow rate between cells i and i+1 (see Fig. VI–3).

$$\left.\begin{aligned}
\rho c\, \forall_i \frac{dT_i}{dt} &= HA_i + Q_{1,2}(T_2 - T_1)\rho c \\
&\vdots \\
\rho c\, \forall_i \frac{dT_i}{dt} &= HA_i + Q_{i,i-1}(T_{i-1} - T_i)\rho c + Q_{i,i+1}(T_{i+1} - T_i)\rho c \\
& \quad i=2,\ldots,n-1 \\
&\vdots \\
\rho c\, \forall_n \frac{dT_n}{dt} &= HA_n + Q_{n,n-1}(T_{n-1} - T_n)\rho c
\end{aligned}\right\} \quad (A1)$$

Solution of the system of Equations (A1):

$$\left.\begin{aligned}
H &= \frac{\rho c \left[\forall_1 \frac{dT_1}{dt} + \ldots + \forall_n \frac{dT_n}{dt}\right]}{A_1 + \ldots + A_n} \\
Q_{1,2} &= \frac{\rho c\, \forall_1 \frac{dT_1}{dt} - HA_1}{(T_2 - T_1)\rho c} \\
Q_{i,i+1} &= \frac{\rho c\, \forall_i \frac{dT_i}{dt} - HA_i - Q_{i-1,i}\, \rho c(T_{i-1} - T_i)}{\rho c(T_{i+1} - T_i)} \\
i &= 2, \ldots, n-1
\end{aligned}\right\} \quad (A2)$$

APPENDIX II

The solution to the system of Eqs. VI–9a and 9b is

$$C_1 = A_1\, e^{-\gamma t} + B_1 e^{-\delta t}$$

$$A_1 = \frac{Q(C_{10}-C_{20})\forall_2 + \left[-\frac{1}{2}(Q(\forall_1+\forall_2) + \forall_1\forall_2(K_2 - K_1)) + \frac{\forall_1\forall_2}{2} R\right] C_{10}}{\forall_1\ \forall_2\ R}$$

$$B_1 = \frac{-Q(C_{10}-C_{20})\forall_2 + \left[-\frac{1}{2}(Q(\forall_1+\forall_2) + \forall_1\forall_2(K_2 - K_1)) + \frac{\forall_1\forall_2}{2} R\right] C_{10}}{\forall_1\ \forall_2\ R}$$

where

$$R = \left[\left[Q\,\frac{\forall_1 + \forall_2}{\forall_1\ \forall_2} + K_1 + K_2\right]^2 - 4\left[\frac{K_1\forall_1 + K_2\forall_2}{\forall_1\ \forall_2}\, Q + K_1K_2\right]\right]^{1/2}$$

$$\gamma = \frac{1}{2}\left[Q\,\frac{\forall_1 + \forall_1}{\forall_1\ \forall_2} + K_1 + K_2\right] + \frac{1}{2} R$$

$$\delta = \frac{1}{2}\left[Q\,\frac{\forall_1 + \forall_2}{\forall_1\ \forall_2} + K_1 + K_2\right] - \frac{1}{2} R$$

Because the system 9a and 9b is symmetrical with respect to subscripts 1 and 2 (i.e. the differential equation for C_2 springs from the equation for C_1 if 1 and 2 are interchanged), the solution will have the same property. The solution for C_2 is:

$$C_2 = A_2\, e^{-\gamma t} + B_2\, e^{-\delta t}$$

where γ, δ are the same as above and A_2, B_2 can be found from A_1, B_1 by transposing the subscripts 1 and 2.

APPENDIX III

HEAT LOSS CALCULATIONS

Heat loss through the tank walls and bottom was measured by filling the tank to capacity with hot water and covering the container with a lid made of the same material that insulated the rest of the tank. A time record of temperatures and the following heat transfer expressions were used to compute a wall thermal resistance coefficient:

$$\rho c \forall \frac{\Delta \bar{T}}{\Delta t} = H_w A_w \qquad \text{(A–3)}$$

where ρ = water density,

c = specific heat of water,

$\forall$ = water volume,

$\Delta \bar{T}$ = $\bar{T}_2 - \bar{T}_1$ = bulk internal temperature drop over time interval

$\bar{T}_1$ = bulk water temperature at time $t = t_1$

$\bar{T}_2$ = bulk water temperature at time $t = t_2$

Δt = $t_2 - t_1$

H_w = heat loss per unit wetted area

A_w = wetted area

Additionally, a thermal resistance coefficient, R, can be defined as

$$R = \frac{\Delta T'}{H_w} \qquad \text{(A–4)}$$

where $\Delta T'$ = $\bar{T} - \bar{T}_a$ = temperature differential across wall

$\bar{T}$ = bulk internal temperature averaged over time period t_1 to t_2

$\bar{T}_a$ = air temperature,

combining (A–3) and (A–4),

$$R = \frac{\Delta T'}{\rho C \left(\frac{\forall}{A} \right) \left(\frac{\Delta T}{\Delta t} \right)} \qquad \text{(A–5)}$$